AD NUMBER

AD465068

LIMITATION CHANGES

TO:

Approved for public release; distribution is unlimited.

FROM:

Distribution authorized to U.S. Gov't. agencies and their contractors; Critical Technology; JUN 1965. Other requests shall be referred to Air Force Aero Propulsion Laboratory, Wright-Patterson AFB, OH 45433. This document contains export-controlled technical data.

AUTHORITY

AFWAL ltr dtd 29 Feb 1984

AFAPL-TR-65-48
Part I

HIGH SPECIFIC IMPULSE THERMAL ARC JET THRUSTOR TECHNOLOGY

Part I. Performance of Hall Arc Jets With Lithium Propellant

R. A. Moore, G. L. Cann, L. R. Gallagher
Electro-Optical Systems, Inc.

TECHNICAL REPORT AFAPL-TR-65-48, PART I

June 1965

Air Force Aero Propulsion Laboratory
Research and Technology Division
Air Force Systems Command
Wright-Patterson Air Force Base, Ohio

NOTICES

When Government drawings, specifications, or other data are used for any purpose other than in connection with a definitely related Government procurement operation, the United States Government thereby incurs no responsibility nor any obligation whatsoever; and the fact that the Government may have formulated, furnished, or in any way supplied the said drawings, specifications, or other data, is not to be regarded by implication or otherwise as in any manner licensing the holder or any other person or corporation, or conveying any rights or permission to manufacture, use, or sell any patented invention that may in any way be related thereto.

This report is not releasable to OTS — Foreign announcement and distribution of this report is not authorized. "The distribution of this report is limited because it contains technology identifiable with items on the strategic embargo lists excluded from export or reexport under U.S. Export Control Act of 1949 (63STAT.7), as amended (50 U.S.C. App. 2020.2031), as implemented by AFR 400-10".

Copies of this report should not be returned to the Research and Technology Division unless return is required by security considerations, contractual obligations, or notice on a specific document.

FOREWORD

This report was prepared by Electro-Optical Systems, Inc., Pasadena, California, to summarize the results of the first Phase of Contract AF 33(615)-1579, Project No. 3141, Task No. 314101. This contract began in April 1964 and the first phase ended in March 1965. The contractor's number for this report is EOS 5090 Phase I Final. The report authors are R. A. Moore, G. L. Cann, and L. R. Gallagher.

This research contract is funded by the Aero Propulsion Laboratory of the Air Force Research and Technology Division. The program is monitored in the Electric Propulsion Technology Section of the Aero Propulsion Laboratory by Mr. Paul Lindquist.

The authors gratefully acknowledge the contributions of C. H. Giltner, R. L. Harder, E. Doty, S. Snider, E. Julian, J. Cole, R. Swope, and T. Jacobson in obtaining the results reported.

The report was submitted for Air Force approval on 30 April 1965.

ABSTRACT

The objective of this program is to develop the technology of efficient electric arc jet thrustors for high specific impulse and long life. It is aimed particularly at power levels up to 300 kW, specific impulse between 1500 and 4000 seconds, and overall efficiency greater than 60 percent for durations of 500 hours.

The approach combines analytical and experimental research to investigate and develop thrustors using lithium and other alkali metals as propellants. Alkali metals have the advantage of high frozen-flow efficiency compared to gaseous propellants used in previous arc jet work. The use of lithium in this I_{sp} range requires energies per particle which are not achievable by the electrothermal arc-heating process. Thus, it is necessary to employ, in addition, electromagnetic acceleration processes. The present approach has relied predominantly on Hall current interactions with an applied magnetic field.

Lithium thrustors have been tested at power levels up to 40 kW. Thrust efficiencies (neglecting power dissipated in the magnet coil) of 70 percent at I_{sp} of 5000 sec, 60 percent at 4000 sec, 45 percent at 3000 sec and 30 percent at 2000 sec have been measured in a test chamber at pressures of the order of 10^{-2} mm Hg. Other tests demonstrated that test chamber pressures between 10^{-2} and 10^{-5} mm Hg have little effect on performance. A 10-hour endurance test was made with a 10-kW thrustor operating at an I_{sp} of about 5000 sec with an efficiency of 53 percent.

The performance results must be considered tentative until an investigation of the effect on performance of test chamber pressure has been completed. However, the results are shown analytically to be feasible and they unquestionably confirm the theoretically predicted superiority of lithium over hydrogen as a propellant for a plasma engine.

The second phase of the program will concentrate on investigation of the tank pressure effects, evaluation of other alkali propellants, evaluation of a new bipropellant concept, minimization of the weight penalty of the required magnetic field, development of 1.0- and 100-kW thrustors, continued analytical investigations, refinement of measurement techniques, and a longer duration (50-hr) endurance demonstration.

HAROLD L. BRIGGS, Capt. USAF, Acting Chief, Propulsion and Power Branch, Aerospace Power Division

CONTENTS

CONTENTS (contd)

ILLUSTRATIONS

ILLUSTRATIONS (contd)

ILLUSTRATIONS (contd)

ILLUSTRATIONS (contd)

LIST OF SYMBOLS

A	Area
A_R	Radiator area
B	Magnetic field strength
B_o	Absolute value of magnetic field strength
B_z	Axial component of magnetic field strength
C_A	Concentration of solute in phase A
C_B	Concentration of solute in phase B
$(C_B)_S$	Solubility of oxygen in B
$(C_A)_S$	Solubility of oxygen in A
$\|e\|$	Absolute charge of electron
ΔF^o_+(A Oxide)	Standard free energy of formation of the oxide of A which can be in equilibrium with a solution of oxygen in A
ΔF^o_+(B Oxide)	Standard free energy of formation of the oxide of B which can be in equilibrium with a solution of oxygen in B
G'	Coil geometric factor
g	Acceleration of gravity
ΔH	Total enthalpy rise $\left[\Delta h_v + (h_2 - h_1) + (h_4 - h_3)\right]$
Δh_v	Latent heat of vaporization
h_1	Enthalpy of liquid in feed system
h_2	Enthalpy at saturated liquid state

LIST OF SYMBOLS (contd)

h_3	Enthalpy at saturated vapor state
h_4	Enthalpy of vapor at 3000°C
I	Current
I_A	Arc current
I_c	Coil current
I_{sp}	Specific impulse $T/\dot{m}g$
I_{sp}^o	Reference specific impulse, $\frac{1}{g}\sqrt{\frac{2 \mid e \mid V_t}{m_a}}$
j_θ	Current density
K_1	Slope of thrust versus current curve
L, ℓ	Length
m	Mass
m_a	Atomic (or ionic) mass
$\dot{m}_e$	Effective mass flow rate
$\dot{m}$	Mass flow rate
$\dot{m}_o$	Reference mass flow rate $\frac{4\pi m_a}{\mu_o \mid e \mid}\sqrt{\frac{2m_a V_I}{\mid e \mid}}$
n	Empirical function of $\dot{m}$ which relates anode power to current ($P_o = n\ I\ V_I$)
n_o	Value of n when $\dot{m} = \dot{m}_o$
P	Power
P_I	Arc power input
P_{IE}	Internal energy loss

LIST OF SYMBOLS (contd)

P_R	Power absorbed regeneratively
P_{ca}	Power lost to cathode
p	Pressure
P_c	Coil power
P_o	$\lvert e \rvert V_I n_o^2 \dot{m}_o / m_a$
P_a	Power lost to anode
p_t	Test chamber pressure
q	Heat flux
Q	Heat transfer rate or total heat transfer
Q_{max}	Maximum heat transfer rate
r	Radial coordinate
r_i, r_1	Inside radius
r_o, r_2	Outside radius
T	Thrust or temperature
V	Voltage
V_A	Arc voltage
V_I	Effective ionization potential
V_M	Magnet volume
W_T	System weight
w_{PS}	Power supply density
w	Density of magnet coil material
z	Axial coordinate

LIST OF SYMBOLS (contd)

α	Outside radius/inside radius or fraction of atoms ionized
β	Length/inside radius
γ, γ'	Heat transfer parameters
δ	Fin thickness
ϵ	Emissivity
η_T, η_o	Thrust efficiency = $T^2/2\dot{m}IV$
η_F	Frozen flow efficiency
λ	$\frac{\text{Coil conductor volume}}{\text{Coil total volume}}$ or packing fraction
ρ	Resistivity
σ	Stephan-Boltzmann constant
ϕ	Thermal conductivity integral
χ_A	Work function of anode material
ψ_e	$\omega_e \tau_e$, cycles per collision for electrons

1. INTRODUCTION

This report summarizes the results obtained during the first year of a three-year program aimed at developing the technology of arc jets to the point where it will be possible to build plasma thrustors capable of the following performance:

Power Input:	up to 300 kW
Specific Impulse:	1500 to 4000 seconds
Over-all Efficiency:	greater than 60 percent
Lifetime:	500 hours

The approach used has been the investigation and development of thrustors which rely predominantly on Hall current acceleration of lithium propellant. This report presents the thrustor performance measurements, endurance test results, characteristics of special test equipment and measurement devices, a thrustor performance analysis, an analysis of the thrustor cooling limitations, and a preliminary evaluation of the propulsion system weight increment resulting from the requirement of a strong magnetic field. The technical effort began in April 1964 and the first phase ended in March 1965.

The present investigation was begun after two types of electromagnetic arc jets had demonstrated the capability to efficiently accelerate hydrogen to an I_{sp} approaching 10,000 sec. The first type (Ref. 1) to achieve this arc jet performance breakthrough relied on interaction between the applied current and its induced magnetic field to accelerate the plasma. The second type was the Hall current accelerator (Refs. 2 and 3) in which an externally applied magnetic field is used to induce azimuthal currents which interact with the applied magnetic field to accelerate the plasma.

The hydrogen results paved the way for the use of the potentially more efficient alkali metal propellants, beginning with lithium in the

present program. The hydrogen performance showed that the electromagnetic mechanisms could accelerate plasma to higher kinetic energy per particle than had previously been achieved in electrothermal devices and to sufficiently high energies that heavier propellants could be used. It was clear that, given the latitude in the use of heavier propellants, the best choice would be an alkali because of their low ionization losses and ease of storage during long missions. Lithium appeared as the best choice among the alkalis because it has the lowest atomic weight, the highest regenerative cooling capability, and the highest second ionization potential.

Concurrently with this program, EOS in a parallel NASA program and other contractors with equivalent objectives have continued investigation of high-I_{sp} electro-magnetic arc jets with gaseous propellants (Refs. 4 through 12). Most of these parallel efforts apparently concentrated initially on the high-current self-induced magnetic field regime (Ref. 7 and 9); more recently the Hall current or applied-magnetic-field regime has also been included (Ref. 8 and 10). Also, one of these parallel programs is beginning to include lithium and other alkali metal propellants (Ref. 13) but as far as is known by the authors the present report and previous progress reports on this program (Refs. 14 and 15) are the first to present alkali metal arc jet performance data.

2. SUMMARY

This report presents the results of the first successful attempt in the United States to use alkali metal propellants in electromagnetic thrust devices. The program reported upon is a logical continuation of previous thrustor development efforts at Electro-Optical Systems in which gaseous propellants, notably hydrogen, have been accelerated in Hall current devices to specific impulses of over 10,000 sec, at power levels of from 1 to 300 kW. In the tests reported, lithium has been used exclusively as the propellant. Many configurations of engines have been tested. The best performance to date has been obtained with anode-feed engines which were tested in a stainless steel tank. The back pressure of ambient air was 10^{-2} to 10μ Hg. The specific impulse was varied over a range of 2000 to 7000 sec and the following thrust efficiencies were measured: 70 percent at I_{sp} of 5000 sec, 60 percent at I_{sp} of 4000 sec, 45 percent at I_{sp} of 3000 sec, and 30 percent at I_{sp} of 2000 sec.

The novel feature in this type of thrust device is the manner in which the electric discharge path extends far out into the wake of the exhaust gas. This mode of operation frees the engine from the so-called containment limit, the maximum enthalpy obtainable when a gas flow is heated in a channel which is coaxial with an electric arc. On the other hand, new problems are introduced which have required intensive investigation. The most critical problem is one involving the possible entrainment of ambient gas into the jet, thus recirculating the tank gas and causing serious error in the interpretation of the measurements. Since the importance of this problem was realized from the beginning, many tests have been conducted at as low a pressure as is presently possible with the EOS vacuum system (10^{-5} mm Hg). Also the thrust level and other important parameters have been measured as a function of tank pressure

by bleeding gas into the tank. In a parallel program (performed under Contract NAS3-5909 for NASA/Lewis) a special low mass-flow-rate engine was built and tested in a Lewis facility at a pressure of about 5×10^{-5} mm Hg. To date, the results of all these tests indicate that engine performance measured at pressures of 1-6μ Hg does not degrade as the pressure is lowered to the order of 10^{-5} mm Hg. Further tests – in progress and planned – will help determine the nature of the vacuum facility necessary to carry out meaningful and accurate measurements.

The power necessary to produce the applied magnetic field must eventually be included in the computation of the thrust efficiency. This requires that minimum-power magnets be designed and tested. An analytical study of electromagnet cooling techniques and design parameters for use in thrustor systems has been made and is presented in Appendix I.

Some tentative analytic results are presented to explain the current-voltage characteristics of thrustors using Hall current acceleration. A concept of so-called effective mass is introduced and is defined as the propellant flow rate required for the discharge to operate at minimum voltage. This concept predicts that if the mass flow rate is held constant and the current changed, then at low currents part of the propellant is rejected by the discharge. At higher currents the discharge will attempt to entrain mass to maintain the potential drop low. It is hoped that further development of this analysis will clarify the problem of mass entrainment and lead to criteria for detecting its presence.

A detailed description is given of the design and development of a liquid feed system for lithium. The system is capable of feeding lithium at a controlled rate of from 0.001 to 0.5 sec. The bellows which contains 200 grams of lithium is maintained in a constant-temperature, constant-pressure environment inside a stainless steel cylinder. Reliable performance has been obtained from this system throughout the program.

It is felt that the results obtained to date indicate that electromagnetic thrustors using alkali metal propellants show real potential as useful space propulsion engines. However, considerable development work is still needed and is being diligently pursued at EOS and elsewhere.

3. THRUSTOR PERFORMANCE MEASUREMENTS

This section presents the overall thrustor performance measurements primarily in terms of the thrust efficiency and specific impulse characteristics. The specific impulse was calculated from the measured thrust and mass flow rate values using the following equation:

$$I_{sp} = \frac{T}{\dot{m}g} \tag{3-1}$$

The thrust efficiency was calculated from the measured arc power input, in addition to the measured thrust and mass flow rate:

$$\eta_T = \frac{T^2}{2\dot{m} P_I} \tag{3-2}$$

where

$$P_I = I_A V_A \tag{3-3}$$

It is to be noted that the power input in the above equation does not include

1. Power dissipated in the magnet coil (about 22 kW at the maximum coil current of 1,800 amperes);
2. Power required to operate the lithium feed system and to maintain the lithium at its melting point; and
3. Power in the lithium where it enters the thrustor.

The coil power was not included because the development of low-power coils is beyond the present scope of this program. The coil designs used were dictated by the criteria of maximum fabrication

simplicity (i.e., low cost) and an optimum match to the voltage-current characteristics of an existing magnet power supply. The calculation in Appendix II shows that the same field could be produced with a power dissipation of only 3.3 kW by a coil of more efficient design.

3.1 Performance of Best Thrustor Configurations

The highest thrust efficiencies in the specific impulse range of 2,000 to 5,000 seconds were measured with Models LAJ-AF-2 and AF-3. The anode-fee thrustors all gave higher efficiencies than cathode-feed thrustors at the same specific impulse, and the short-cathode versions (AF-2 and AF-3) performed better but had more erosion than the extended-cathode versions (AF-4, -6 and -8). Test data are given in Appendix III.

Thrust efficiencies of Model LAJ-AF-2 which is described in detail in Section 7, varied from 20 percent at I_{sp} of 1,500 sec to 70 percent at I_{sp} of 5,500 sec. These measurements were made with the test chamber pressure in the range of 1 to 10μ Hg. The power input was varied from 5 kW to 25 kW with mass flow rates of 0.01 and 0.02 gram per second. Figure 3-1 is a plot of the efficiency as a function of specific impulse, showing both the measured data and the theoretical efficiency as calculated in Section 9. The apparent scatter in the data of Fig. 3-1 is caused primarily by changing modes of attachment of the arc to the electrodes (especially the cathode) rather than by random errors in the measurements.

Above a power level of about 25 kW the cathode and the anode-cathode insulator eroded. The arc did not attach to the tip of the conical cathode, as preferred. It attached on the conical surfaces and even the cylindrical surface behind the base of the cone. There was no erosion of the anode, which appeared to be adequately cooled by the lithium and the graphite radiation disk.

The voltage of Model LAJ-AF-2 varied between 35 and 55 volts as shown in Fig. 3-2, where voltage is plotted as a function of specific impulse. Also shown is a theoretical estimate of the voltage based on

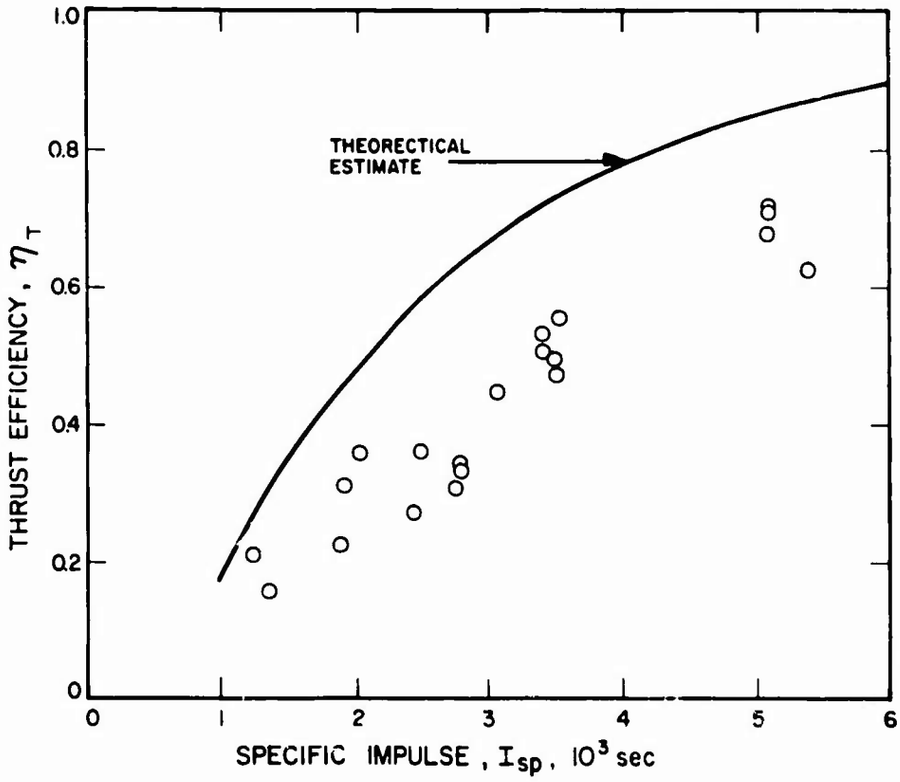

FIG. 3-1

THRUST EFFICIENCY AS A FUNCTION OF SPECIFIC IMPULSE FOR LITHIUM ARC JET MODEL LAJ-AF-2

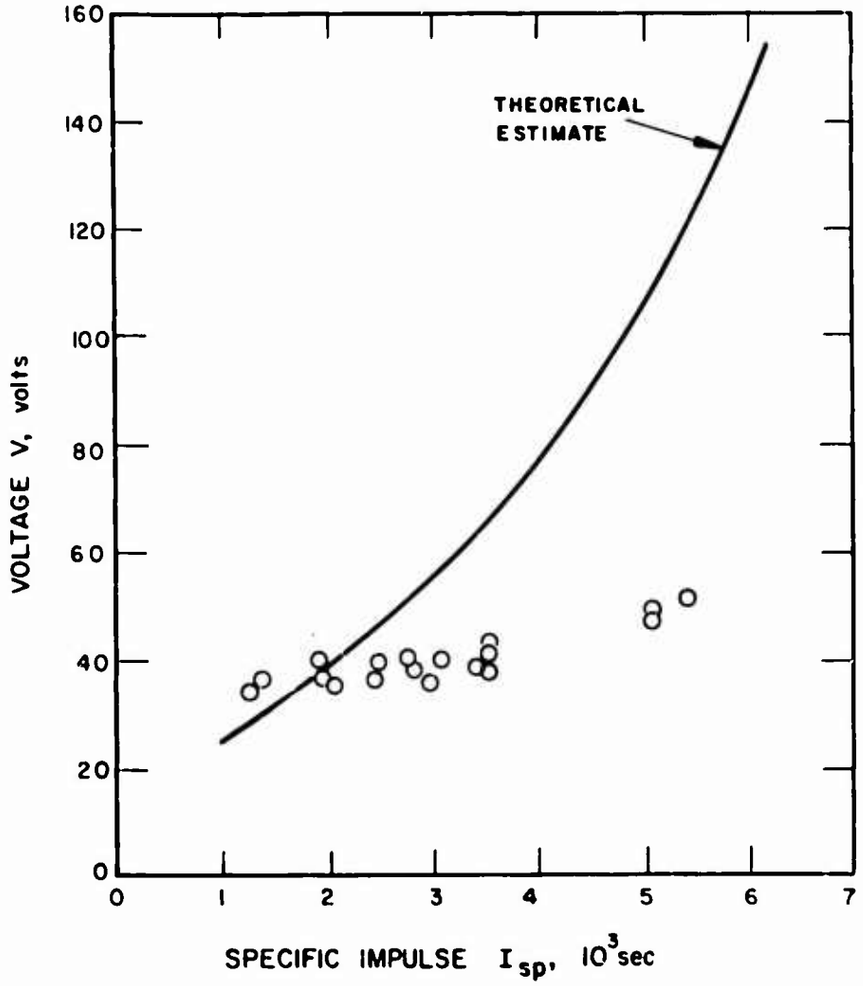

FIG. 3-2

ARC VOLTAGE AS A FUNCTION OF SPECIFIC IMPULSE FOR LITHIUM ARC JET MODEL LAJ-AF-2

the assumption that the average kinetic energy per ion leaving the interaction region of the discharge corresponds to that of a single ion falling through the voltage difference across the electrodes less the ionization potential and the potentials representing losses to the electrodes (Section 9). This is implicit in the assumption that the discharge current is given by

$$I_A = |e| \frac{\dot{m}}{m_a} \quad . \qquad (3\text{-}4)$$

It remains to be proven whether or not the current has such a limit and consequently whether or not the average velocity can be "anomalous" (i.e., higher than that corresponding to the arc potential difference). As Fig. 3-2 shows, the data from the Model LAJ-AF-2 thrustor are "anomalous" above a specific impulse of 2,000 sec.

The measurements may or may not be correct for the reasons given in Section 8. Additional measurements at lower test chamber pressure are necessary. If the present results are erroneous then, as the tank pressure is decreased, the voltage should increase or thrust should decrease.

The thrust efficiency of Model LAJ-AF-3 was, at the same specific impulse, about the same as that of Model LAJ-AF-2. As Fig. 3-3 shows, the thrust efficiency was about 20 percent at 2,000 sec, 40 percent at 3,000 sec and over 60 percent at 4,000 sec. This thrustor, described in detail in Section 7, was identical to Model LAJ-AF-2 except for the cathode configuration. Model AF-2 had a conical cathode and Model AF-3 had a conical cavity at the cathode tip.

These variations in cathode configuration were made in trying to achieve a more stable and confined mode of attachment of the arc to the cathode. As described above, the arc did not attach to the tip of the conical cathode (Model LAJ-AF-2) as preferred. It attached non-uniformly on the conical surface and on the cylindrical surface behind

the base of the cone. With the conical-cavity cathode (Model LAJ-AF-3) the arc attached both inside the cavity and outside on the external cylindrical surface as well as at the rim of the cavity. The arc was stable inside the cavity.

High vacuum tests with Model LAJ-AF-3 indicated that the thrust was not affected by decreasing tank pressure from about one micron-Hg to about 5×10^{-5} mm Hg. These results were observed in the 6-ft diameter x 6-ft overall length test chamber which was connected to a diffusion pump. Pressures of about one micron were measured with the thermocouple gages and a McLeod gage. The lower pressures were measured with ion gages. All pressure measurements are uncertain because of the unknown composition of the gas at the sampling points.

3.2 Performance of Anode-Feed Thrustors with Extended Cathodes

The extended-cathode versions of the anode-feed thrustors are Models LAJ-AF-4, AF-6A through 6B and AF-8, all of which are described in detail in Section 7. These models were less efficient than the AF-2 and AF-3 models, but were more efficient than the cathode-feed thrustors, and operated with less insulator erosion than any of the other thrustors.

Model LAJ-AF-4 was operated over a higher range of specific impulse from about 4,000 to 8,000 sec. Its thrust efficiency, as Fig. 3-4 shows, is about 40 percent at I_{sp} of 4,000 sec, 60 percent at I_{sp} of 6,000 sec and 80 percent at I_{sp} of 8,000 sec. It is to be noted that, at about 4,000 sec, its efficiency is lower than that of Models LAJ-AF-2 and LAJ-AF-3. Performance points for Models LAJ-AF-6 and AF-8 are also shown in Fig. 3-4 for comparison. Any differences between these models appear to be within the scatter of the data.

The thrust of Model LAJ-AF-1 was not measured because this thrustor was mounted vertically to prevent liquid lithium from forming a short-circuit across the electrodes. Observations of the operation

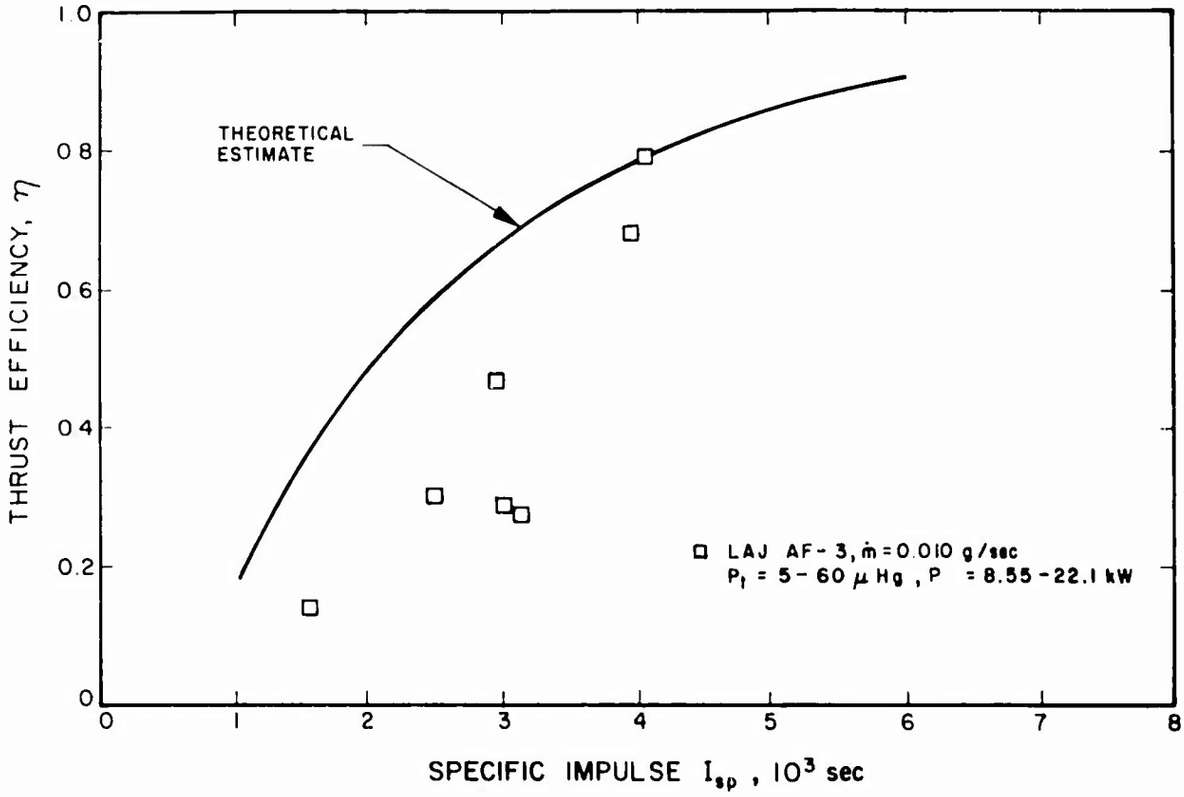

FIG. 3-3 PERFORMANCE OF LITHIUM ARC JET MODEL LAJ-AF-3

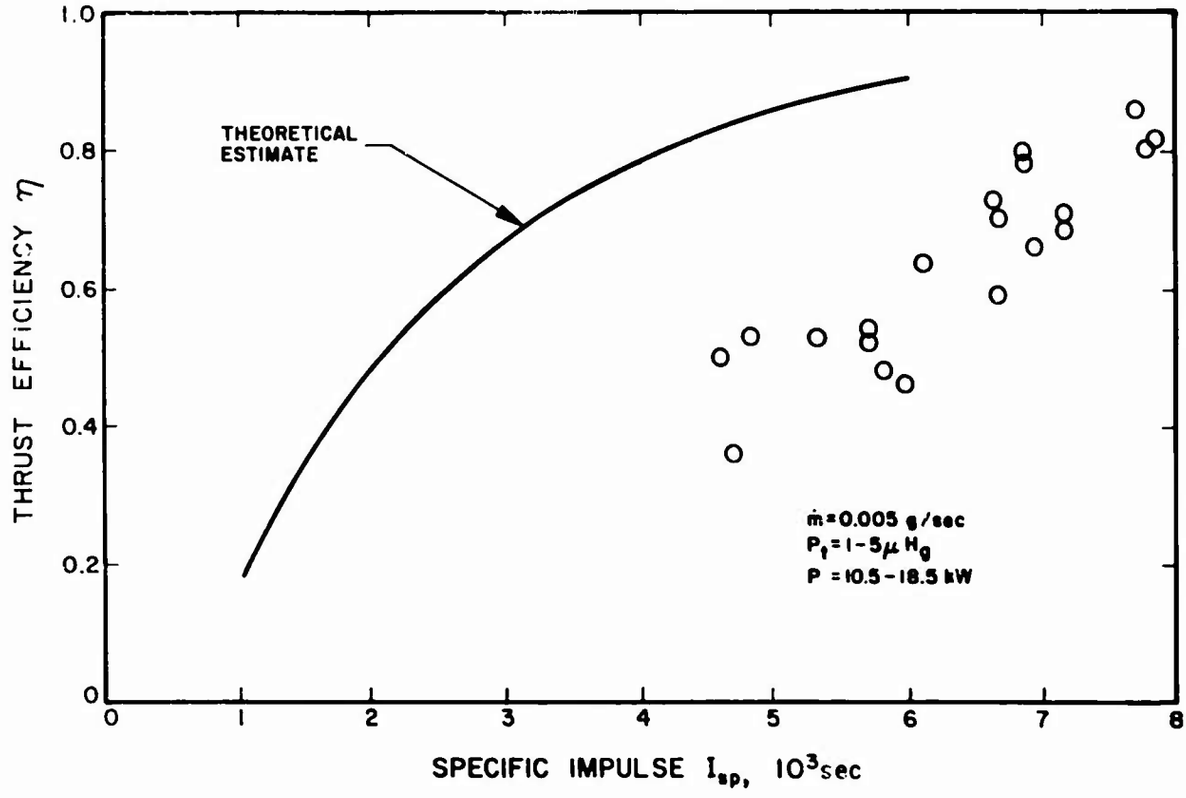

FIG. 3-4 PERFORMANCE OF LITHIUM ARC JET MODEL LAJ-AF-4

however indicated that the arc attached to the anode inside of the injection slot and thus the inside section (Section 7, Fig. 7-2) of the anode ran at a much greater temperature than the outside section. The arc voltage of this thrustor was about 30 volts.

3.3 Performance of Cathode-Feed Thrustors

The thrustors with lithium injected through their cathodes were models LAJ-CF-1 through CF-5. These were all tested in the 3-ft-diam x 6-ft-long vacuum chamber. Models CF-4 and CF-5 were tested on the thrust balance. The thrust target was used to measure the thrust of Model CF-3.

Models LAJ-CF-1 and CF-2 were tested in a vertical position and hence, thrust measurements were not made. Tests without thrust measurement gave the following results:

1. The effect of anode diameter on arc voltage with lithium injection at the cathode.
2. General arc characteristics and behavior (e.g., arc stability, approximate attachment area at electrodes, and voltage-current characteristics).
3. Comparison of anode injection to cathode injection of lithium.
4. Techniques for controlling the experiment - in particular, starting, shutdown, and feed rate control techniques.

The specific impulse and thrust efficiency measured with Model LAJ-CF-3 could have significant errors. Thrust was measured with a target collector-balance which, from visual observations did not appear to completely collect the jet, particularly at pressure levels in the tank below about one mm-Hg. Under some conditions, the discharge appeared to be partly attached to the target.

Figures 3-5 and 3-6 show the measured performance of Model CF-3. The specific impulse varied between 1,700 and 4,700 sec, with arc power input between 9 and 31 kW. Thrust efficiency varied between 10 and 64 percent.

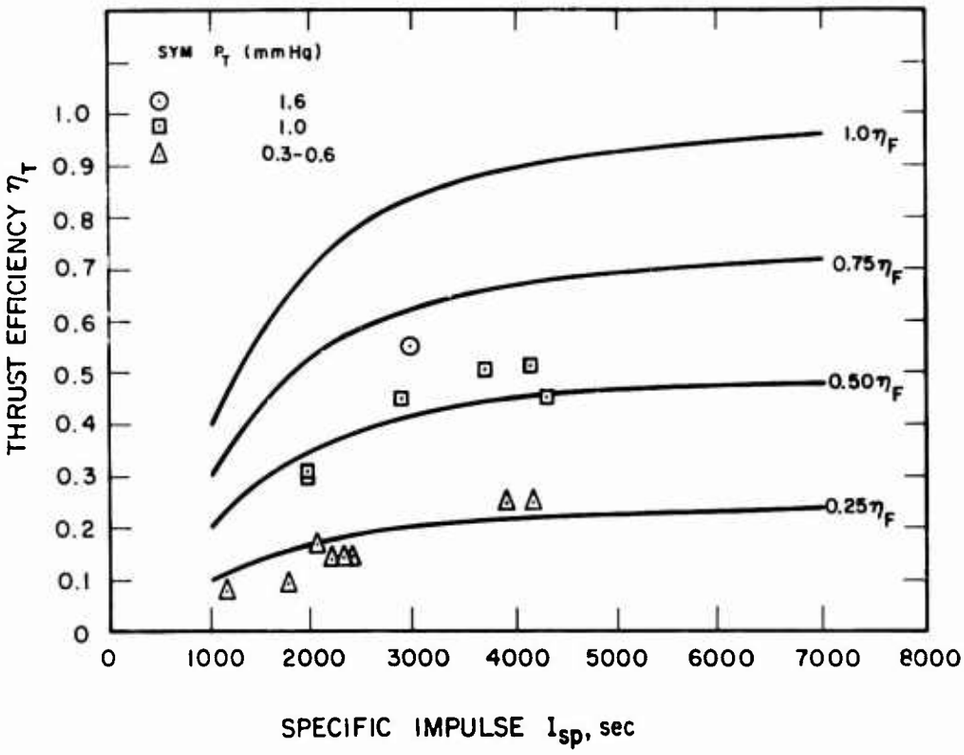

FIG. 3-5

THRUST EFFICIENCY AS A FUNCTION OF SPECIFIC IMPULSE FOR LITHIUM ARC JET MODEL LAJ-CF-3

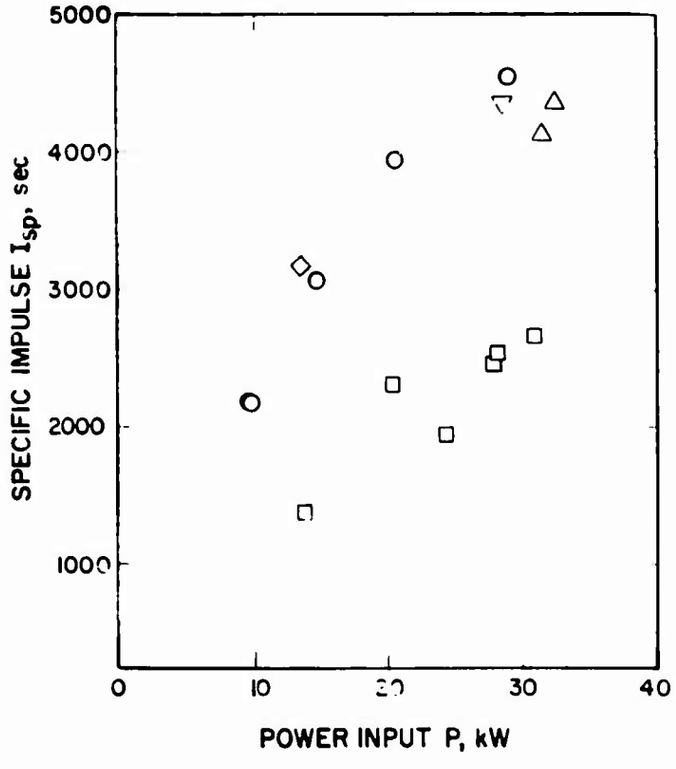

FIG. 3-6

SPECIFIC IMPULSE AS A FUNCTION OF POWER INPUT FOR LITHIUM ARC JET MODEL LAJ-CF-3

For reference, Fig. 3-5 shows the theoretical functions $0.75\ \eta_F$, $0.50\ \eta_F$, and $0.25\ \eta_F$, where η_F is the theoretical frozen-flow efficiency. This is based on complete first ionization and the frozen-flow includes the energy required to vaporize lithium. It is to be noted that the measured efficiency (at constant tank pressure) has the same trend with specific impulse as the theoretical frozen-flow efficiency.

Figure 3-6 indicates that the performance may be adversely affected by decreasing the tank pressure. As mentioned above, this may be an erroneous indication caused by incomplete collection of the jet by the target at the lower pressures. Visually, this appeared to be the case; thus the thrust balance measurements at varying pressure are a better indication of the pressure effect. There are, however, other effects which could conceivably give the observed results. These are discussed in Section 5.

When the Model LAJ-CF-3 thrustor was operated with mixtures of lithium and hydrogen, the higher efficiency of lithium was directly demonstrated. The results show that the introduction of hydrogen reduced the thrust level for the same power input. If the efficiency had remained constant, the thrust would have increased as the square root of the total mass flow rate (Eq. 3-2). Figures 3-7 and 3-8 show the results in terms of thrust as functions of current and power, respectively, for various levels of the hydrogen flow rate. The lithium flow rate was about 0.01 g/sec; the value is not known exactly because of malfunctions of the feed system during this run.

As current and power were increased, there was an increase in the ratio of thrust with lithium and hydrogen to thrust with lithium only. These effects are caused by the loss of energy due to dissociation of the hydrogen. As power was increased, the hydrogen temperature increased and the percentage of the total energy in dissociation became lower. Hence, the efficiency increased.

Figure 3-9 shows the effect of hydrogen injection on the voltage-current characteristics of the Model LAJ-CF-3 arcjet. With

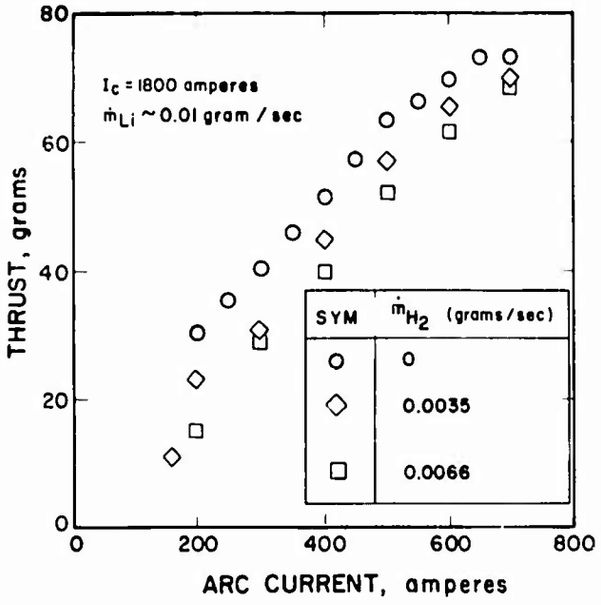

FIG. 3-7

THRUST AS A FUNCTION OF CURRENT FOR MODEL LAJ-CF-3 WITH LITHIUM AND HYDROGEN

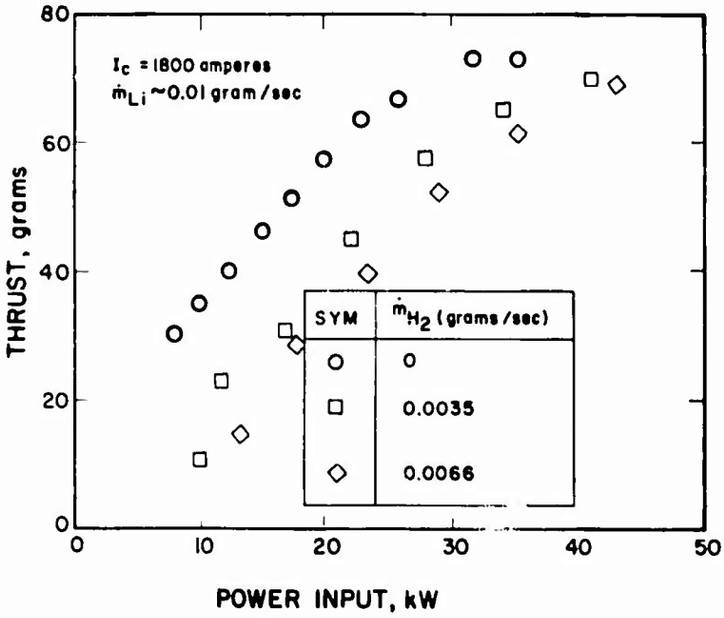

FIG. 3-8

THRUST AS A FUNCTION OF POWER INPUT FOR MODEL LAJ-CF-3 WITH LITHIUM AND HYDROGEN

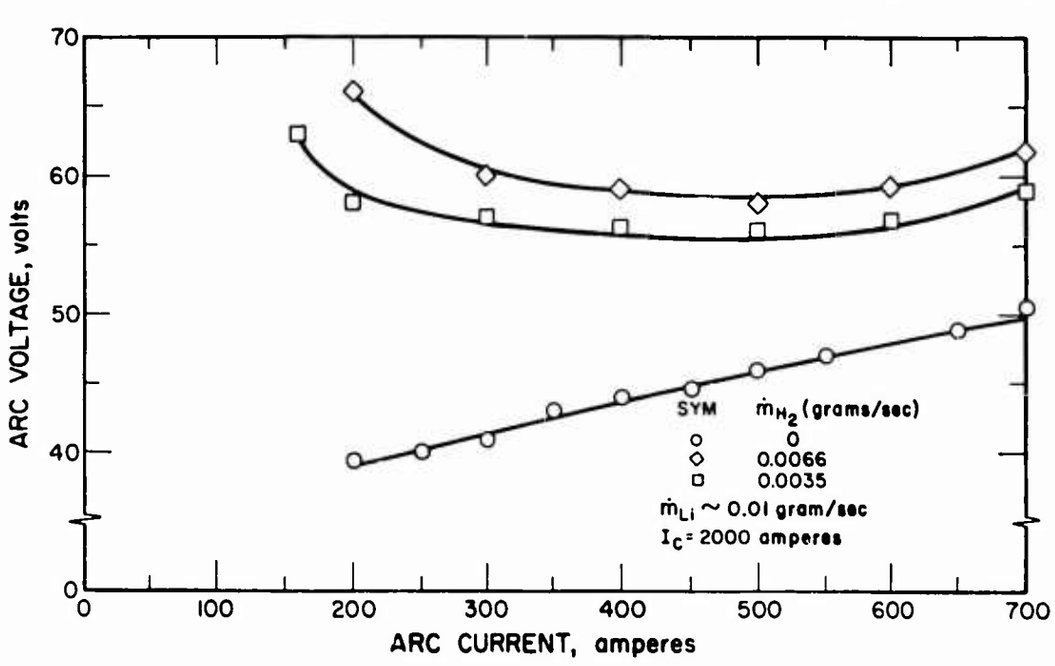

FIG. 3-9 ARC VOLTAGE AS A FUNCTION OF ARC CURRENT FOR MODEL LAJ-CF-3 WITH LITHIUM AND HYDROGEN

pure lithium, the arc voltage increased approximately linearly with arc current. The general level of voltage increased when hydrogen was injected. The voltage decreased with current below about 500 amperes, where the voltage was at a minimum. Above about 500 amperes, the voltage increased with increasing current.

The observed effects of magnetic field strength seem to indicate that the thrust of the lithium arc jet is due primarily to Hall current interactions. Figures 3-10 and 3-11 show the effect of magnet coil current on specific impulse and voltage for constant values of arc current, lithium flow rate, and tank pressure (At a coil current of 2,000 amperes, the magnetic field strength is about 4,000 gauss in the vicinity of the electrodes). Both the thrust and voltage increased approximately by a factor of five when the field strength was increased from zero to 5,000 gauss.

Reliable direct performance measurements with Model LAJ-CF-4 were not obtained due to malfunctions of the balance and instabilities of the lithium feed rate.

Figure 3-12 shows thrust efficiency as a function of specific impulse for Models LAJ-CF-4b and CF-5. Thrust efficiency varied from about 10 percent at I_{sp} of 1,500 sec to about 55 percent at I_{sp} of 8,500 sec. The performance characteristics for these two models appear to be alike, although the operation of CF-5 was more stable and its performance data have less scatter. After some improvements had been made on the thrust balance, it performed satisfactorily during the tests of Model CF-5. Several measurements were repeated and the results agreed within a few percent.

The power input for these tests was varied between 6 and 36 kW. Above about 20 to 30 kW, depending on mass flow rate, the anode overheated and the insulator between the anode and cathode began to erode.

The cathode of Model LAJ-CF-4 thrustor was modified to form the CF-4b Model. The modification consisted of relocating the lithium

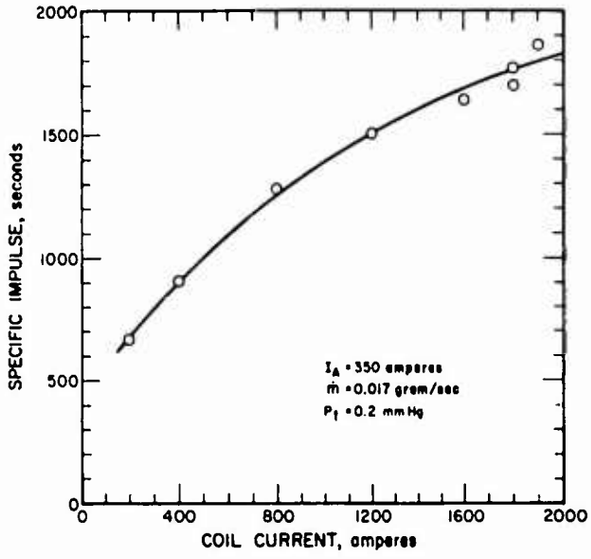

FIG. 3-10

EFFECT OF MAGNET COIL CURRENT ON SPECIFIC IMPULSE OF MODEL LAJ-CF-3

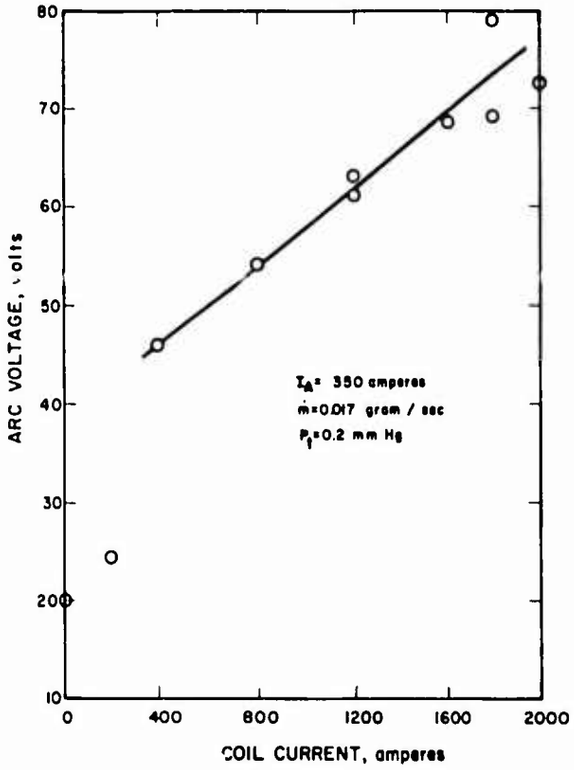

FIG. 3-11

EFFECT OF MAGNET COIL CURRENT ON ARC VOLTAGE OF MODEL LAJ-CF-3

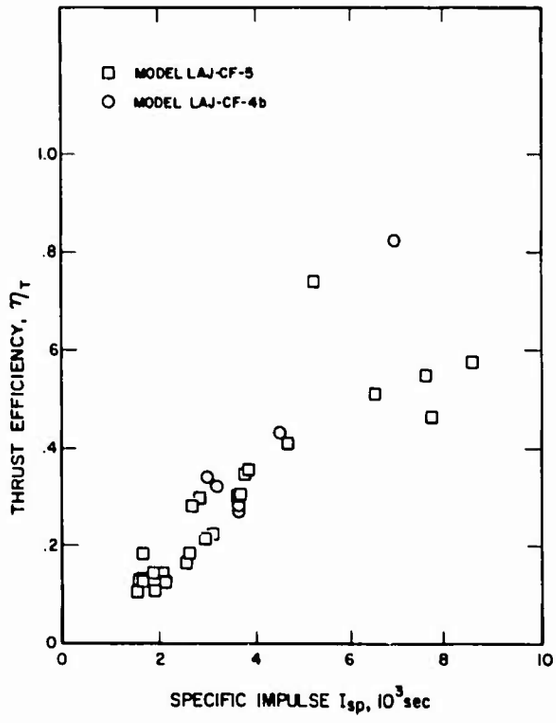

FIG. 3-12

THRUST EFFICIENCY AS A FUNCTION OF SPECIFIC IMPULSE FOR MODELS LAJ-CF-4b AND CF-5

flow restriction plug farther from the arc to maintain the vapor front downstream of the plug. This improved the stability of the feed rate; however, the distribution of current at the cathode surface continued to be unstable and nonuniform. The arc frequently attached along the side of the cathode surface instead of in the preferred region near the axis. This caused severe erosion of the insulator.

Model LAJ-CF-5 was designed with a cathode configuration intended to promote a more uniform and stable arc at the cathode surface. As Fig. 7-6 in Section 7 shows, the cathode tip has a tapered hole in which the arc tended to attach. Lithium was injected into the base of this tapered cavity. Operation of this thrustor was considerably more stable and uniform than that of CF-4b.

4. THRUSTOR ENDURANCE

4.1 Ten-Hour Endurance Test

Lithium arc jet Model LAJ-AF-6D was endurance-tested for 9.33 hours with 10-kW power input. The specific impulse and thrust efficiency were 4950 sec and 53 percent, respectively. Prior to that run, the same engine was tested for about one hour in substandard-performance condition. The endurance test was stopped after the lithium in the feed system was all used. The cathode and cathode-anode insulator eroded considerably at the end of the run after the lithium flow stopped and before the arc was turned off. Therefore, the weight-loss measurements given below are not representative of the erosion rate occurring during the run. Erosion was also observed at the beginning of the run before stabilization of the lithium flow rate.

The operating conditions and other pertinent data for the endurance test are summarized as follows:

Model No.	LAJ-AF-6D
Run Duration	9.33 Hours
Duration of previous run with same thrustor	0.91 Hour
Total time on thrustor	10.24 Hours
Power Input	10 kW
Current	250 amperes
Voltage	40 volts
Lithium mass flow rate	4.53×10^{-3} g/sec
Test chamber pressure	6μ Hg
Cathode and insulator weight loss	5.6 grams
Anode weight increase	0.43 gram
Net electrode and insulator weight loss	5.2 grams
Ratio of weight loss to total propellant	0.028
Thrust	22.5 grams
Thrust efficiency (not including coil power)	53 percent
Specific Impulse	4950 sec

At the beginning of the one-hour run the lithium feed system was pressurized excessively and liquid lithium flowed into the space between the anode and cathode. This caused the arc path to be too short (a few millimeters) and the voltage to be too low (15 to 20 volts) for good performance. The one-hour run was continued until the excess lithium vaporized.

4.2 Endurance Potential and Problem Areas

From the erosion and endurance test results obtained so far with lithium, it is not possible to make accurate predictions about the eventual life of alkali metal arc jets. However, the lithium results are encouraging — particularly the lack of any measurable anode weight loss during the 10-hour endurance test. These results show that tungsten at high temperatures (up to 2000°C) is not severely attacked by the lithium vapor. The principal endurance problem with the thrustors tested in Phase I was the insulator. This problem will be solved by one or both of the following measures:

1. Use of an insulator material which will resist lithium better at high temperatures than boron nitride or alumina — the only two insulator materials tried so far.
2. Evolution of a cathode design which will stabilize the arc in a region farther away from the insulator. (The bipropellant buffered cathode thrustor, Model LAJ-AF-5, is one design which accomplishes this.)

Insulator materials with better resistance to lithium than boron nitride or alumina are beryllia, thoria, and yttria. These will be evaluated in the second phase of this continuing program. The problem of materials compatibility with lithium is discussed in detail in Appendix IV.

5. UNCERTAINTIES IN THE PERFORMANCE RESULTS

This section discusses certain questions regarding the validity of the performance results presented in Section 3. The question here is not accuracy of the measurements - this is discussed in Section 6 - but, rather, how well the conditions of outer space were simulated for the Hall arc jet.

These questions were easily resolved for electrothermal arc jets which produce thrust as a result of heating and expansion processes occurring inside the thrustor. However, the electromagnetic arc jets, either of the Hall current type or self-induced magnetic field type, rely on thrust mechanisms which apparently occur outside the confines of the thrustor itself. Therefore, two effects - which are not completely resolved at present - become important:

1. Effect of test-chamber ambient gas (i.e., effect of test chamber pressure)
2. Effect of the test chamber itself on the operation and performance of the thrustor.

The effects of test chamber pressure and size on performance of the Hall arc jet should be further investigated by

1. Additional high vacuum tests
2. Tests in various sized chambers or with a "false" chamber wall which can be placed at various positions downstream of the thrustor
3. Additional measurements of the axial current distribution at various chamber pressure levels in tanks of different sizes.

5.1 Effect of Test Chamber Pressure

At test chamber pressure levels greater than about 10μ Hg, the thrust and voltage of the lithium arc jet varied as the pressure. Figure 5-1 shows thrust of Models LAJ-AF-4 and -6 as a function of test chamber pressure. Also, the arc voltage of Model LAJ-CF-5 decreased by about 25 percent as atmospheric air was bled into the vacuum pipe downstream of the tank to increase the chamber pressure. When a small amount of argon was bled into the tank, the voltage and thrust decreased by a factor of about 3 to 4. These effects were caused by entrainment of some of the tank gas in the discharge region at tank pressure levels of the order of 1 mm Hg.

At test chamber pressure levels below about 10μ Hg, there is evidence that the thrustor performance is not adversely affected by pressure. Tests of a 10-kW hydrogen Hall current accelerator did not show a measurable effect of pressure at pressures between 10^{-3} mm Hg and 10^{-5} mm Hg (Ref. 5). This hydrogen accelerator was tested in an EOS 3-ft-diam x 6-ft-long test chamber and then in the 15-ft-diam x 50-ft-long chamber at the NASA/Lewis Research Center. Tests at EOS were made with the chamber pressure between 10^{-2} and 1.0 mm Hg. Unfortunately, results (shown in Table 5-I) from the two facilities at the same pressure do not agree and because of the lack of agreement, in addition to uncertainties in the thrust measurements at NASA/Lewis, the results of these tests are not conclusive.

Tests with the lithium arc jet were made at pressures in the 10^{-5} mm Hg range, but these too are not conclusive because of the relatively short period over which the high vacuum could be sustained. The lithium tests did, however, indicate that the thrust did not change significantly between 10μ Hg (indicated on a McLeod gage) and 5×10^{-5} mm Hg (indicated on an ion gage).

Gas entrained in the arc discharge region may affect the thrustor in any of the following ways:

1. Entrained gas may be accelerated along with the injected gas from the thrustor.

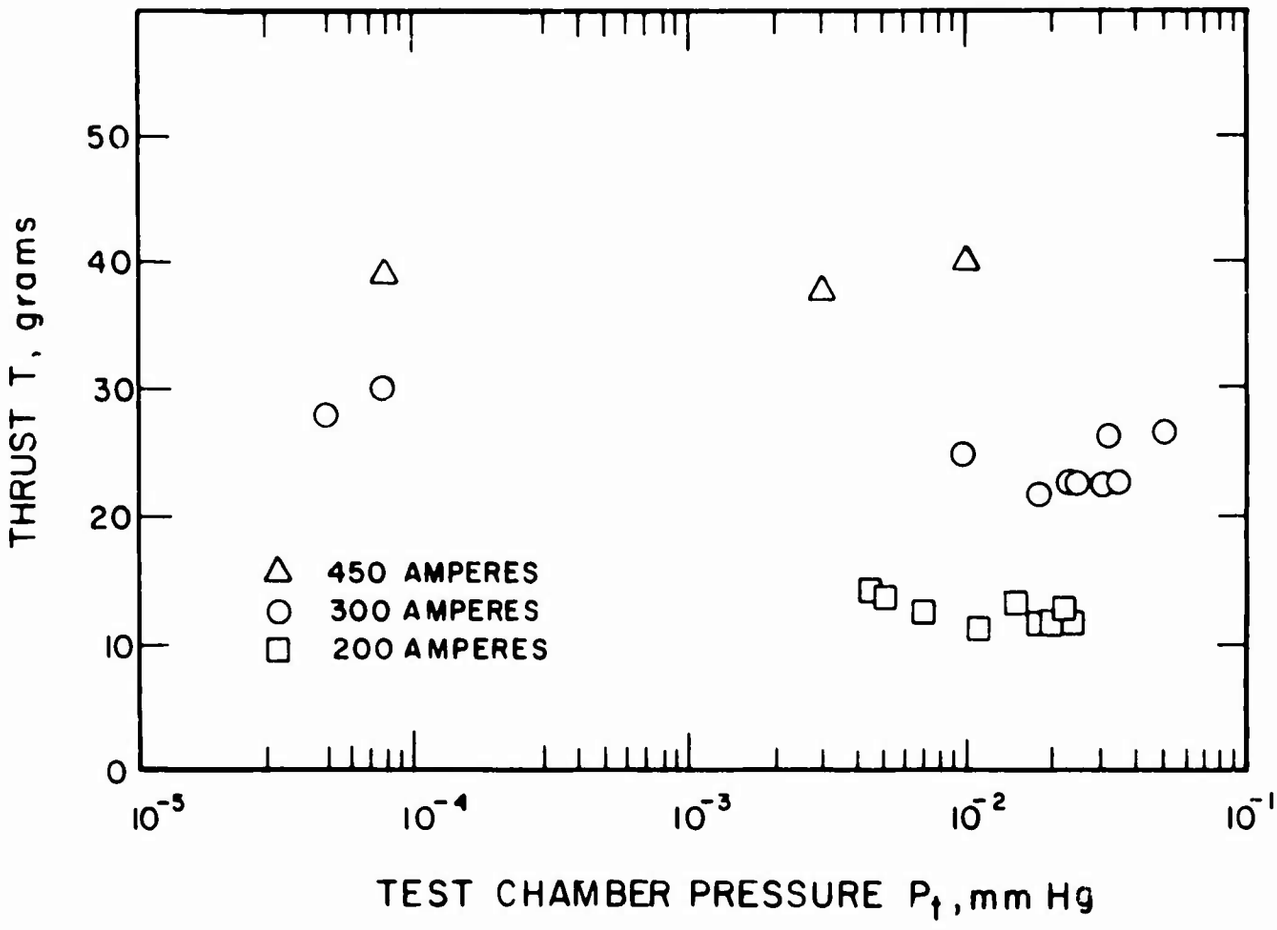

FIG. 5-1 THRUST AS A FUNCTION OF TEST CHAMBER PRESSURE FOR ANODE-FEED THRUSTORS WITH EXTENDED CATHODE (Models LAJ-AF-4 and -6)

TABLE 5-I

PERFORMANCE OF 10-kW HALL CURRENT ACCELERATOR

COMPARED AT HIGH AND LOW AMBIENT PRESSURES

$\dot{m}$ (mg/sec)	I_a (amperes)	I_m (amperes)	P_{IV} (kW)	P_t (mm Hg)	T (gf)	I_{sp} (sec)	η_o
*1.24	140	500	11.5	1×10^{-2}	8.6	6900	0.25
1.04	140	500	9.52	1.15×10^{-2}	4.0	3850	0.078
1.04	140	500		8×10^{-5}	4.4	4231	
1.4	120	500	7.56	1×10^{-3}	3.3	2360	0.049
1.4	120	500	7.69	5×10^{-5}	3.1	2210	0.043

*Test at EOS.

2. Ionization of entrained gas could provide a charged-particle density in the jet higher than that which would exist in space. This could cause the current distribution in the test chamber to be different from that in space.
3. Entrained gas may cause the flow and diffusion of neutral propellant atoms to be different from that which would exist in space.
4. There may be a contribution by entrained gas to the rate of recombination of the ions and electrons downstream of the discharge region. This would cause the propellant to escape the magnetic field in the test chamber sooner than it would in space.

The relative significance of the entrainment effects has not been established; however, the first two in the above list are probably more predominant.

5.2 Effect of Test Chamber Wall Proximity

The tank walls may affect the thrustor performance by influencing the scale of the arc discharge (i.e., the length of the current field extending into the jet), by electrostatic effects, and by shorting out part of the arc discharge. That the arc discharge of the Hall arc jet extends far afield of the thrustor itself has been verified by

1. Observed striations in the jet
2. Observation of the discharge with secondary electrodes downstream of the thrustor
3. Determination of the axial current distribution from measurements of the induced tangential magnetic field (Ref. 5).

It is possible that the current-carrying portion of the jet would extend farther in space than is allowed by the length of the test chamber. If that is so, the walls of the test chamber either shorten the discharge or carry part of the current. The wall could shorten the discharge without carrying current by providing a thermal

boundary layer due to its low temperature. Alternately, part of the current from the anode could flow into the test chamber wall, close the loop between the anode jet* and cathode jet,* and then flow through the cathode jet to the cathode. Such arcing to the tank wall has been suggested at times from observations of the discharge at very low chamber pressure and also from measurements of the chamber voltage. Under conditions where the cathode jet extends as far as the chamber wall, the test chamber potential is very close to the cathode potential. When the cathode jet does not extend to the chamber wall, the chamber potential is about midway between that of the anode and that of the cathode.

*Observed luminous streams of particles emanating from the cathode tip and generally from the inside edge of the anode.

6. PERFORMANCE MEASUREMENT TECHNIQUE

6.1 Thrust Measurements

The thrust of all anode-feed thrustors beyond Model LAJ-AF-1 and all cathode-feed thrustors beyond LAJ-CF-3 was measured with the thrustors and the feed system mounted on a thrust balance. The thrust of Model LAJ-CF-3 was measured with the thrustor mounted to the tank and with a target balance approximately 10 inches downstream of the thrustor. All models prior to LAJ-AF-2 and LAJ-CF-3 were tested in a vertical position and thrust measurements were not obtained. Thrust measurements with the target were only approximate because, at tank pressure levels below 1 mm Hg, part of the jet from the thrustor was not collected by the target. Some of the flow at tank pressure levels above 1 mm Hg may have passed into the target, reversed direction, and passed back out of the target. This would cause the thrust reading to be higher than the actual thrust. When the direct thrust balance was used, the magnet coil and the lithium feed system, as well as the thrustor, were mounted directly on the balance.

6.1.1 Balance Description

The balance suspension mechanism is a parallelogram which supports the bottom thrustor-mounting plate as shown in Fig. 6-1. The lower plate is connected to the upper fixed plate through three support members which have thin flexible sections at either end, to form flexural pivots. The thrust is sensed by the force transducer mounted on the lower plate and connected to a vertical tube which in turn is mounted to the upper plate. The balance is designed so that the principal stiffness (force resisting the applied thrust) is that of the transducer. A small fraction of the applied thrust is also resisted by the effective pendulum stiffness and the stiffness of the parallelogram suspension.

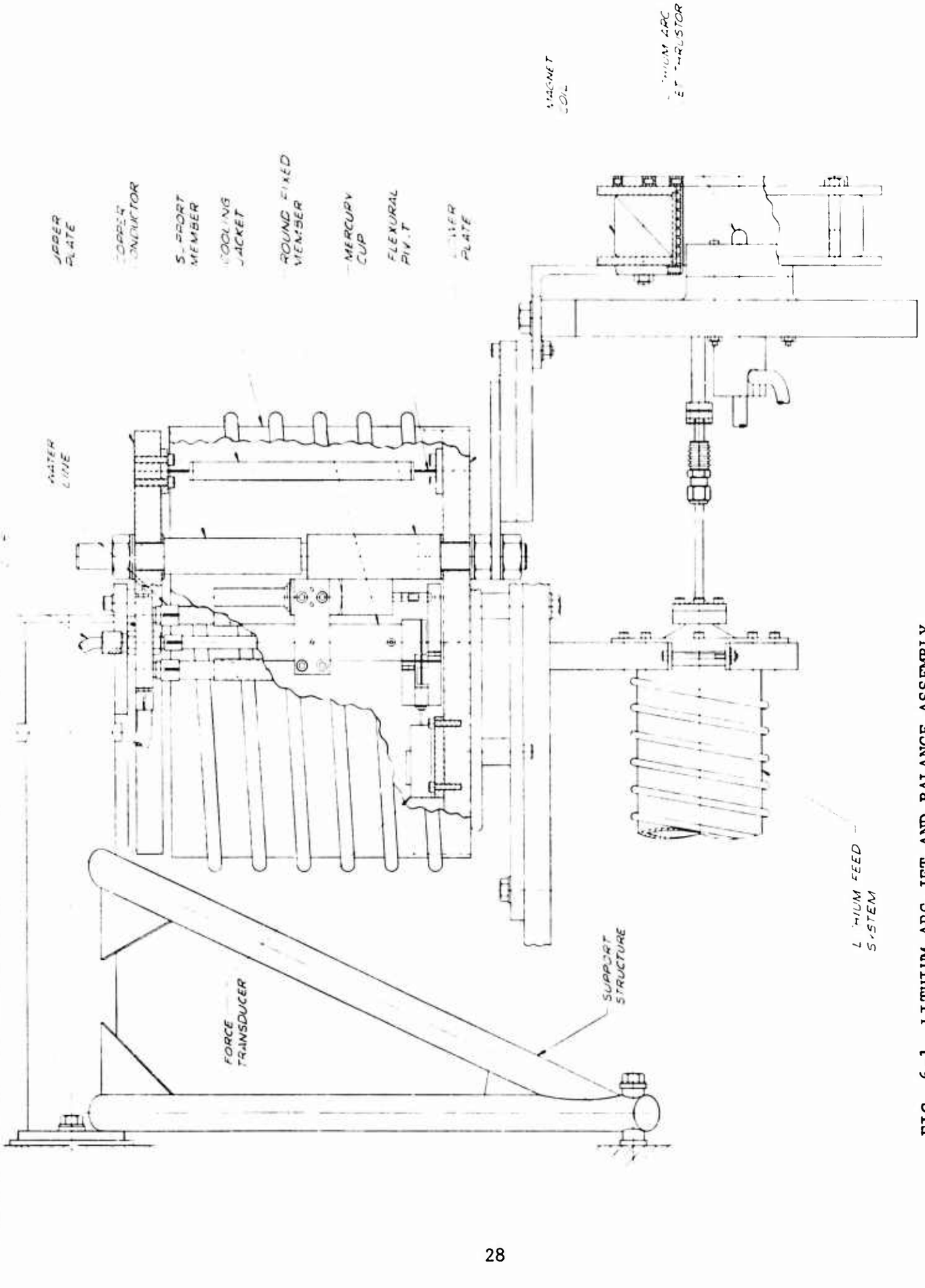

FIG. 6-1 LITHIUM ARC JET AND BALANCE ASSEMBLY

Power leads for the arc and magnet coil, gas and water leads, and power and instrumentation leads for the feed system are connected across the balance so as to minimize tare forces and errors. These tare forces are caused by current, water flow, and gas flow through the leads, in addition to gas and water pressure, and the temperature of these leads. The arc and coil power are carried across the balance through copper conductors suspended in cups containing liquid mercury. Gas and water are brought across the balance through flexible plastic hoses which are prestretched to insure vertical alignment. The power and instrumentation leads for the feed system are carried across the balance through helical copper wires (Fig. 6-2).

6.1.2 Accuracy

The estimated probable error in a thrust measurement is ± 1-2 grams. The principal source of error is drift of the zero-thrust reading of the transducer. This zero-drift is caused by distortion and shifting of the tank and balance suspension frame due to the nonuniform temperature distribution of the balance and tank structure. Other sources of zero-drift are temperature effects on the force transducer, and shifting of the relative positions of the magnet coil, the magnet coil leads, and thrustor power leads. Such a shift causes a change in the Lorentz forces between leads and between the leads and the coil itself. Other sources of thrust measurement error, such as hysteresis and changes of the force transducer sensitivity, are overshadowed by zero-drift.

In spite of occasional severe zero-drift (e.g., of the order of 10 grams thrust per hour) the error can be minimized by frequently shutting off the engine to obtain a zero reading. The thrust measurements are assumed to be valid when they are preceded by and followed by zero readings which are not different by more than 1 gram. In fact, even if the zero reading which preceded a given measurement differs by more than 1 gram from the zero reading following the measurement, that measurement may be valid.

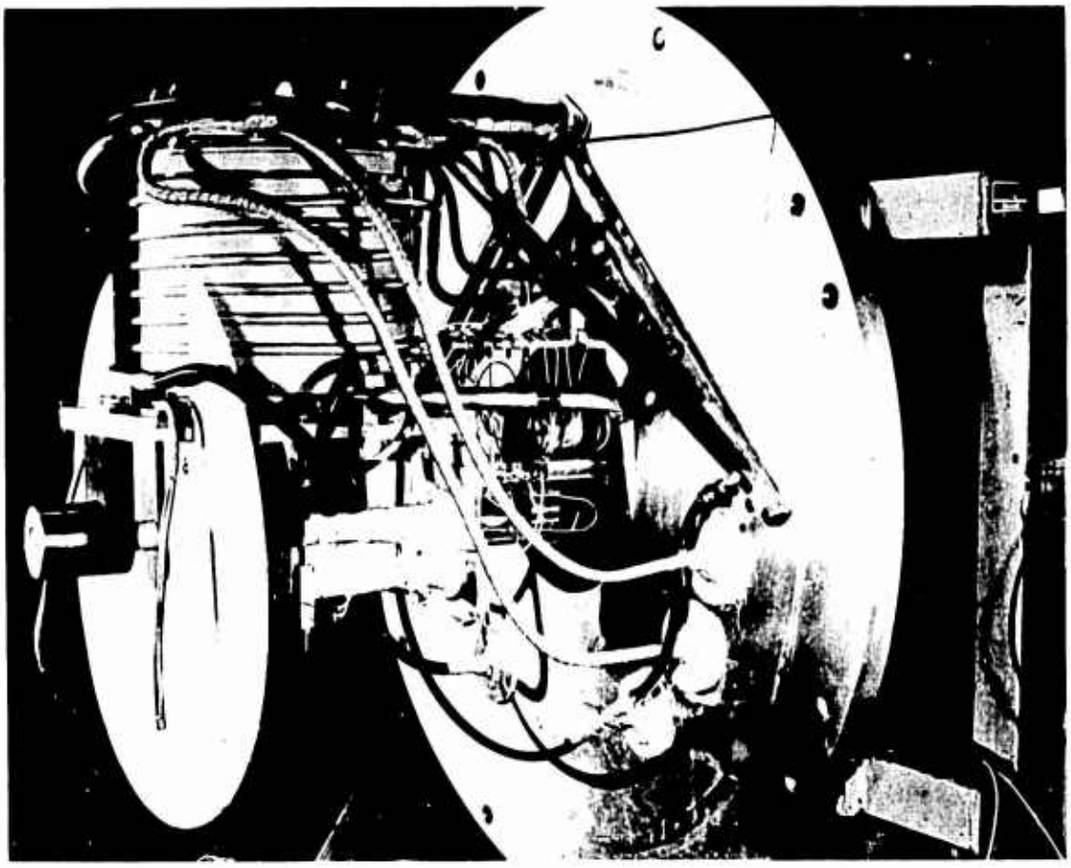

FIG. 6-2 LITHIUM ARC JET MODEL LAJ-CF-4 INSTALLED ON THRUST BALANCE WITHOUT MAGNET COIL

6.1.3 Balance Calibration Technique

Three types of calibrations are obtained for each thrustor run. These include measurement of the balance sensitivity, measurement of the tare force as a function of the magnet coil current, and measurement of the interaction tare force as a function of coil current and current through the arc power leads. The balance sensitivity (i.e., the relation between applied thrust and the voltage output of the transducer) is determined by a deadweight calibration in which gram weights are applied to the balance over a pulley. This deadweight calibration has been made with the magnet coil both on and off. It was found that the magnetic field has no effect on the sensitivity. After the sensitivity calibration has been made, the magnet coil current is set at various values and the thrust for each value is measured. To obtain the interaction tare force calibration, the thrustor electrodes are shorted out with a copper shorting fixture and and the arc current and the coil current are set at various values. The thrust for each set of values is measured. The magnet tare force is the largest of the tares; it normally is about 30 to 40 grams. The interaction tare is normally less than 10 grams for all values of arc current and coil current.

6.2 Lithium Feed System

The lithium feed system provides the means for control and measurement of the mass flow rate of the liquid lithium propellant. The feed system utilizes a cylindrical, nesting bellows to contain the lithium and force it into the thrustor. The force or pressure required to inject the lithium into the thrustor is provided by gas pressurizing the space surrounding the bellows. The lithium flow rate, which is proportional to the linear displacement rate of the bellows, is measured by the angular speed of a linear actuator connected to the end of the bellows.

6.2.1 Mass Flow Rate Accuracy

The flow rate measurement accuracy must be stated for both an instantaneous measurement and for an average measurement over a period of several minutes or longer. The probable error in an instantaneous mass-flow-rate measurement is about 10 percent or 10^{-3} g/sec, whichever quantity is larger. However, over a length of time greater than a few minutes, the average mass flow rate can be determined with a probable error of less than 5 percent.

This duality in the flow rate measurement accuracy is caused by dynamic effects in the feed system. The most accurate measurement is obtained when the temperature of the lithium inside the bellows is constant with time and when the pressure difference across the bellows (between the lithium inside the bellows and the surrounding gas) is also constant with time. Under these conditions the volumetric displacement rate of the bellows is a function only of the linear displacement rate or velocity of the end of the bellows. The preceding probable error estimates were based on the effective volumetric expansion rate caused by a rate of change of the temperature, and also on measurements of the bellows volume for various pressure differentials across the bellows.

6.2.2 Description of Feed System

Two feed systems of the same type were constructed during Phase I of the program. These are designated Mark I and Mark II. In both of these models the same type of nesting bellows was used. In the Mark I system the lithium is contained inside the bellows and the actuating gas pressure is applied between the outside of the bellows and a cylindrical tubular container. In the Mark II system the lithium is contained between the outside of the bellows and the tubular container.

6.2.2.1 Mark I Feed System

To minimize sag and buckling of the bellows, it is mounted inside a tubular container which is sealed so that gas

pressure can be applied between the container and the bellows. Figure 6-3 is a schematic of the bellows, the container, and the servoactuator; Figs. 6-4 and 6-5 show the feed system assembled and partially disassembled. As shown in Fig. 6-3, a plug is mounted in the rear of the bellows to partially reduce the quantity of lithium remaining in the bellows when it is fully compressed. This was done in order to minimize the rate of accumulation of impurities in the bellows and to minimize the amount of lithium that has to be removed before the bellows can be cleaned.

The base of the plug is connected to a shaft which in turn is connected to a screw-type linear actuator. In the original form of Mark I, this linear actuator exerted the force required to expel the lithium. However, it was later modified so that the force was provided by gas admitted into the space between the bellows and the container. This modification prevented buckling of the bellows by insuring that the outside pressure was higher than the inside pressure. If the bellows were to buckle, mass flow rate could not be measured accurately because the bellows change of volume due to changing pressure differential is nonlinear and nonrepeatable. Figure 6-6 is a photograph of the bellows with internal pressure 15 psi higher than the external pressure, and buckling of the bellows is apparent.

With this gas-actuated system the lead screw then controls the displacement rate of the bellows but does not apply the compressive force. The bellows pressure differential is approximately proportional to the force between the actuator and the bellows. It is measured with a force transducer. The pressure surrounding the bellows is manually controlled so that the actuator force is maintained constant and in slight tension. With the force and the lithium temperature held constant, the flow rate is proportional to the speed of the actuator, which is regulated by the closed loop servosystem shown in Fig. 6-7.

The servosystem consists of a split phase induction motor which drives the lead screw through a speed reducer;

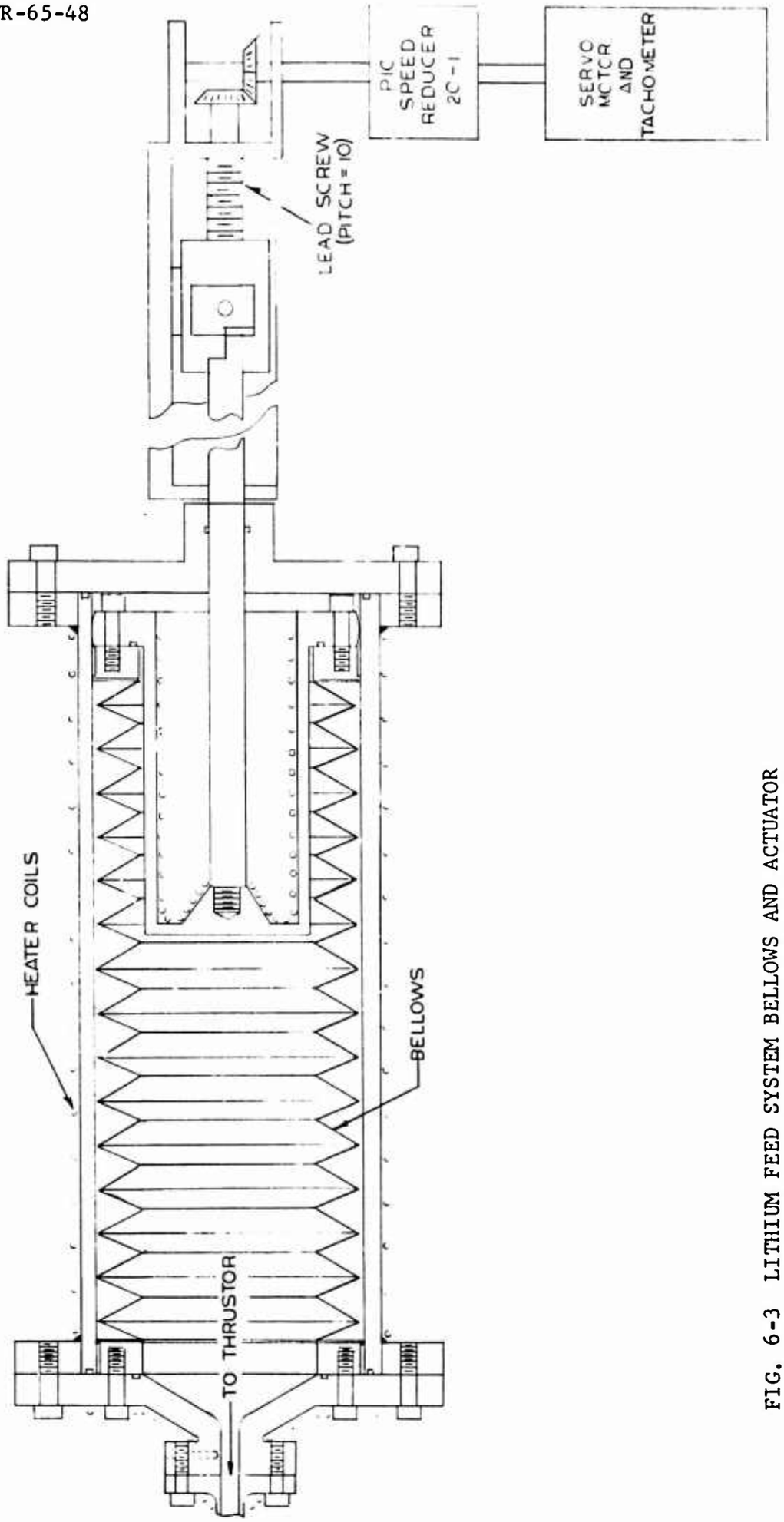

FIG. 6-3 LITHIUM FEED SYSTEM BELLOWS AND ACTUATOR

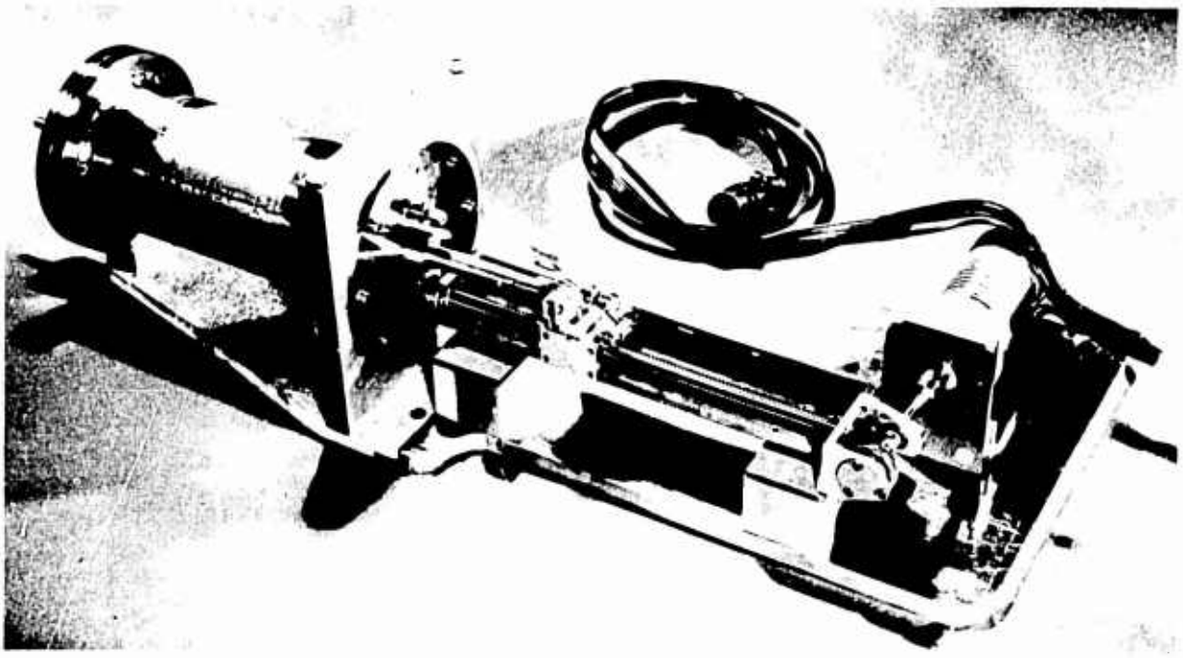

FIG. 6-4 LITHIUM FEED SYSTEM

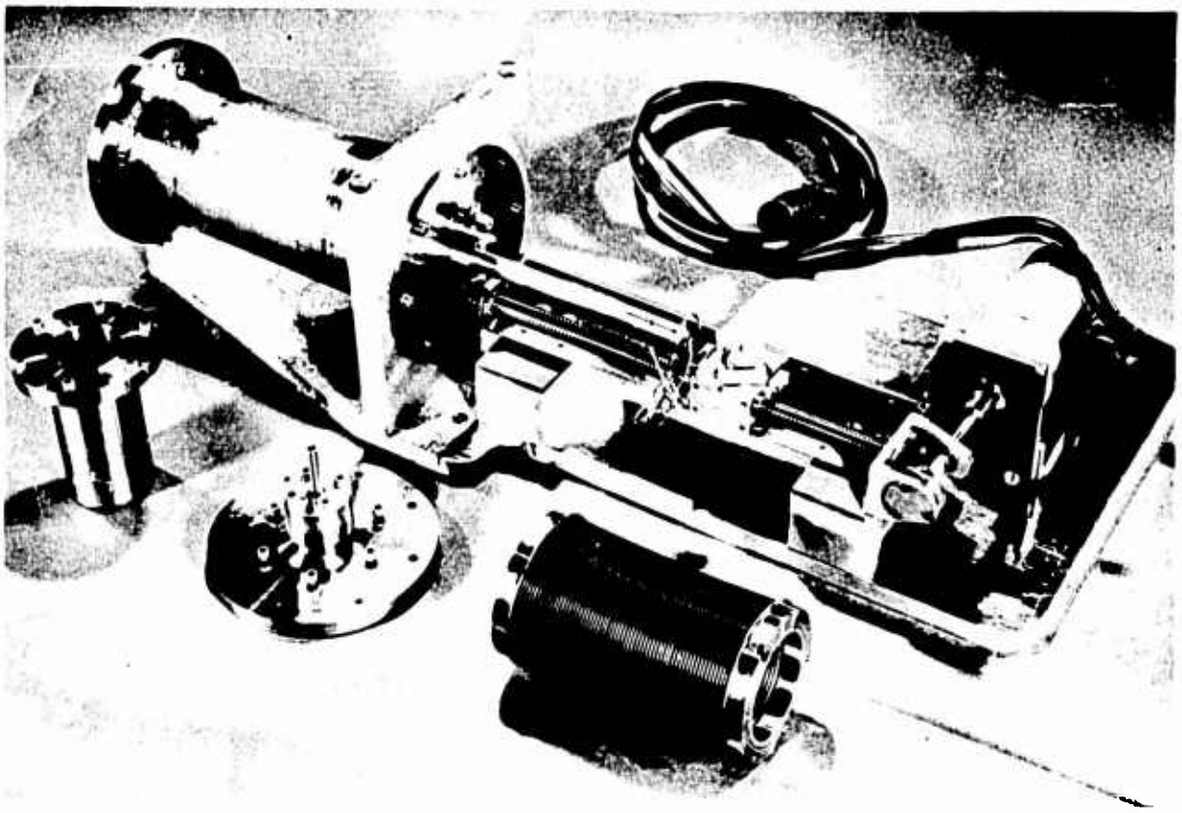

FIG. 6-5 LITHIUM FEED SYSTEM COMPONENTS

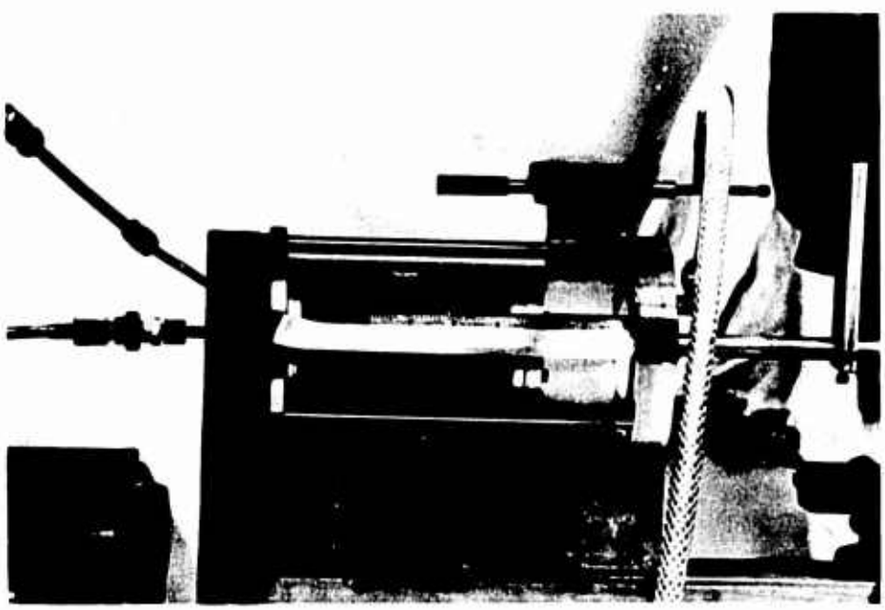

FIG. 6-6 BELLOWS WITH INTERNAL PRESSURE 15 psi HIGHER THAN EXTERNAL

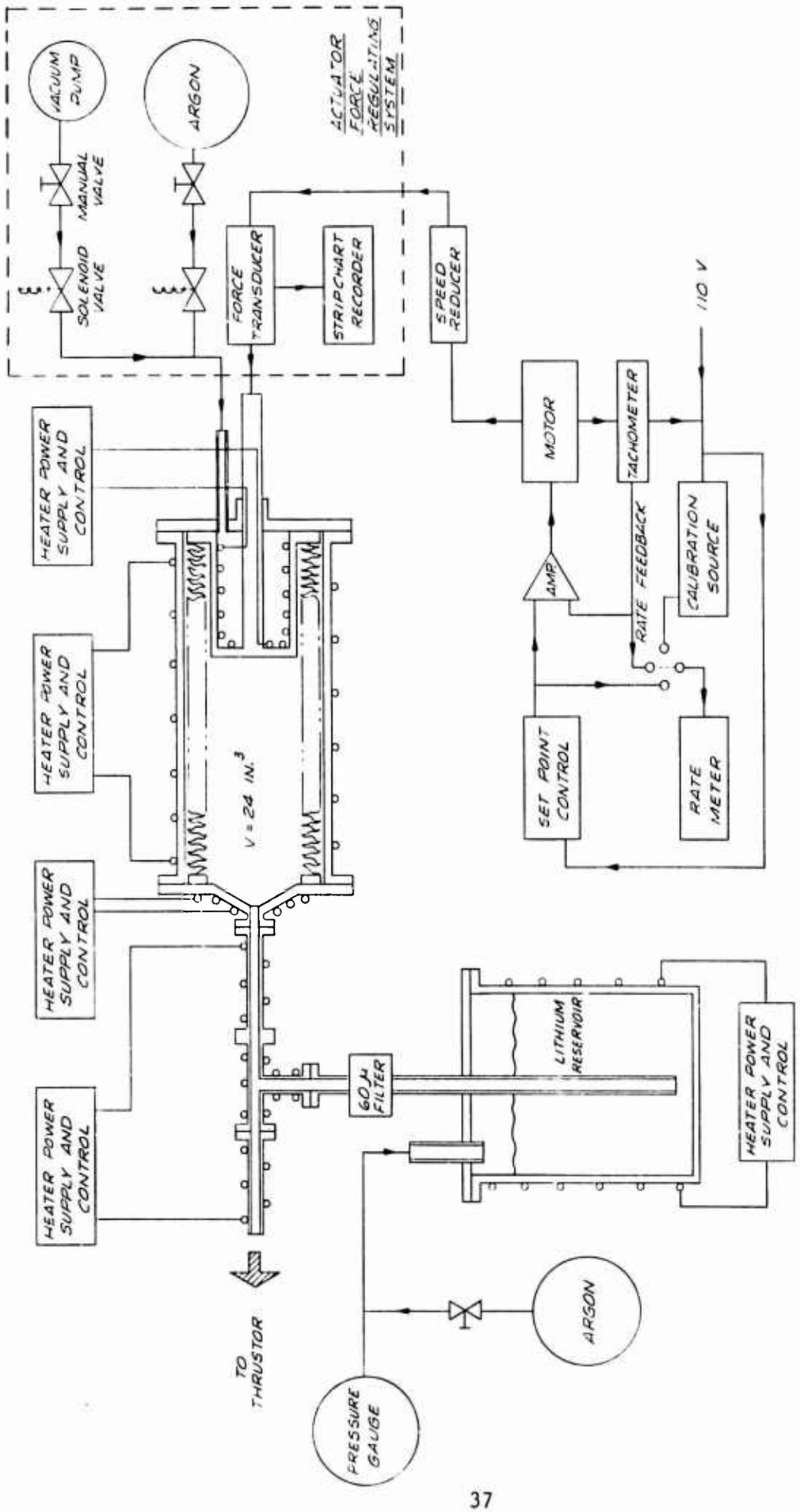

FIG. 6-7 LITHIUM FEED SYSTEM BLOCK DIAGRAM

a tachometer which senses the angular speed of the motor and provides rate feedback to the servoamplifier; a servoamplifier which responds to the tachometer and provides power to the motor to maintain the output of the tachometer equal to the voltage from the set-point control; a set-point device to provide voltage to the amplifier corresponding to the desired mass flow rate; a calibration source for fine adjustment and calibration of the set-point control and feed rate meter; and a feed rate meter to indicate both the mass flow set point and the actual mass flow indicated by the output of the tachometer.

The lithium inside the feeder is maintained at a temperature above its melting point by nichrome wire heating coils cemented to the outside of the cylindrical container, the end flanges of the container, the compensating plug, and the thrustor feed tube. The heater wires for these sections of the feeder are each connected to a separate heater power supply. Each heater power supply has a variable autotransformer (Variac), an isolation transformer, and an ammeter. The isolation transformers are necessary to prevent shorting of the thrustor electrodes to ground in the event that a heater wire shorts to the feed system, which is at an electrode potential. The temperature of each separately heated section of the feed system is measured with a thermocouple and indicated on a meter at the appropriate heater control panel. These temperatures are manually controlled during a run to maintain the feed system temperature between 200^{o} and 225^{o}C.

6.2.2.2 Mark II Feed System

The Mark II feed system shown in Fig. 6-8 uses the same type and size bellows as that used in Mark I, but the lithium is contained between the outside of the bellows and the tubular container. Mark II also has an annular space around the tubular container for containment of tin metal which helps to maintain the lithium at a constant temperature. Since the melting point of tin is slightly higher than the melting point of the lithium, tin can be maintained in

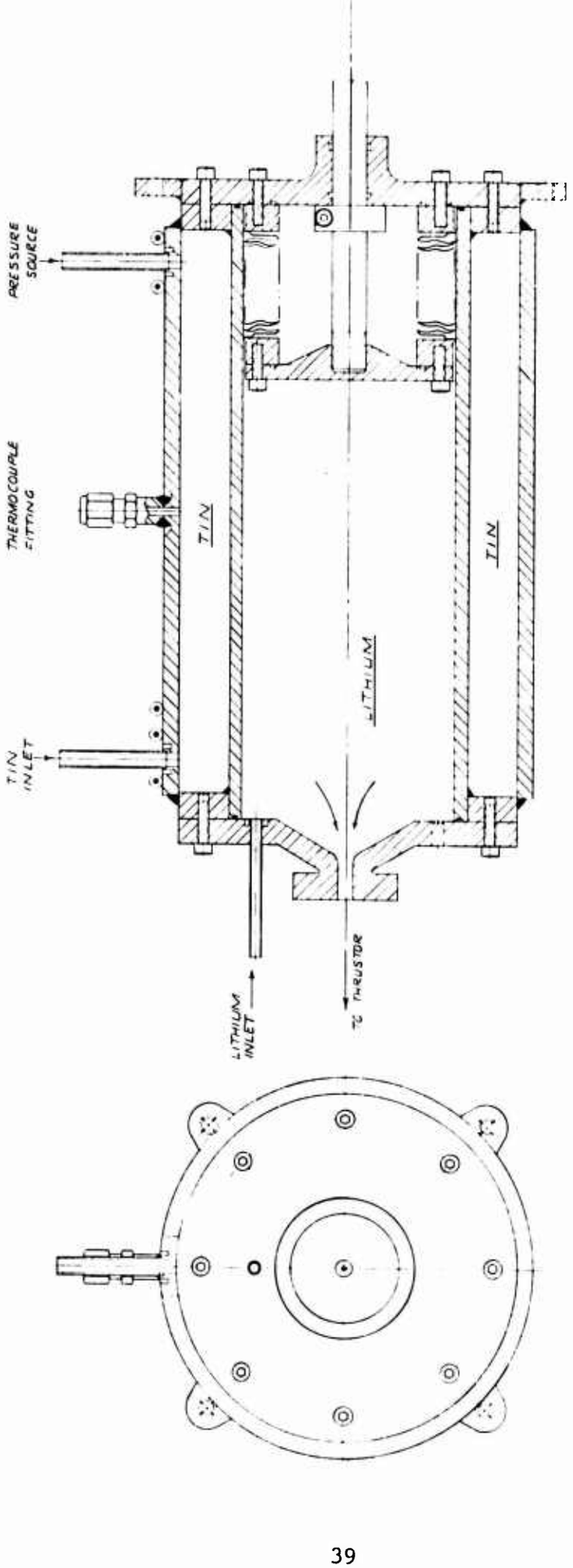

FIG. 6-8 LITHIUM FEED SYSTEM LAYOUT - MK-1 MODIFIED

a two-phase (solid-liquid) state and the latent heat of fusion helps to control the temperature. As in Mark I, the bellows expansion force is provided by gas admitted between the bellows and the container. Mark II also has a speed-regulated drive system and a force transducer for sensing the actuator force.

The scheme of speed regulation for Mark II is somewhat different than that for Mark I. Mark II employs an open loop servosystem consisting of a step-motor controlled by an accurate variable frequency oscillator (Fig. 6-9). At one instant during each cycle of the output of the oscillator, the motor power supply admits a signal to the step-motor, advancing the step-motor shaft through an angle of 90°. Since the motor drives the linear actuator through a 20:1 speed reducer, the lead screw rotates in steps of $4^{\circ}.5$. Although this motor actuates the lead screw in steps, the flow of lithium out of the system should be fairly uniform because of the damping provided by the actuator, force transducer, and the bellows itself. This design is somewhat simpler than that used in Mark I since a tachometer is not required and it will be more precisely regulated through the use of an oscillator which can be frequently calibrated to a crystal frequency standard. It should be possible to obtain an independent measurement of the mass flow rate from determining the period of the slight oscillations in the output of the actuator force transducer which result from the step motion of the drive system.

6.2.3 Feeder Filling Procedure

Both the Mark I and Mark II feed systems are filled with liquid lithium from the transfer container shown in Fig. 6-10. It holds 4 pounds of lithium which is put into the container in solid billets as received from the manufacturer. The lithium in the transfer container is melted using nichrome heater wire and the heater power supplies as described above. Lithium is forced out of the transfer container into the feed systems by gas admitted above the lithium. In flowing out of the transfer container, the lithium passes through a stainless steel 10μ

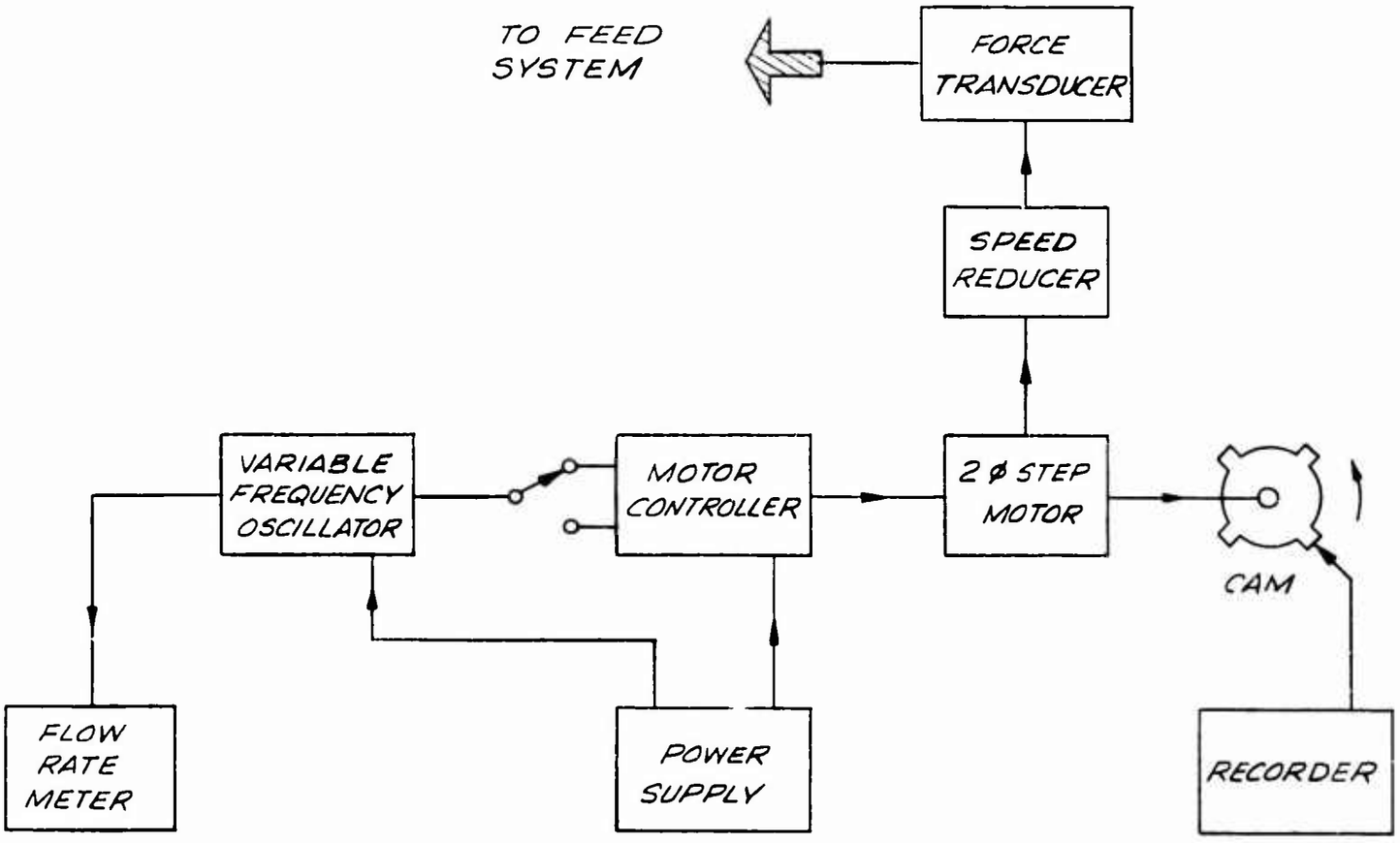

FIG. 6-9 SPEED REGULATION SERVO DIAGRAM - MARK II LITHIUM FEED SYSTEM

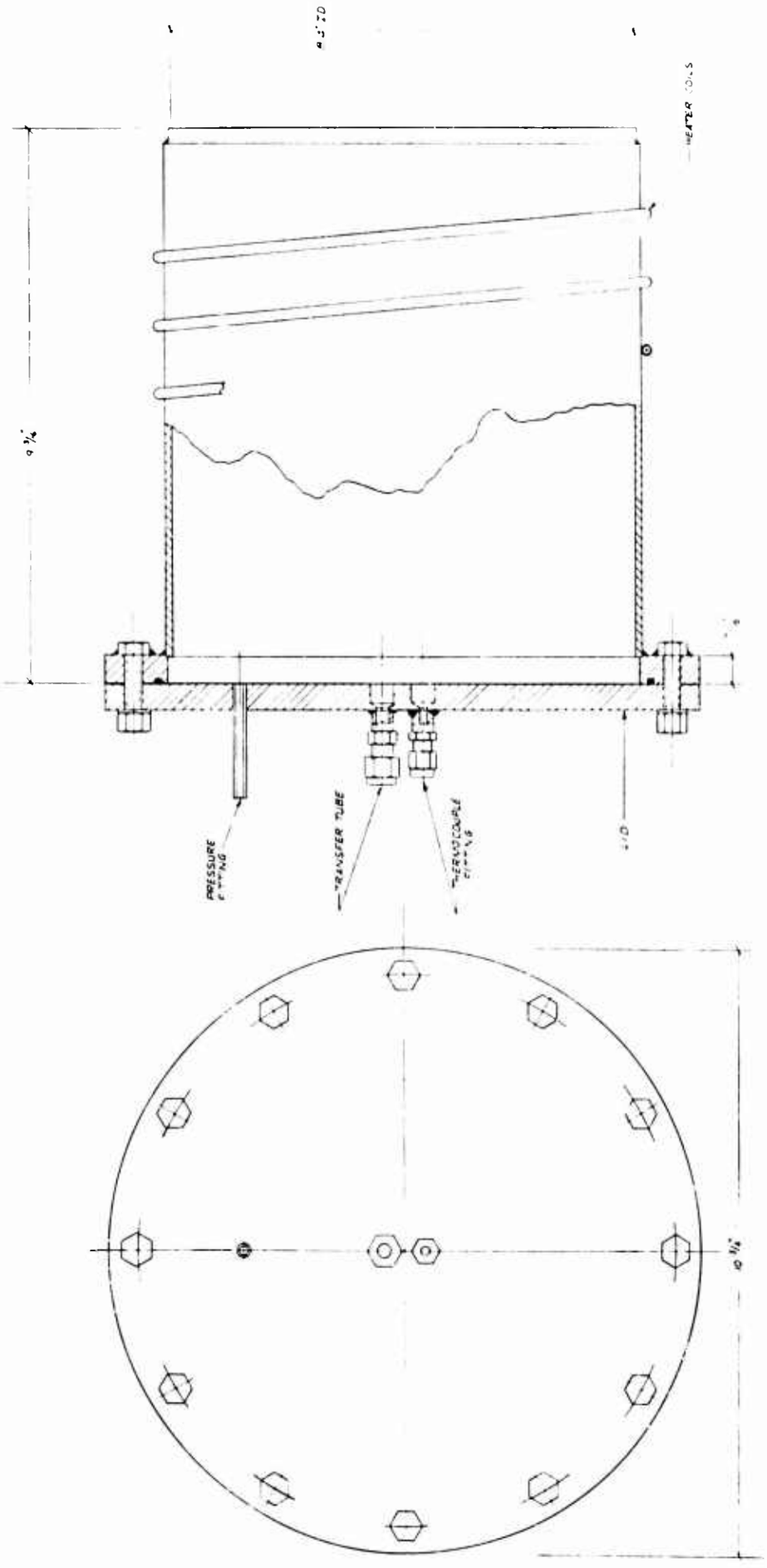

FIG. 6-10 TRANSFER CAN ASSEMBLY, 4LB - LITHIUM FEED SYSTEM

filter for removal of solid-state contaminants. The bellows is filled with the axis of the feed system vertical and with the feed tube at the top so that gas entrained in the lithium will rise to the top of the feed system. After filling, the tube between the feed system and the transfer container is allowed to cool below the melting point of lithium and vacuum is applied to the feed system to remove any entrained gas.

6.2.4 Feed System Calibration

The feed system was calibrated with water to determine the effective area of the bellows. Effective area is the volumetric displacement of the bellows divided by the linear displacement of the end of the bellows. The effective area from the water calibration was later verified by measuring the weight of lithium expelled for known linear displacements of the end of the bellows. Figures 6-11 and 6-12 show the water calibration setup. Water was forced out of the bellows and into the inclined metal tube by the actuator. A small glass tube connected to the metal tube at either end enabled measurement of the height of the water in the tube and thus the volume of water displaced by the bellows. In this calibration the height of the water was measured as a function of the position of the end of the bellows for various pressure levels both above the water and between the bellows and the bellows container.

The actuator force and pressure inside and outside the bellows were also measured during the calibration. Figure 6-13 shows some of the calibration results in terms of volume of water displaced versus deflection of the end of the bellows. These results were obtained for constant values of the actuator force. Constant actuator force would correspond to constant pressure differential if the bellows had no stiffness; however, since the stiffness of the bellows structure is significant, constant actuator force corresponds to a slightly variable pressure differential.

It is to be noted that the slope of the curve of Fig. 6-13 is the same for the three values of actuator force which were used.

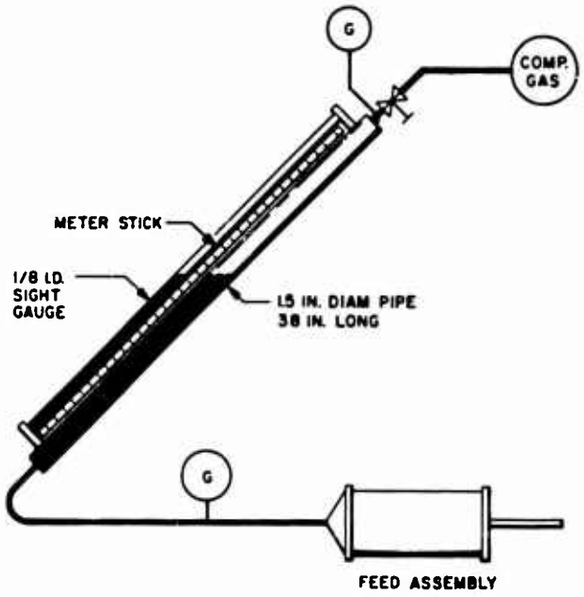

FIG. 6-11

WATER CALIBRATION APPARATUS FOR LITHIUM FEED SYSTEM

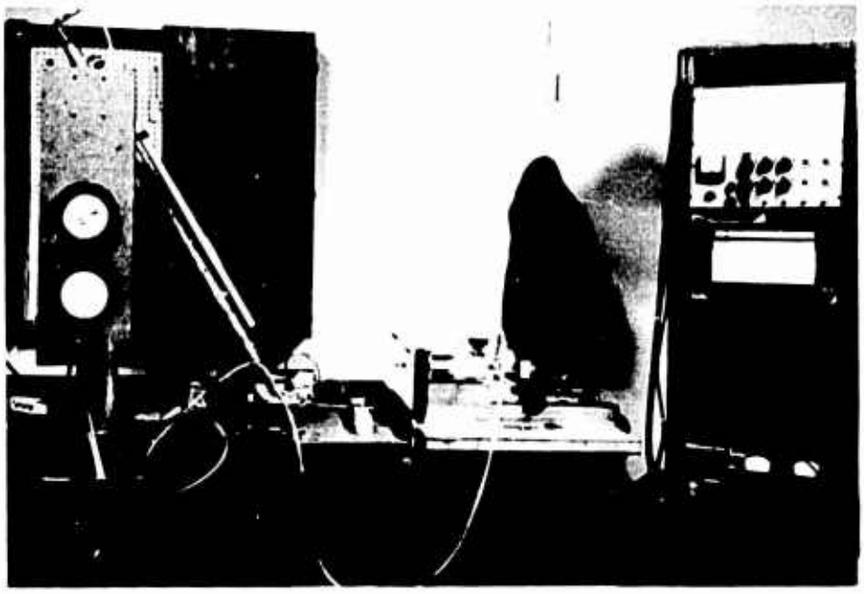

FIG. 6-12

LITHIUM FEED SYSTEM WATER CALIBRATION APPARATUS

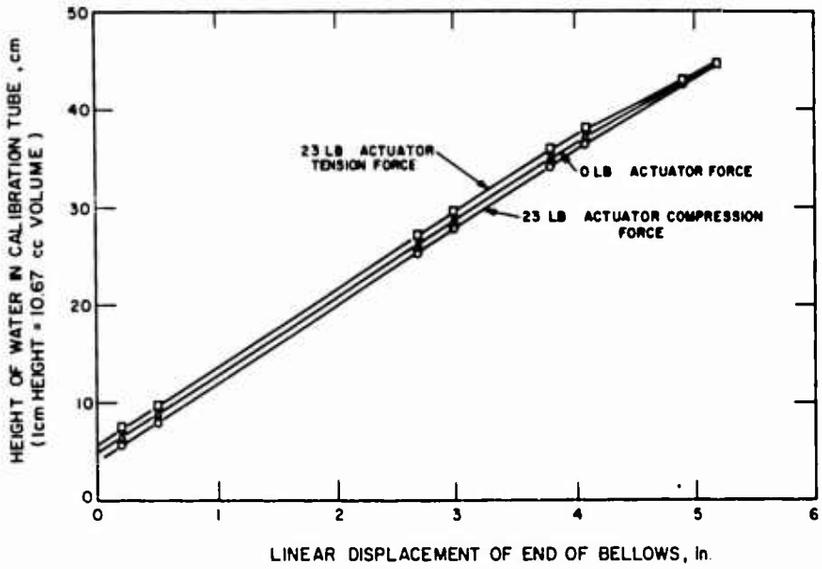

FIG. 6-13

LINEAR DISPLACEMENT OF END OF BELLOWS AS A FUNCTION OF HEIGHT OF WATER IN CALIBRATION TUBE

The figure also indicates that, when the displacement at the end of the bellows exceeds about 4 inches, the effective area decreases. This is caused by nonlinearity in the stiffness of the bellows when it is almost fully compressed.

In the following table the effective area determined from Fig. 6-13 is compared with the effective area determined from the calibration with lithium.

Calibration Medium	Actuator Force	Effective Area (in^2)
Water	+ 23 lb	5.17
Water	0	5.17
Water	- 23 lb	5.17
Lithium	32.5 lb (average)	5.10
Lithium	58.5 lb (average)	5.06

The value for effective area of 5.17 in^2, determined from the water calibrations, was used for calculation of the lithium mass flow rates presented in this report. This value is more accurate than those from the lithium calibration because the actuator force and the temperature were more nearly constant. However, the results from the lithium calibrations confirm, under actual thrustor operating conditions, the effective area established from the water calibrations. It is to be noted on Fig. 6-13 that a change in the actuator force for a given position of the end of the bellows corresponds to a change in volume displaced. This indicates that, if the force is changing during a run, the effective area is different from that determined for constant force. This is the largest source of error in an instantaneous mass flow rate measurement. A changing temperature of the lithium in the bellows causes a corresponding change in the effective area because of the expansion of the lithium in the bellows. Therefore, changing temperature also affects the accuracy of an instantaneous measurement of the mass flow rate. The situation is different, however, for the determination of an average flow over a finite period of time during the run. If, for such a finite period of time, the actuator force and temperature at the end of the

period are the same as at the beginning of the period, the average flow rate over the period is not affected. Also, changing actuator force and changing temperature do not affect mass flow rate from the thrustor as much as mass flow rate out of the bellows. Fluctuations in mass flow rate leaving the bellows are damped partially by the restrictor between the bellows and the thrustor and also by the volume of the lithium passages in the feed-tube and the thrustor.

6.2.5 Feed System Bellows Data

The bellows is a standard stock item, Model No. 52671, manufactured by the Metal Bellows Corporation by welding disks together with an electron beam welder. The bellows material is 347 stainless steel which is not attacked by lithium at temperatures up to 600°C. The pertinent data and dimensions describing the bellows are listed below:

Outside Diameter	3 in.
Inside Diameter	2 in.
Effective Area	4.87 in^2 (specified by manufacturer)
	5.17 in^2 (determined from calibration)
Material Thickness	0.005 in.
Free Length	5.40 in.
Extended Length	7.455 in.
Compressed Length	2.55 in.
Usable Length	5.00 in.
Usable Volume	26 in^3
Spring Constant	4.3 lb/in. (Approx)

6.3 Test Facility Description

During Phase I of this program, a special facility has been fabricated for the purpose of testing lithium arc jets. Prior to completion of this facility, a small, more general purpose vacuum chamber was used. Figures 6-14 and 6-15 show the installation of the thrust balance and an arc jet in the small chamber and the large chamber, respectively.

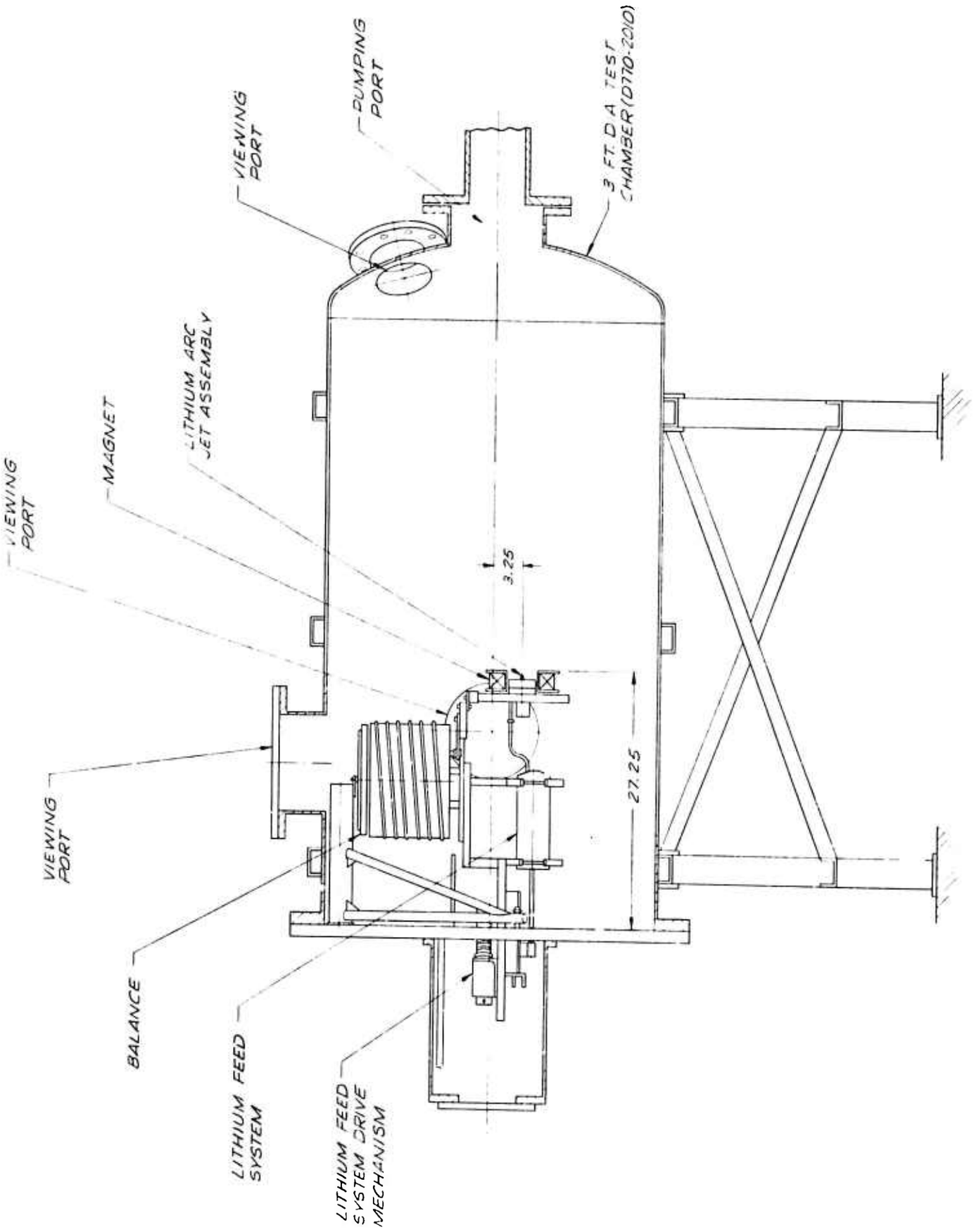

FIG. 6-14 LITHIUM ARC JET 6-FT-DIAMETER TEST CHAMBER

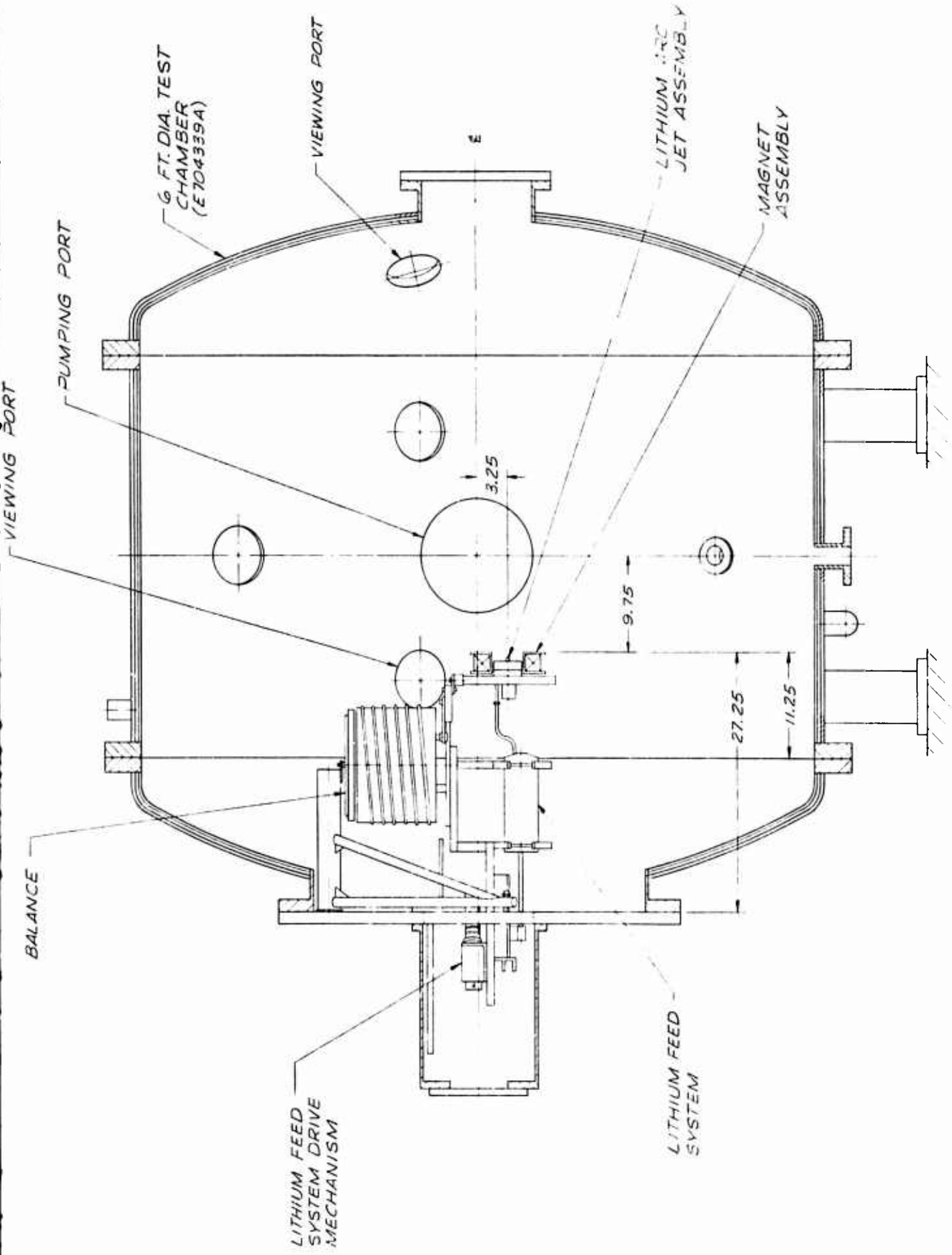

FIG. 6-15 LITHIUM ARC JET 3-FT-DIAMETER TEST CHAMBER

The new special purpose facility was used in the last quarter of the first phase, during which anode-feed engines later than Model LAJ-AF-3 were tested. AF-1, -2 and -3 and all cathode-feed models were tested in a small chamber which is 3 ft in diameter and 6 ft long. This chamber proved to be too small for the lithium arc jet experiments because of the size and complexity of the equipment which has to be installed on the balance. Also, the small chamber is constructed of mild steel, which is subject to corrosion by lithium and its compounds, whereas the large test chamber is constructed of stainless steel.

The new lithium test chamber is 6 ft in diameter and 6 ft long between the extremities of the domed access doors. Important features of this chamber, shown in Figs. 6-16 and 6-17, are as follows:

1. The chamber provides enough space for a long-pendulum balance and a large propellant feed system which is required for long endurance tests (100 hours).
2. The large doors allow full access to the chamber interior so that assembly of the thrustor and feed system can be made with ease, and so that the balance is not disturbed after final adjustments and calibrations are made. (In the small 3-ft x 6-ft chamber, the only access to the inside of the tank was through small viewing ports on the side of the tank.)
3. The test chamber has adequate inside surface area and adequate cooling on the tank walls to effectively condense and thereby cryopump the lithium vapor.
4. The chamber is also connected to a diffusion pump in addition to the large 5,000-cfm 3-stage vacuum pumping system.
5. The chamber is fabricated out of nonmagnetic stainless steel to eliminate the effect of the tank on the applied and induced magnetic fields in the thrustor.
6. Since the tank is constructed out of stainless steel, the walls may be easily cleaned and are resistant to corrosion by lithium and its compounds.

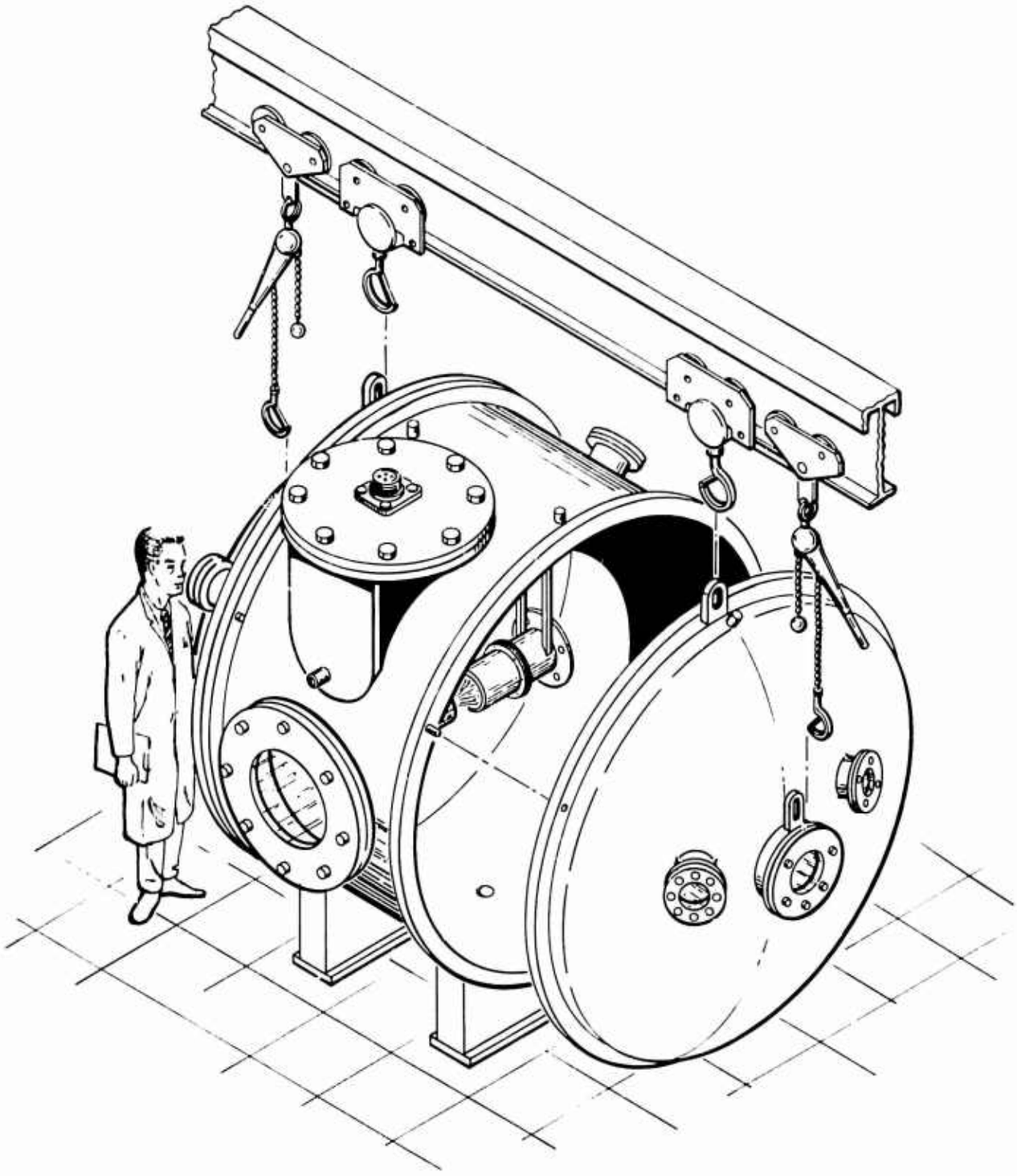

FIG. 6-16 LITHIUM ARC JET TEST FACILITY

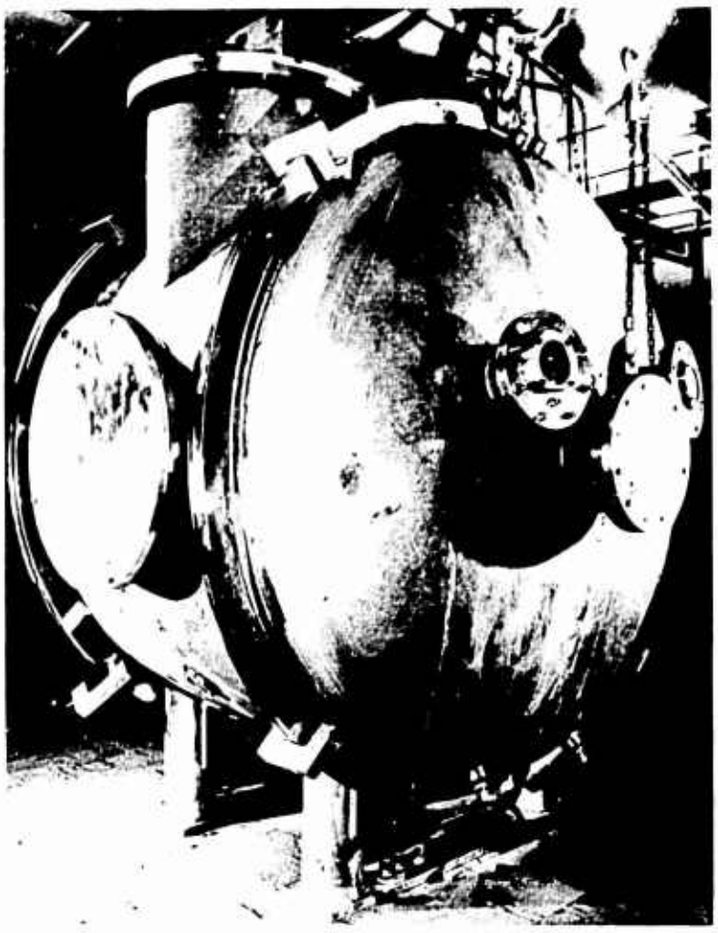

OVER-ALL VIEW OF TANK

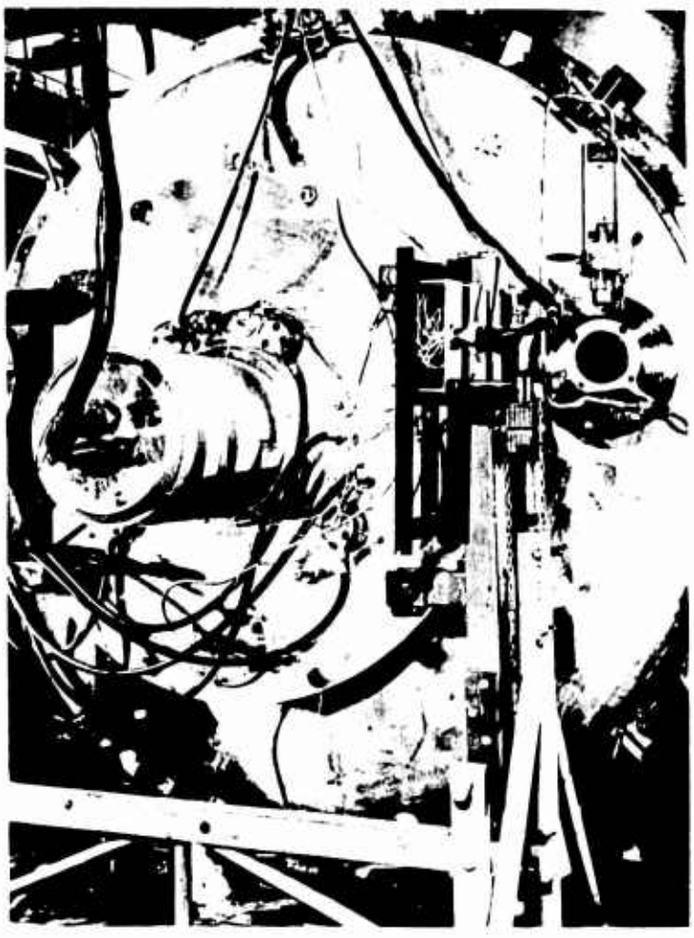

INSIDE VIEW OF TANK SHOWING BALANCE AND THRUSTOR

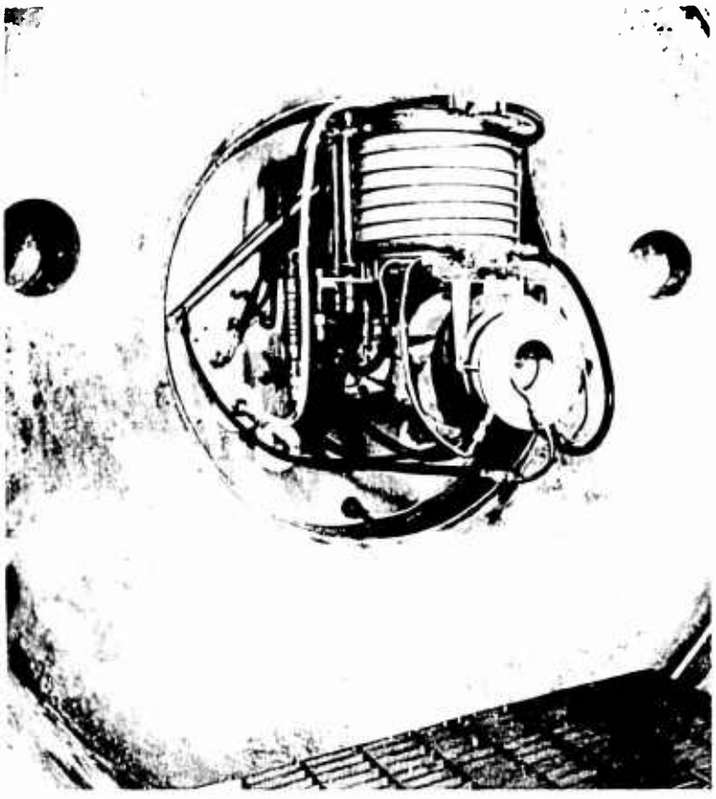

REAR VIEW OF TANK SHOWING POWER, WATER AND INSTRUMENTATION FEEDTHROUGHS

FIG. 6-17

LARGE TEST CHAMBER, 6 FT x 6 FT

7. The arc jet exhaust may be directed diametrically across the chamber as shown in Fig. 6-16 or it may be directed across the tank in an axial direction.
8. A portable A-frame structure and hoists provide for easy removal of the access doors and for rotation of the chamber if desired.
9. Provision has been made for removal of molten lithium from the chamber during long endurance tests.

6.3.1 Facility Pressure Capabilities

With the lithium test facility pumped by the 5,000-cfm pumping system, the minimum pressure capability normally was in the range of 5-10μ Hg (measured by a McCloud vacuum gage and a Hastings thermocouple gage). With a single 12-in. diffusion pump the chamber was pumped down to the 10^{-5}mm Hg range without the engine operating. This pressure was indicated by an ion gage. When a valve between the chamber and the diffusion pump was opened with the engine operating, the pressure dropped rapidly to about 5×10^{-5}mm Hg but remained at this level for only a few minutes or less. Then the pressure increased to greater than 100μ Hg and the valve to the chamber had to be closed. It is possible that this pressure rise was caused by the desorption of gases from the lithium which condensed on the surface of the tank.

7. THRUSTOR DESIGN DETAILS

This section presents the design details for all of the arc jet thrustors which were designed and tested during Phase I of the program. These thrustors consisted of three general types: thrustors with lithium injected at the cathode; thrustors with lithium injected at the anode; and thrustors with lithium injected at the anode and hydrogen injected around the cathode. These will be referred to as anode-feed, cathode-feed, and bipropellant thrustors, respectively. Thrustors with lithium injected at both the anode and cathode were considered, but not tested during Phase I.

The main parts of these thrustors are anode, cathode, cathode-to-anode insulator, main body, and magnet coil. Some of the models also used a heat-radiation disk attached to the anode. The bipropellant engine had, in addition to the above components, a buffer or arc constrictor and a cathode-buffer insulator. With a few exceptions, the materials used for fabrication of the thrustor components were as follows:

Anode	Pressed and sintered tungsten containing 1-2 percent thoria
Cathodes	Pressed, sintered, and swaged tungsten containing 1-2 percent thoria
Insulators	Pressed and sintered boron nitride, commercial grade or low hygroscopic grade
Main body	ATJ graphite or commercial grade boron nitride
Anode radiation disk	ATJ graphite
Magnet coil	Copper
Nuts and bolts used in assembly	Arc-cast molybdenum

7.1 Description of Thrustor Configurations in Chronological Order

Table 7-I lists the thrustors tested in Phase I along with location of the lithium injection, identification of critical materials used, anode diameter, type of cathode, coil internal diameter, and coil position. The listing in the table is in chronological order. Discussions of each model are in the following paragraphs.

Each of the thrustors listed had either the anode or cathode connected to the Mark I lithium feed system described in Section 6.

Model LAJ-CF-1

Figure 7-1 shows the design details of this thrustor which consisted of radiation-cooled tungsten electrodes and a boron nitride insulator between the electrodes. The electrodes were mounted inside a solenoidal magnet coil which has approximately 20 turns of rectangular (0.25 inch x 0.38 inch) tubing. With the maximum current of 2000 amperes through the coil, the axial magnetic field strength at the center of the coil was about 5000 gauss. The lithium was injected through a small hole (0.030 inch diameter) at the center of the cathode.

Thrust and specific impulse of this thrustor were not measured. It was mounted vertically in the test chamber (3 feet in diameter x 6 feet long) facing downward so that any excess liquid lithium would not short the electrodes. This technique was utilized until proper control of the lithium flow was achieved.

Model LAJ-CF-2

This thrustor as shown in Fig. 7-1 was the same as LAJ-CF-1 except the anode internal diameter was increased to 2.0 cm. The larger anode arc voltage (40 to 50 volts) was higher than Model LAJ-CF-1 due to greater interaction with the applied magnetic field. This thrustor, like the first model, was mounted vertically because of lithium feed problems and hence thrust measurements were not made.

Model LAJ-AF-1

Figure 7-2 shows this configuration, the first in which lithium was injected through the anode. In this case, the two-piece anode was

TABLE 7-I

ARC JET THRUSTOR DESIGN DATA

Model Designation	Location of Lithium Injection	Anode Material	Anode Inside Diameter	Cathode Material	Cathode Tip Configuration	Insulator Material	Coil Internal Diameter	Coil and Location
LAJ-CF-1	Cathode Tip	Tungsten	1.5 cm	Tungsten	Blunt	Boron Nitride	3.25 in.	1 in. behind anode face
CF-2	↓	↓	2.0		↓			↓
AF-1	Anode Face	Molybdenum	1.5		Convex Cone			
CF-3	Cathode Tip	Tungsten	3.0		Blunt			
CF-4	↓	↓	↓		↓			
CF-5					Concave Cone			1 in. behind anode face
AF-2	Anode Inner Surface				Convex Cone		3.75 in.	1 in. behind anode face
AF-3A	↓				Concave Cone		↓	↓
AF-4					Hemisphere (Extended)			
AF-3B					Concave Cone			
AF-5A					Convex Cone (Buffered)			1 in. behind anode face
AF-5B					↓			↓
AF-5C								1 in. behind anode face
AF-3C					Concave Cone	Alumina ("Lucalox")		1/8 in. behind cathode tip
AF-3D					↓	↓		1/8 in. fwd. of cathode tip
AF-5D					Convex Cone (Buffered)	Boron Nitride		At plane of lithium injection port
AF-6A					Hemisphere (extended with ridge)			At anode face
AF-6B					↓			1.0 cm forward of anode face
AF-6C					Hemisphere (Extended)			↓
AF-6D					↓			
AF-7					Convex Cone (Buffered)			
AF-8	↓	↓	↓	↓	Hemisphere (Extended)	↓	↓	1.0 cm forward of anode face

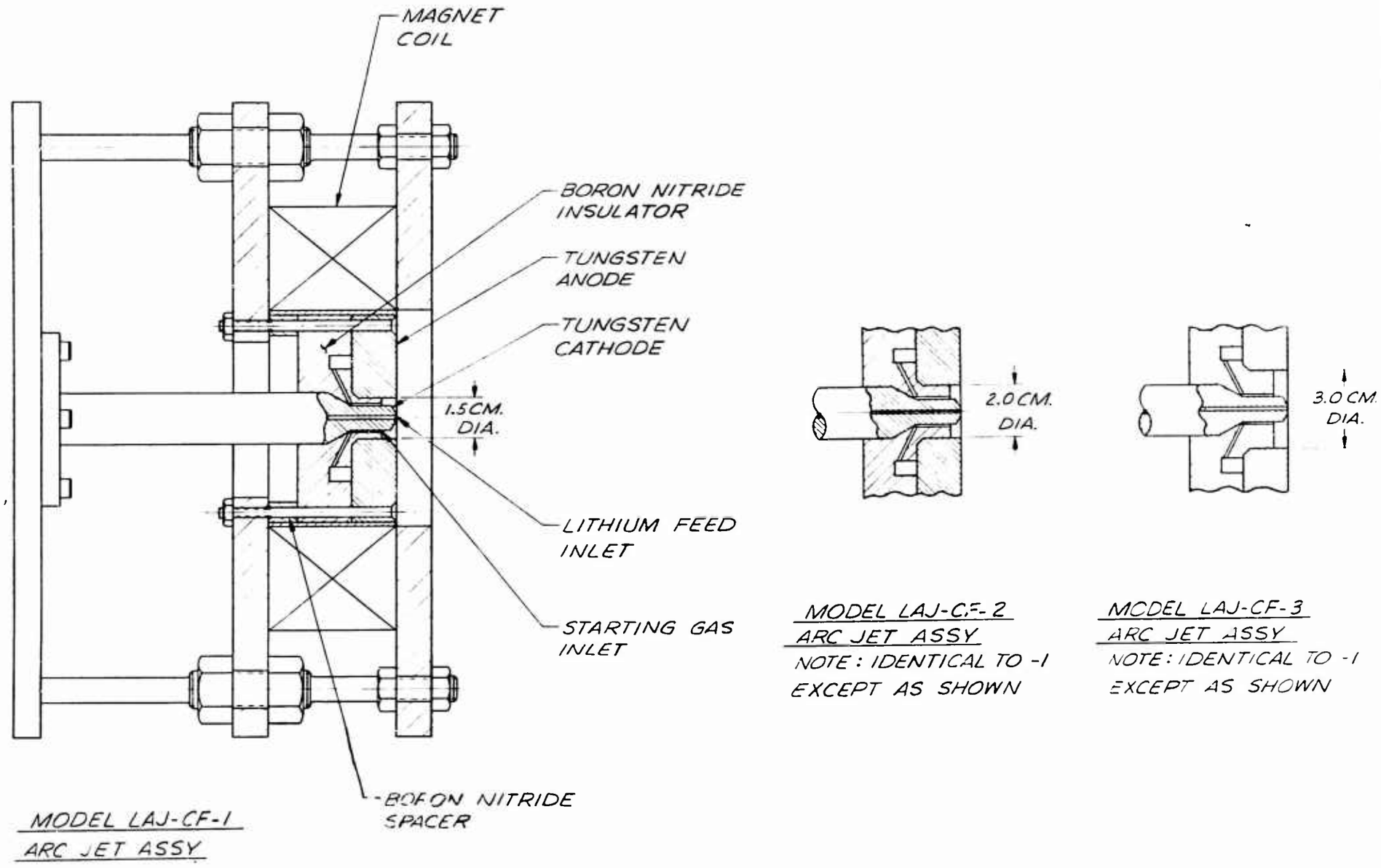

FIG. 7-1 ASSEMBLY DRAWING OF LITHIUM ARC JET MODELS LAJ-CF-1, -2, AND -3

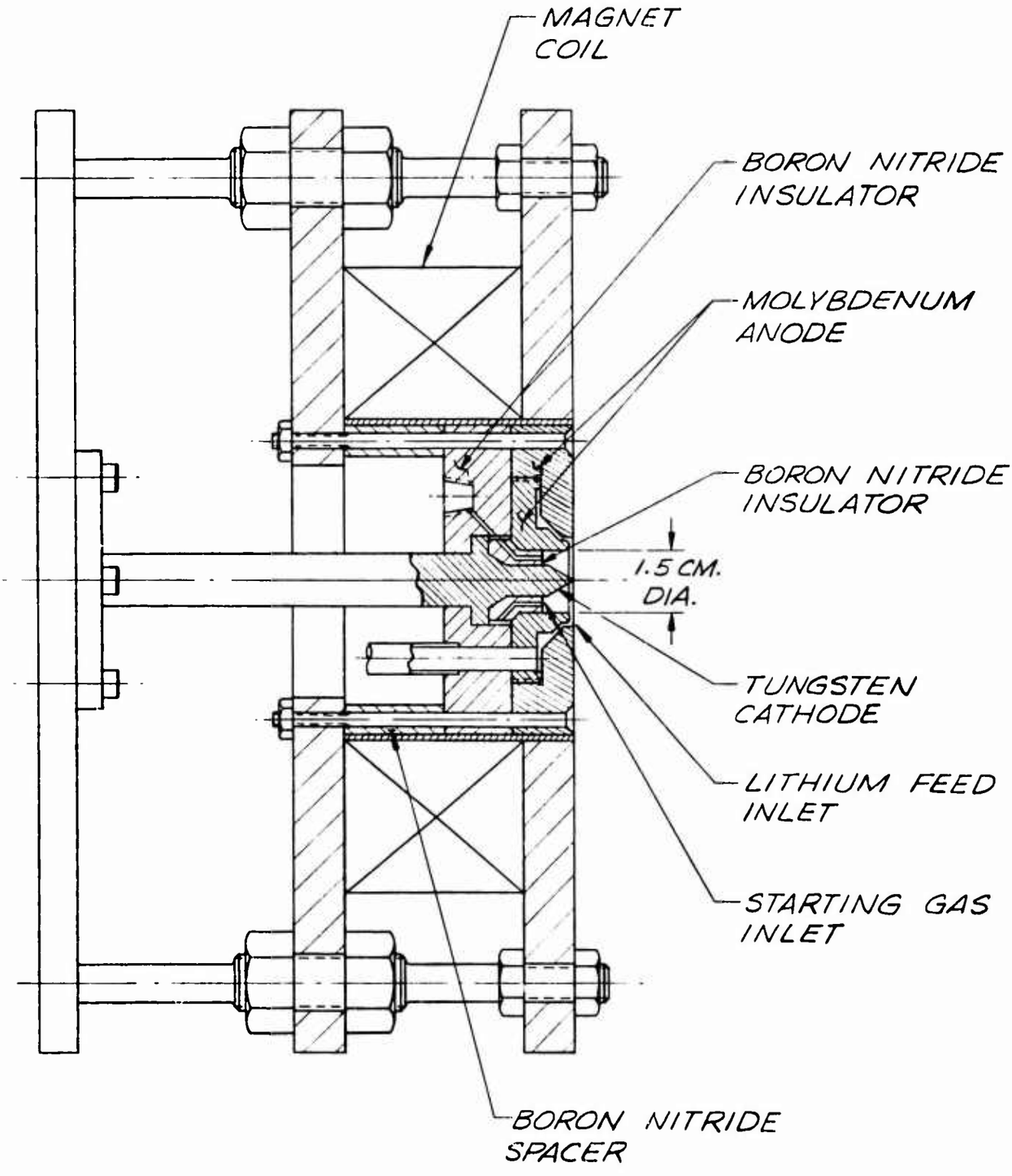

FIG. 7-2 ASSEMBLY DRAWING OF LITHIUM ARC JET MODEL LAJ-AF-1

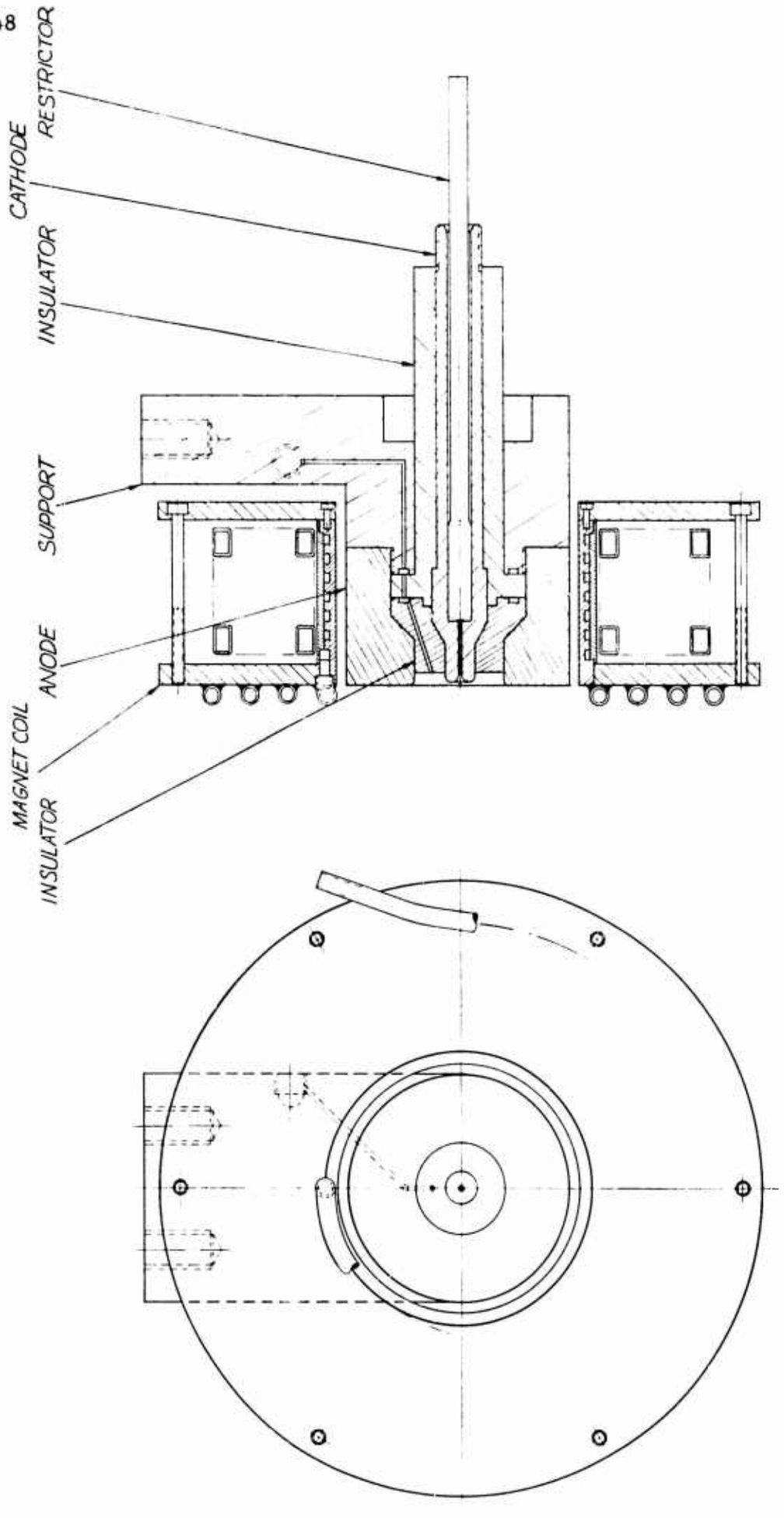

FIG. 7-3 ASSEMBL DRAWING OF LITHIUM ARC JET MODEL LAJ-CF-4

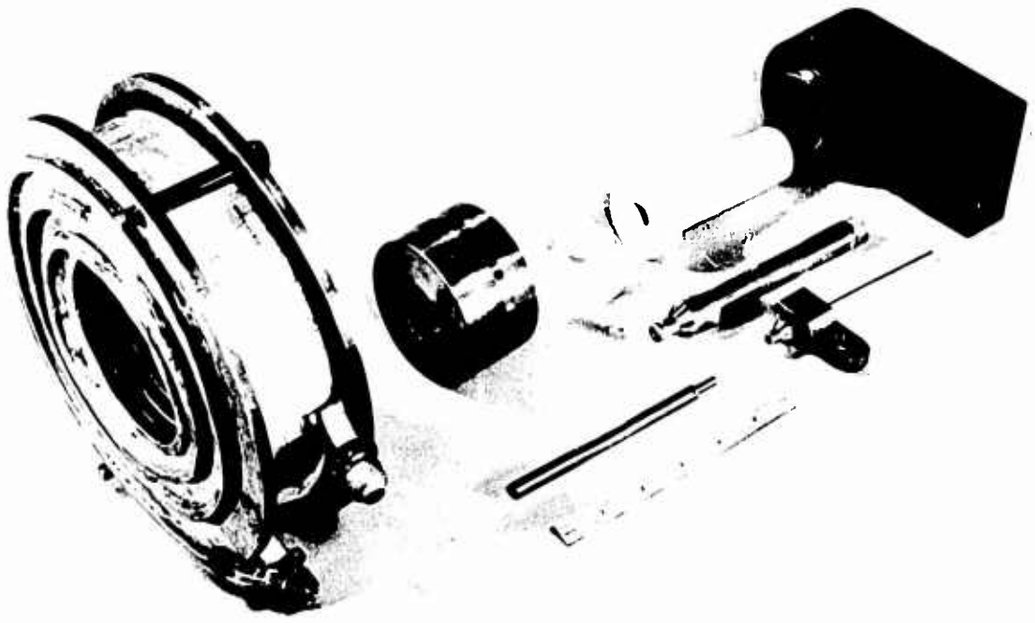

FIG. 7-4 LITHIUM ARC JET MODEL LAJ-CF-4 DISASSEMBLED

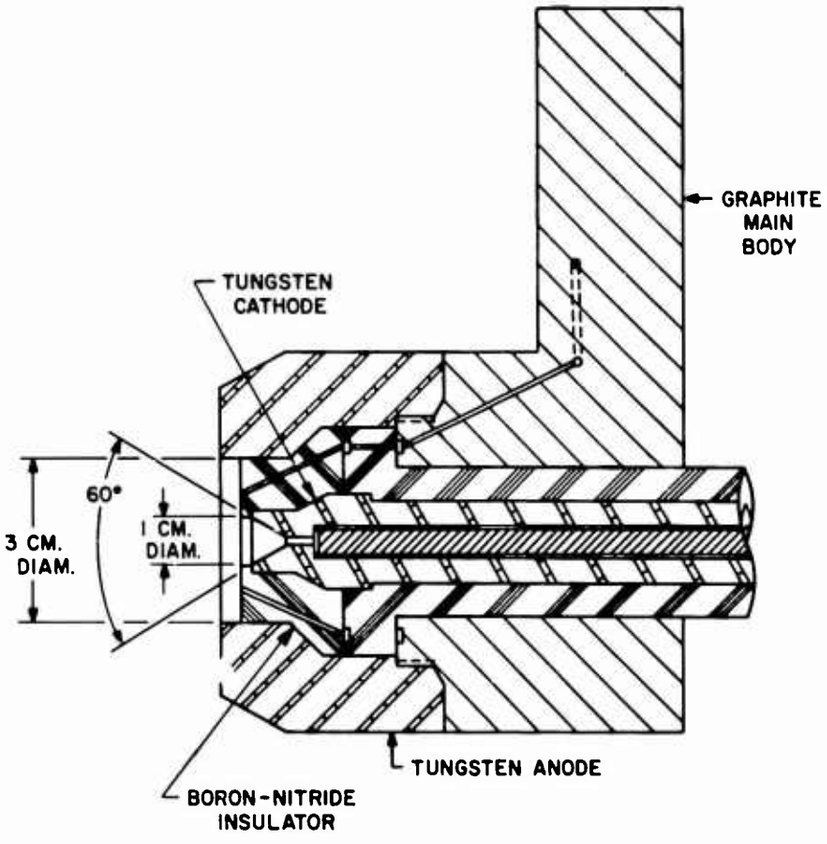

FIG. 7-5

LITHIUM ARC JET MODEL LAJ-CF-5 (magnet coil not shown)

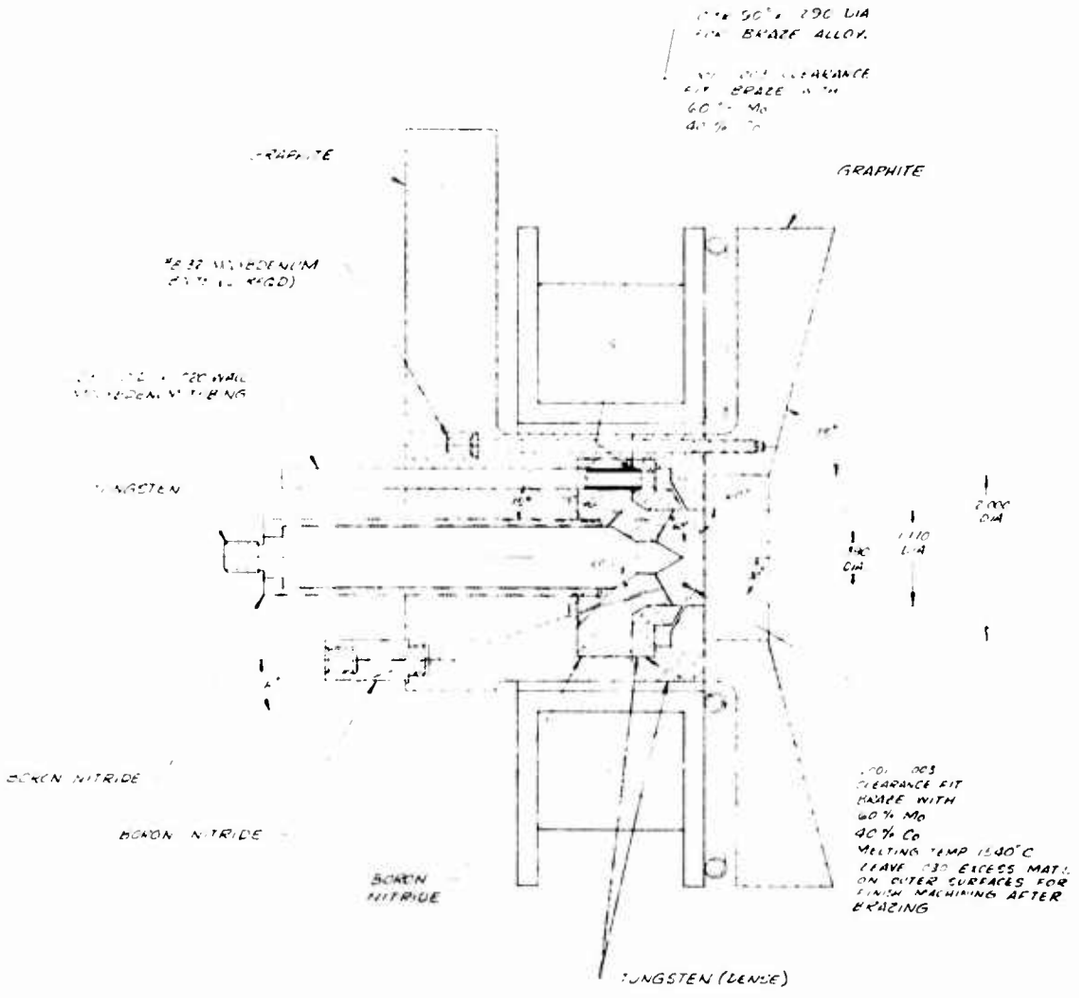

MODEL LAJ-AF-2

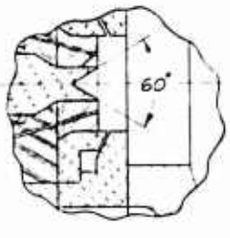

MODEL LAJ-AF-3

NOTE: IDENTICAL TO MODEL LAJ-AF-2 EXCEPT AS INDICATED.

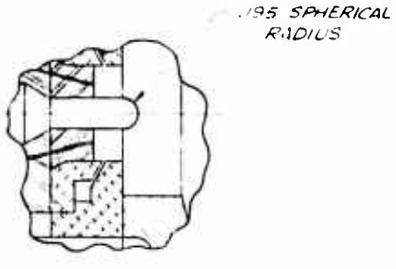

MODEL LAJ-AF-4

NOTE: IDENTICAL TO MODEL LAJ-AF-3 EXCEPT AS INDICATED.

FIG. 7-6 LITHIUM ARC JET MODELS LAJ-AF-2, -3, AND -4

made of molybdenum by electron-beam welding. The cathode was solid tungsten and the insulator was boron nitride. Molybdenum was used for the anode to simplify its fabrication, although tungsten is capable of withstanding higher power levels. The electrodes were placed inside the same magnet coil used with the thrustors described above. In this configuration, the cathode was completely radiation-cooled and the anode was cooled by regeneration, radiation and, to a lesser degree, by conduction to the water-cooled magnet coil.

This thrustor was first mounted in a vertical position. It was later mounted horizontally with the exhaust directed into a target balance; however, the inner piece of the anode melted before thrust was measured.

Model LAJ-CF-3

This thrustor was identical to the first two configurations with cathode feed (Models LAJ-CF-1 and LAJ-CF-2) except the anode diameter was increased to 3 cm as shown in Fig. 7-1.

This thrustor was tested in a horizontal position with a target balance.

Model LAJ-CF-4

Figures 7-3 and 7-4 show this thrustor configuration. It is essentially the same as Model LAJ-CF-3 with lithium injection at the cathode and with an anode diameter of 3 cm.

The anode structure was improved to eliminate fractures caused by thermal shock and thermal stresses. The method of assembly was also improved. As an additional change, the flow-restricting plug in the lithium passage through the cathode was relocated closer to the cathode tip in order to reduce the volume of lithium downstream of the plug.

This thrustor and the feed system were mounted on a direct thrust balance. Figure 6-2 shows the thrustor on the balance before the magnet coil was placed around the thrustor.

Model LAJ-CF-5

The new cathode configuration of Model LAJ-CF-5 was designed to provide a more uniform and stable arc at the cathode surface. As Fig. 7-5 shows, the lithium was injected through the cathode into the apex of a tapered hole at the end of the cathode. The anode was identical to that used in Model LAJ-CF-4 with the exception of the beveled outside edge which was included only to smooth the edge after it had been chipped during the machining process. The other components of this model were also very similar to those of Model LAJ-CF-4 and the same coil was used. The boron nitride cathode-to-anode insulator was modified slightly to make it more compatible with the new cathode design.

Model LAJ-AF-2

Figure 7-6 shows Model LAJ-AF-2, the second thrustor configuration with lithium injected through the anode. In this model the lithium was injected through an annular slot inside the anode whereas in Model LAJ-AF-1 it was injected through a slot on the downstream face of the anode. The lithium in Model LAJ-AF-2 is pumped into the large annular volume behind the injection slot through a 0.250-in.-diam molybdenum tube. Inside this volume, the lithium is normally in the vapor state and thus the flow through the slot into the arc region is uniformly distributed around the circumference. The cathode was a solid tungsten rod which tapers to a point at the downstream end. The anode-to-cathode insulator was boron nitride with four equally spaced holes for injection of argon during startup of the thrustor. A graphite disk was connected to the downstream face of the anode to increase the surface area (and emissivity) for better radiation-cooling of the anode. The anode was clamped between the graphite disk and the graphite main body with six molybdenum bolts as illustrated in Fig. 7-6. The magnet coil used with this model and all subsequent models had the same number of turns as the previous coil, but its inside diameter was increased from 3.25 in. to 3.75 in.

Model LAJ-AF-3

Model LAJ-AF-3 was the same as Model LAJ-AF-2 except for the cathode and anode-to-cathode insulator. The cathode was changed to the inverted-cone configuration shown in Fig. 7-6 in an attempt to make the arc attach to the cathode in a stationary region on the convex conical surface rather than have it move about randomly over a convex surface as in Model AF-2. The insulator was modified slightly to conform to the new cathode shape. The remaining components were identical to those of Model AF-2.

Model LAJ-AF-4

Model LAJ-AF-4 was identical to Model LAJ-AF-3 except in the cathode configuration. The new cathode shape was designed to promote attachment of the arc to the cathode in a region farther away from the anode-to-cathode insulator in order to decrease the temperature and erosion of the insulator. As Fig. 7-6 shows, the cathode was extended so that its hemispherical tip was located 3 cm downstream of the face of the anode. It was thought that the arc would attach either on the hemispherical tip or on the cylindrical surface between the tip and the insulator. The extended cathode had another advantage in that the surface area was increased for larger thermionic emission and radiation cooling.

Model LAJ-AF-5

The bipropellant Model LAJ-AF-5 had a pointed conical cathode tip and a cathode buffer (or arc constrictor) downstream of the cathode (Fig. 7-7). Hydrogen was injected around the cathode through the buffer-to-cathode insulator and then through the buffer. The purpose of the buffer and the hydrogen gas was to maintain the cathode at a pressure high enough to promote attachment of the arc at a small spot on the cathode tip. The cathode and the buffer were cooled with water in this model although it is possible to design such a thrustor which would be cooled by radiation heat transfer. The anode for this model was similar to those used in Models AF-2, -3 and -4. The lithium injection slot was identical and was located at the same distance from the downstream face of the anode. The anode had the same diameter as the previous

models in the region of the lithium injection slot but was changed upstream of the slot to accommodate the buffered cathode. The graphite main body and radiator disk had the same configurations as those used in Models AF-2, -3 and -4. The coil was also the same and was located in the same position relative to the anode downstream face as in these earlier models.

Model LAJ-AF-6

The endurance-tested Model LAJ-AF-6D is shown in Fig. 7-8 along with Models AF-6A, -6B and -6C. These models had electrode configurations similar to Model LAJ-AF-4. The anode designs are essentially identical and the cathodes were all extended various distances beyond the face of the anode. The AF-6 versions have the magnet coil in a forward location (its centerline either at or slightly downstream of the anode face) whereas the AF-4 had the magnet centerline about 3 cm upstream of the anode face. Also, in the AF-6 versions, the graphite radiator disks were upstream of the coil and attached to the rear face of the anode, whereas in AF-4 the disk was downstream of the coil and attached to the front face of the anode.

The cathodes in Models AF-6A and -6B were extended so that their hemispherical tips were 2 cm downstream of the anode face. Both cathodes had the 0.050-in.-high ridge on the cylindrical surface located in the plane of the anode face. The only difference between AF-6A and -6B was the magnet coil location. For AF-6A the coil was centered at the plane of the anode face; for AF-6B it was centered 1.0 cm downstream of the anode face.

Model AF-6C was identical to AF-6B except that the protruding ridge on the cathode was not included.

Model LAJ-AF-6D, the thrustor which was endurance-tested, had a shorter cathode than the previous versions. The tip of the cathode was located 1.0 cm downstream of the anode face. The cathode of AF-6D was water-cooled, as shown in Fig. 7-8, whereas in the previous versions it was cooled primarily by heat radiation. It was water-cooled because the

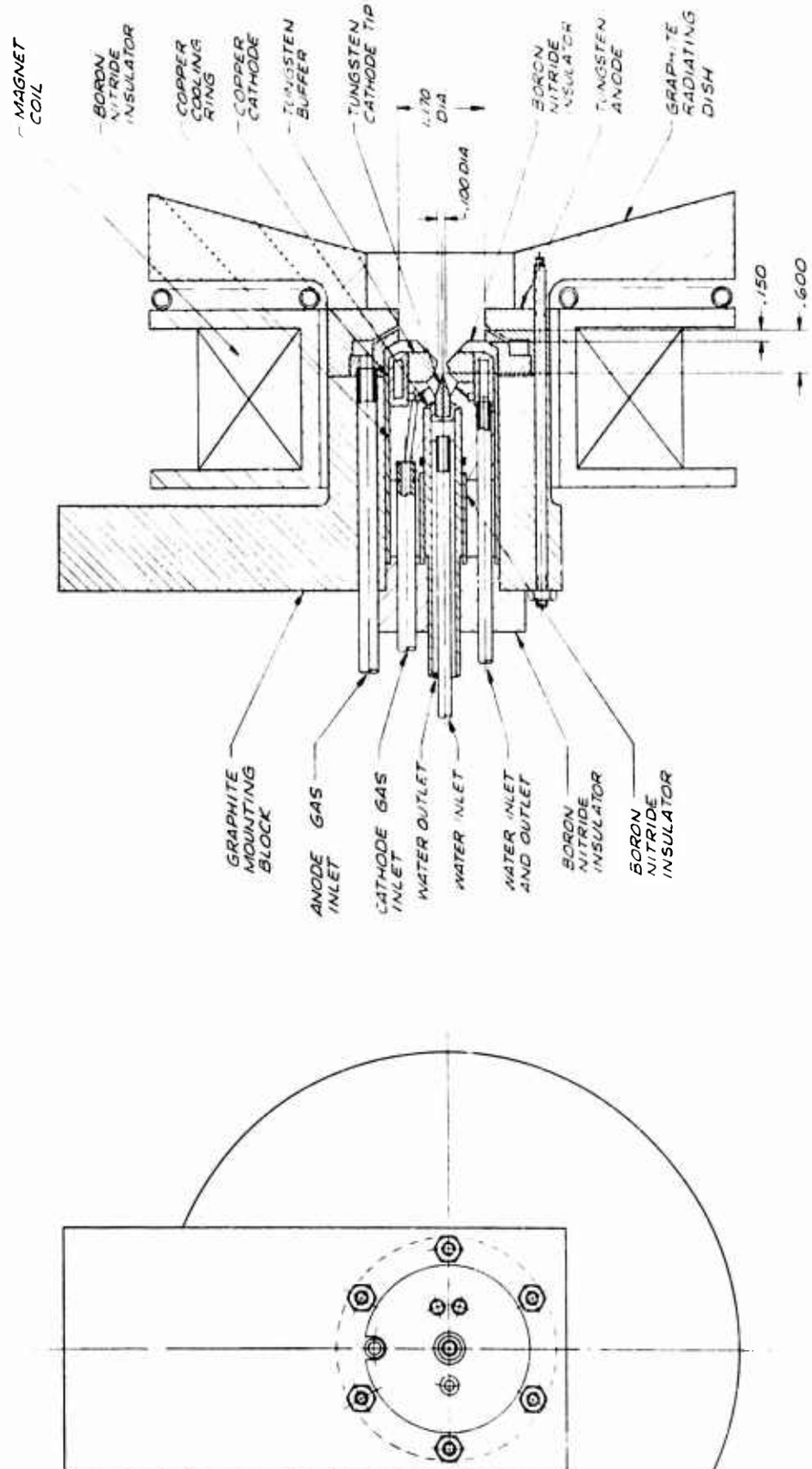

FIG. 7-7 LITHIUM ARC JET MODEL LAJ-AF-5 WITH HYDROGEN-STABILIZED CATHODE

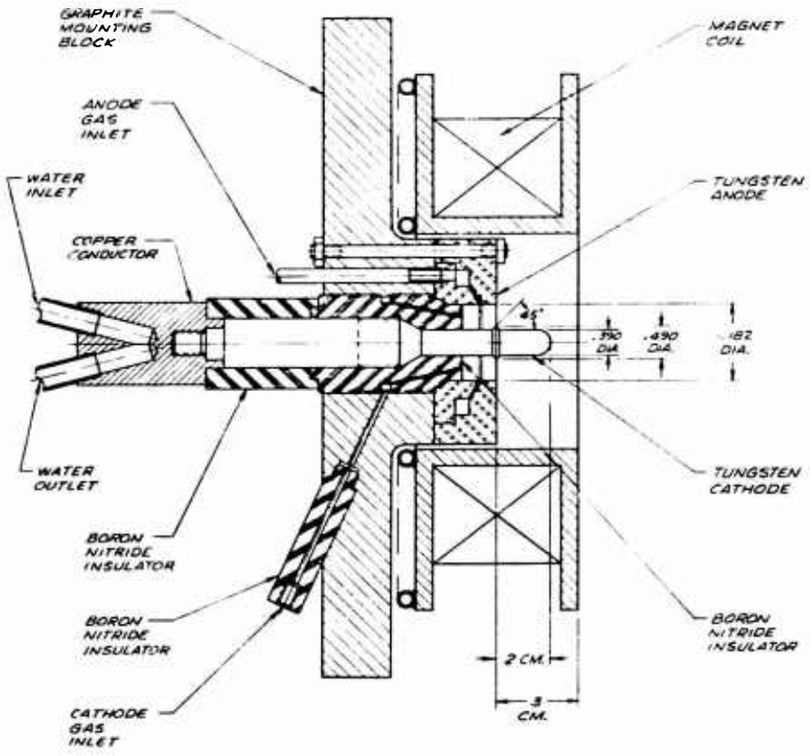

MODEL LAJ-AF-6A

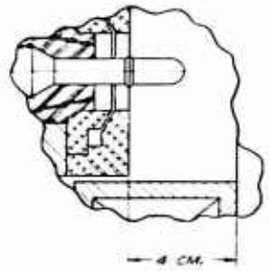

MODEL LAJ-AF-6B
NOTE: IDENTICAL TO MODEL LAJ-AF-6A EXCEPT AS INDICATED.

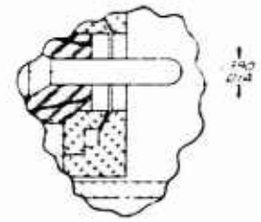

MODEL LAJ-AF-6C
NOTE: IDENTICAL TO MODEL LAJ-AF-6B EXCEPT AS SHOWN.

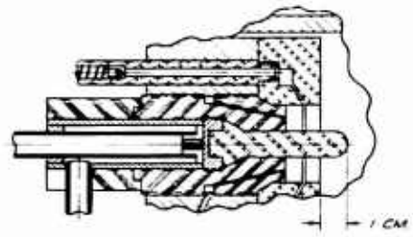

MODEL LAJ-AF-6D
NOTE: IDENTICAL TO MODEL LAJ-AF-6C EXCEPT AS INDICATED.

FIG. 7-8 SCHEMATIC OF LITHIUM ARC JET MODEL LAJ-AF-6

rear portion of the cathode had to be covered with insulation to prevent external arcs. It can be shown by heat transfer calculations that the cathode can be radiation-cooled if a sufficient area is exposed. The cathode can be exposed at sufficiently low ambient pressures - certainly in space. However, in the vacuum test chamber the pressure was not low enough to prevent external arcs. Figure 7-9 consists of photographs of the Model LAJ-AF-6D thrustor which was delivered to the Air Force after the original thrustor of this design had been endurance-tested.

Model LAJ-AF-7

In the Model AF-7 thrustor, lithium was injected at the anode through four holes aligned tangentially to the inside cylindrical surface of the anode. Other than this change to vortex injection from the uniform radial injection previously used, the anode was like those used in Models AF-2 through AF-6. Model AF-7 had the same buffered cathode used with Model AF-5 and the same magnet coil used with Models AF-2 through AF-7. The magnet coil polarity for Model AF-7 was such that the azimuthal JxB force due to radial current and axial magnetic field was in the same direction as the vortex flow from the lithium-injection holes in the anode.

Model LAJ-AF-8

The last new thrustor tested in Phase I of this program was Model LAJ-AF-8, which was like the endurance-tested Model AF-6D except for the length of the anode. The front face of the anode was extended 0.5 inch downstream as shown in Fig. 7-10. The magnet coil was in the same position relative to the cathode as in Model AF-6D.

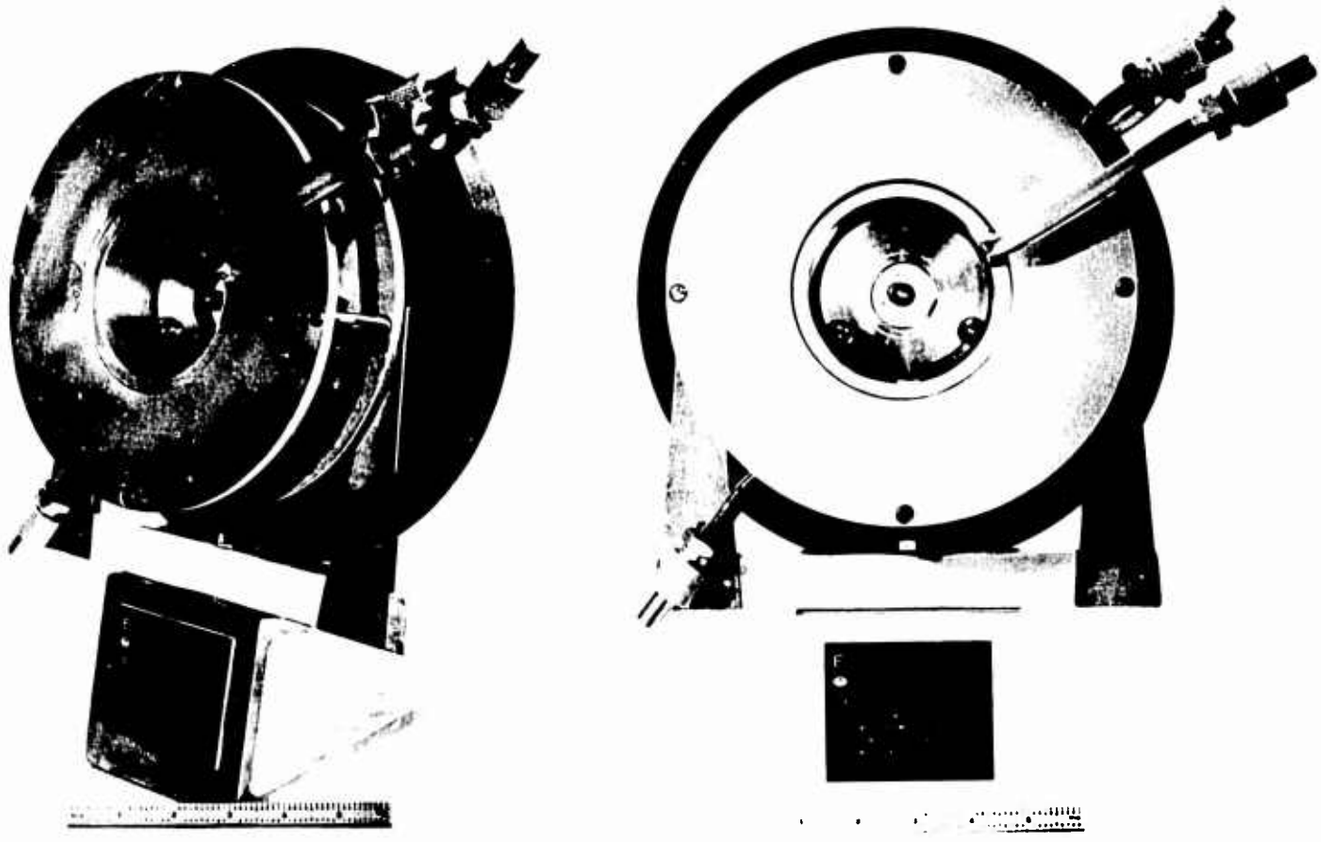

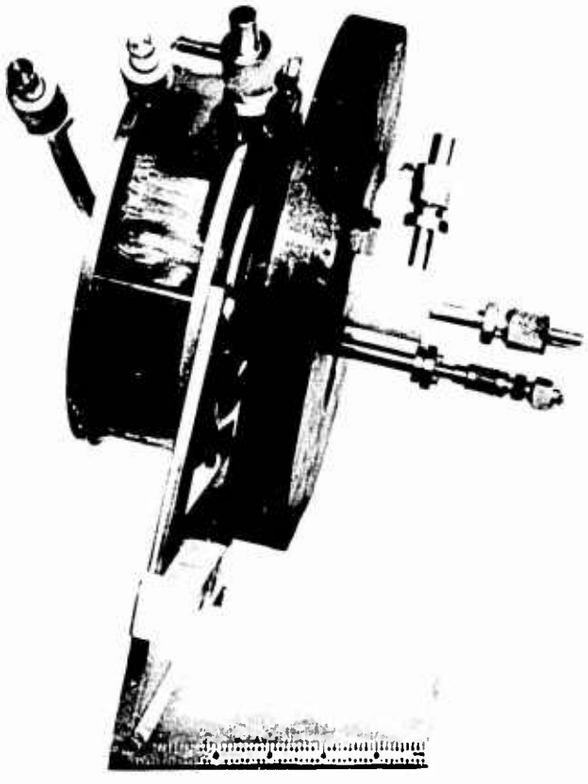

FIG. 7-9

PHOTOGRAPHS OF THRUSTOR DELIVERED TO AIR FORCE

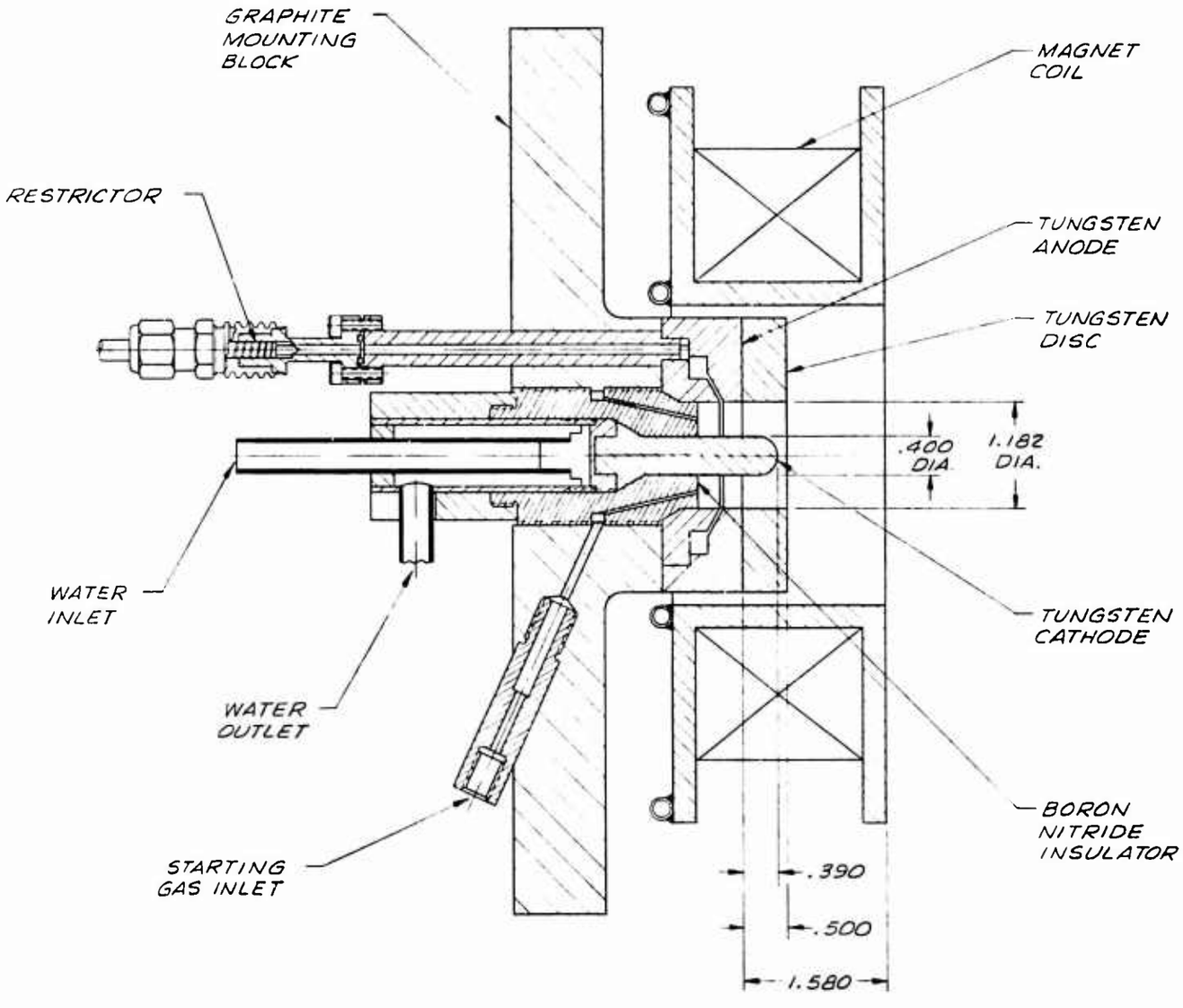

FIG. 7-10 ASSEMBLY DRAWING OF LITHIUM ARC JET MODEL LAJ-AF-8

8. THRUSTOR PERFORMANCE ANALYSIS

There are a number of unresolved problems in connection with the performance of Hall current accelerators that require intensive investigation. Whether or not ambient gas from the vacuum tank is entrained in the exhaust jet is a question that can determine the minimum size and pumping capability of the test facility. The parameters which determine the anode power loss also have a very strong influence upon the performance capability of the engine and must be determined.

In the following analysis, the significance of some very general conservation principles will be emphasized. Some empirical relations will be used to make the analysis tractable. It is not expected that the results obtained here will be applicable to all configurations of Hall current accelerators; however, it is hoped that the assumptions made are adequate for explaining most experimentally observed trends and for predicting the performance capability of most practical engines.

The following are the most important assumptions made, based upon data taken with tests on hydrogen and lithium.

1. The cathode attachment should occur on the tip of a cone which extends so that it is flush with the anode face.
2. The anode attachment occurs on the front face of the anode.
3. The magnetic field strength is maintained in a range where the thrust is independent of the field strength.
4. The thrust is linearly dependent upon the arc current.
5. The power loss to the anode is all due to convection of electron energy with the arc current. The electron energy depends inversely upon the square root of the mass flow rate, but must be high enough to ionize the atoms.

6. The energy of the electrons in the exhaust stream is not recovered.
7. The amount of mass $\dot{m}_e$ which is ionized and accelerated is not necessarily equal to the applied mass flow rate $\dot{m}$. The mass flow which is accelerated is assumed equal to that which is ionized.

From these relations, an energy balance can be constructed:

$$IV = I\, n_o \left(\frac{\dot{m}_o}{\dot{m}} \right)^{1/2} V_I + \frac{K_1^2 I^2}{2 \dot{m}_e} + \frac{|e|}{m_a} V_I \dot{m}_e + \dot{m}_e \left(\frac{\dot{m}_o}{\dot{m}} \right)^{1/2} \frac{|e|}{m_a} n_o V_I \quad . \tag{8-1}$$

The first term on the right represents the energy loss to the anode. The reference mass flow rate can be chosen arbitrarily and the constant n_o determined from experiment. For convenience, the chosen values of $\dot{m}_o$ are

$$\dot{m}_o = \frac{4\pi\, m_a}{\mu_o |e|} \sqrt{\frac{2\, m_a V_I}{|e|}} = 6 \times 10^{-5} \text{ kg/sec (for } H_2\text{)}$$

$$= (9.12 \times 10^{-5} \text{ kg/sec (for Li)} \quad .$$

In this report, it shall be assumed that the best fit for the relation between anode heat loss and mass flow rate is given by

$$P_a = n_o I V_I \left(\frac{\dot{m}_o}{\dot{m}} \right)^{1/2} \quad .$$

However, in many experiments, a relation with a different exponent has been shown to correlate the data better, e.g.,

$$P_a = n_o' I V_I \left(\frac{\dot{m}_o}{\dot{m}} \right)^{1/3}$$

The second term in Eq. 8-1 represents the power in the exhaust beam. For the time being, the mass flow in the beam will be arbitrary and is called the effective mass flow rate, $\dot{m}_e$. The quantity K_1 is the proportionality constant between the thrust and the discharge current. The analysis should determine the value of this constant or else it may be found from experiment.

The third term of Eq. 8-1 represents the power used to dissociate and ionize the mass flowing in the exhuast jet. The fourth term represents the energy of the electrons in the beam.

Equation 8-1 can be conveniently rewritten as

$$\frac{V}{V_I} = \left(\frac{\dot{m}_o}{m}\right)^{1/2} n_o + \frac{K_1^2 \mid e \mid}{2\, m_a\, V_I} \frac{1}{\psi_e} + \left\{1 + \left(\frac{\dot{m}_o}{\dot{m}}\right)^{1/2} n_o\right\} \psi_e \quad , \tag{8-2}$$

where

$$\psi_e = \frac{\mid e \mid}{m_a} \frac{\dot{m}_e}{I} \quad .$$

If the effective mass flow rate $\dot{m}_e$ is equal to the actual mass flow rate $\dot{m}$, and if $\dot{m}$ is held constant when ψ is varied over a wide range by changing the current of the discharge, the voltage would be expected to pass through a minimum as shown by the solid curve in Fig. 8-1. Also included in the figure are some experimental data from Refs. 4 and 14 . For high mass flow rates, i.e., for $\psi > 1$, the theory predicts voltages much higher than measured. In view of this, it has been concluded that $\dot{m}_e$ cannot be equated to the mass flow rate $\dot{m}$. As an alternative, it shall be postulated that the effective mass flow rate $\dot{m}_e$ adjusts itself so as to make the voltage a minimum when $\psi > 1$. This condition equates the last two terms of Eq. 8-2 such that

$$\psi_e^2 = \frac{\mid e \mid K_1^2}{2\, m_a\, V_I \left\{1 + \left(\frac{\dot{m}_o}{\dot{m}}\right)^{1/2} n_o\right\}} \quad . \tag{8-3}$$

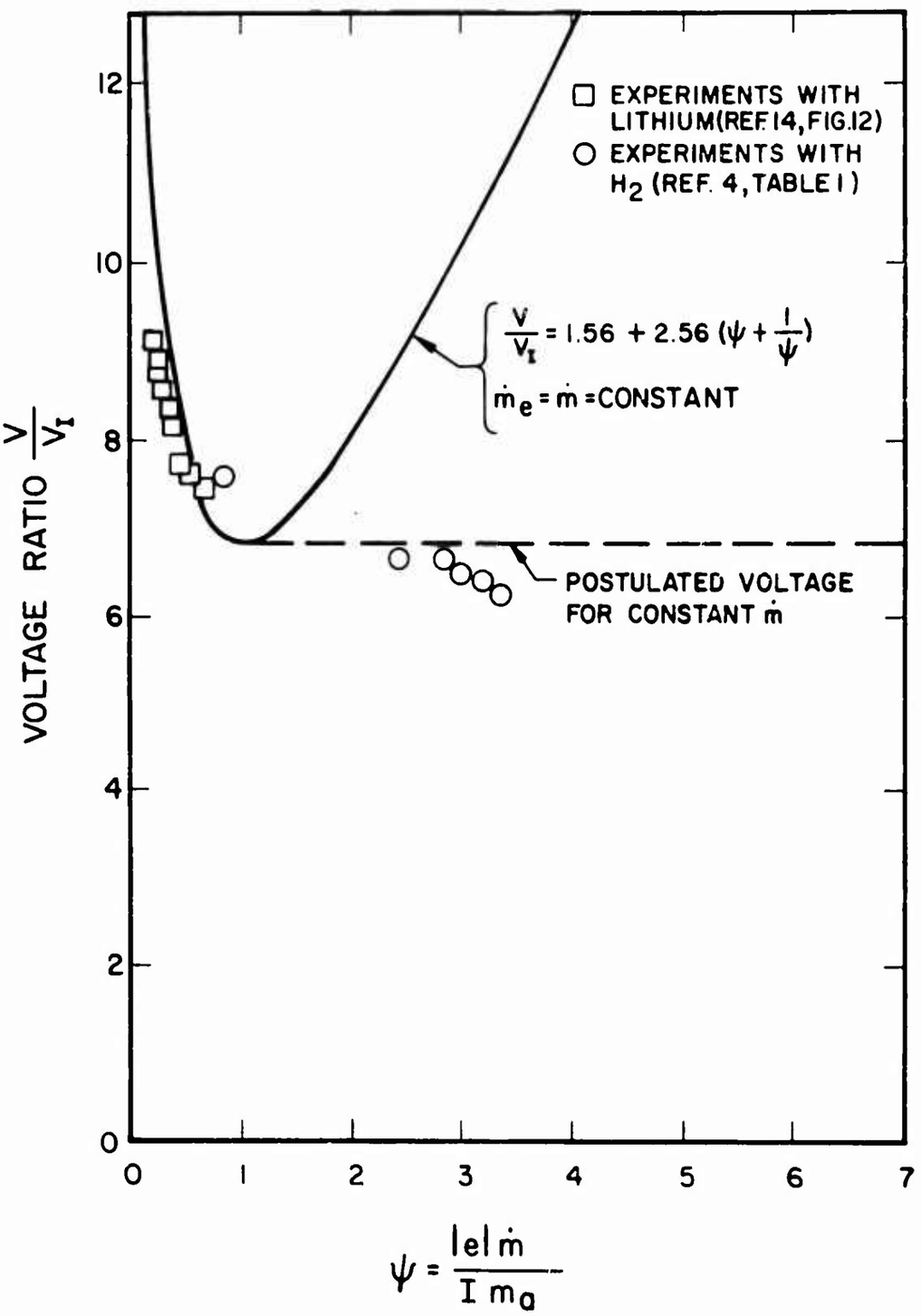

FIG. 8-1 ARC VOLTAGE IN HALL CURRENT ACCELERATORS

It can be further postulated that <u>when $\psi > 1$, the ions carry all of the current and, hence, just enough gas is ionized for this purpose</u>, i.e.,

$$\psi_e = 1$$

and

$$K_1 = \left\{ 1 + \left(\frac{\dot{m}_o}{\dot{m}} \right)^{1/2} n_o \right\}^{1/2} \sqrt{\frac{2 m_a V_I}{e}} \quad . \tag{8-4}$$

Thus, when $\psi > 1$, Eq. 8-2 can be written as

$$\frac{V}{V_I} = n_o \left(\frac{\dot{m}_o}{\dot{m}} \right)^{1/2} + 2 \left\{ 1 + n_o \left(\frac{\dot{m}_o}{\dot{m}} \right)^{1/2} \right\} \tag{8-5}$$

and, when $\psi < 1$, as

$$\frac{V}{V_I} = n_o \left(\frac{\dot{m}_o}{\dot{m}} \right)^{1/2} + \left\{ 1 + n_o \left(\frac{\dot{m}_o}{\dot{m}} \right)^{1/2} \right\} \left\{ \psi + \frac{1}{\psi} \right\} \quad . \tag{8-6}$$

An interesting result of the above postulates is that the energy in the gas is equipartitioned between kinetic energy and internal energy. Because of this, the efficiency is always less than 50 percent for $\psi > 1$. As shown in Fig. 8-1, the voltage is now expected to be constant for $\psi > 1$ and to rise rapidly for smaller values of ψ.

Equation 8-4 expresses a relationship between the slopes of the curves for thrust as a function of current and anode power loss as a function of current. If experimental curves for both these quantities are available, then comparing their values in Eq. 8-4 provides a method of checking the internal consistency of the analysis. Alternatively, if one or the other are available experimentally, then the other can be computed from Eq. 8-4. When the data presented for hydrogen in Ref. 4

were used, the values of K_1 obtained from the curve for thrust as a function of current and from Eq. 8-4 using the measured anode power loss as a function of current correlated to within a few percent.

The manner in which the discharge utilizes the propellant can now be determined. The information is best presented in a plot of effective mass flow rate as a function of the parameter $\psi = |e| \dot{m}/m_a I$ (Fig. 8-2). When $\psi > 1$, the discharge does not use all of the mass provided and hence the mass utilization can be very poor. If the electrode structure is quite open, then it is expected that the engine will operate along the $\dot{m}_e$ curve which gives minimum voltage. If, however, the discharge is forced to flow through the gas in a long constrictor or hollow cylindrical anode, then the mass flow will probably be greater than $\dot{m}_e$ and the voltage will consequently be somewhat higher than the minimum. This will be particularly true if the pressure is higher than 10 to 20 mm Hg.

When $\psi < 1$ then the discharge uses all the mass flow provided and, as ψ is decreased, more would be used in order to keep the potential drop as low as possible. If the device is operated in an atmosphere where the ambient pressure is zero, and if the heat load on the electrodes is low enough so that no electrode material is vaporized or eroded, then the voltage across the discharge must increase as ψ is decreased. However, in the region where $\psi < 1$, the discharge will entrain ambient gas or vaporize electrode material, if possible, in order to keep the potential from increasing. This suggests that a measurement of the discharge potential would be a good criterion to determine whether or not entrainment of ambient gas or vaporization of electrode material is occurring.

The propellant performance in an accelerator can now be estimated on the basis of the above analysis. In particular, expressions for the specific impulse I_{sp} and thrust efficiency η_T can be found. In the region where $\psi = |e| \dot{m}/m_a I > 1$, the equations are summarized below.

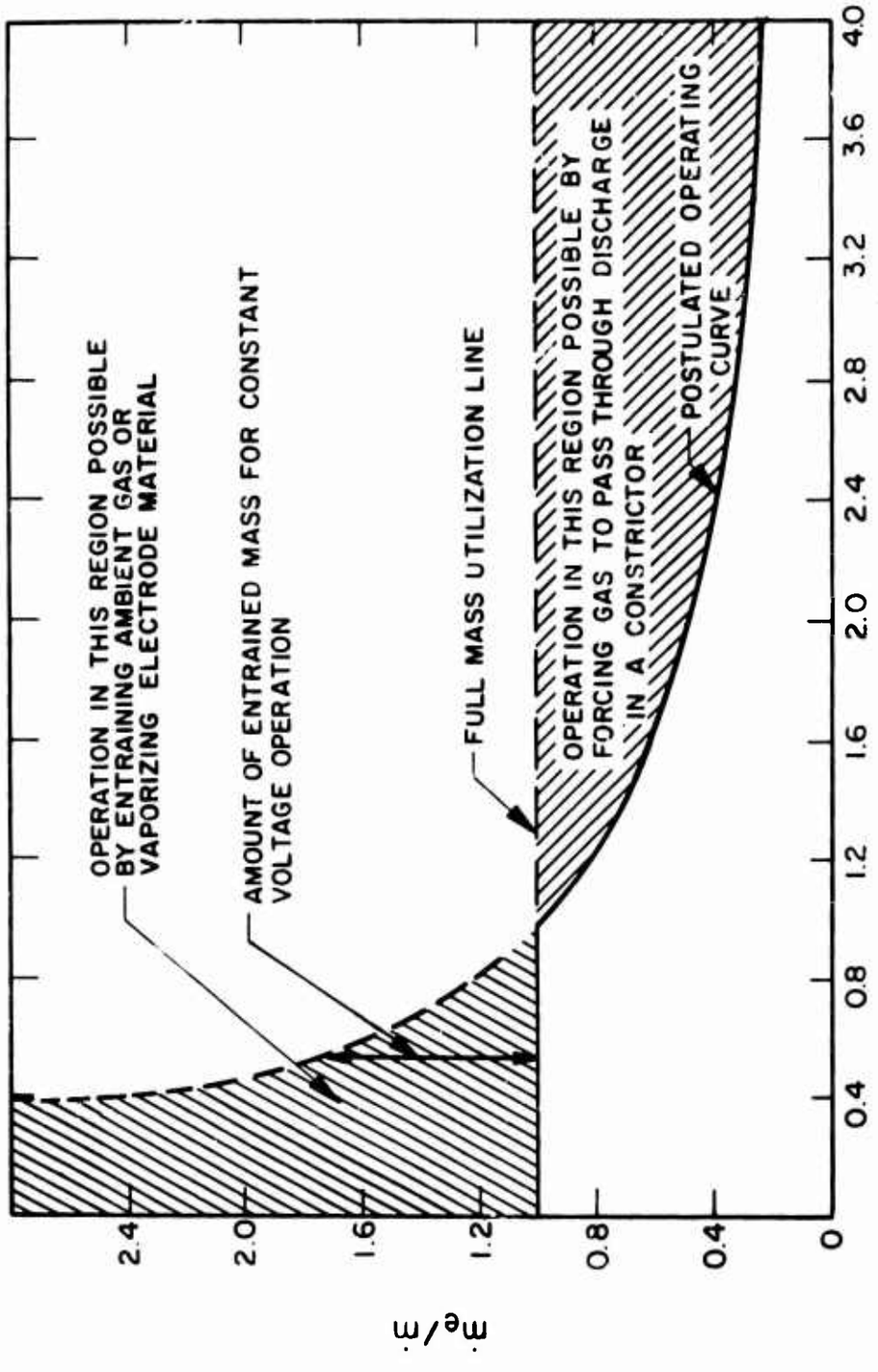

FIG. 8-2 EFFECTIVE MASS-FLOW-RATE

$$\psi = \frac{|e|\dot{m}}{m_a I} > 1$$

$$\dot{m}_e = \frac{m_a I}{|e|}$$

$$\frac{V}{V_I} = 3 n_o \left(\frac{\dot{m}_o}{\dot{m}}\right)^{1/2} + 2$$

$$T = \sqrt{\frac{2\left[n_o \left(\frac{\dot{m}_o}{\dot{m}}\right)^{1/2} + 1\right] m_a V_I}{|e|}}\, I$$

$$\eta_T = \frac{T^2}{2 \dot{m} I V} = \frac{n_o \left(\frac{\dot{m}_o}{\dot{m}}\right)^{1/2} + 1}{3 n_o \left(\frac{\dot{m}_o}{\dot{m}}\right)^{1/2} + 2} \frac{m_a I}{|e|\dot{m}} = \frac{(n+1)\frac{1}{\psi}}{3n+2}$$

$$I_{sp} = \sqrt{\frac{2\left[n_o \left(\frac{\dot{m}_o}{\dot{m}}\right)^{1/2} + 1\right] |e| V_I}{g^2 m_a}} \frac{m_a I}{|e|\dot{m}}$$

$$= I^o_{sp} \sqrt{\frac{n+1}{\psi}} \quad ,$$

where

$$\dot{m}_o \equiv \frac{4\pi m_a}{\mu_o |e|} \sqrt{\frac{2 m_a V_I}{|e|}} = 0.06 \text{ g/sec (for } H_2\text{)}$$

$$= 0.092 \text{ g/sec (for Li)}$$

$$I^o_{sp} \equiv \frac{1}{g} \sqrt{\frac{2|e|V_I}{m_a}} = 5600 \text{ sec (for } H_2\text{)}$$

$$= 1240 \text{ sec (for Li)}$$

In the region where $\psi < 1$, the following equations summarize the engine performance capability:

$$\frac{|e|\dot{m}}{m_a I} \equiv \psi < 1$$

$$\dot{m}_e = \dot{m}$$

$$\frac{\dot{V}}{V_I} = n + (n+1)\left(\frac{1}{\psi} + \psi\right)$$

$$T = \sqrt{\frac{2(n+1) m_a V_I}{|e|}}\, I$$

$$\eta_T = \frac{(n+1)\frac{1}{\psi}}{n + (n+1)\left[\frac{1}{\psi} + \psi\right]}$$

$$I_{sp} = \sqrt{\frac{2(n+1)|e|V_I}{g^2 m_a}}\,\frac{1}{\psi}$$

$$= I_{sp}^{o}\,\frac{\sqrt{n+1}}{\psi}$$

$$n = n_o \left(\frac{\dot{m}_o}{\dot{m}}\right)^{1/2}$$

From the above equations it is possible to plot a curve of the best efficiency possible for each specific impulse. This efficiency occurs when the power in the discharge is very high, since the high mass flow rate under these conditions makes the percentage loss of power to the anode quite low.

Use of the parameter I_{sp}^{o}, as defined above, yields a universal curve that is valid for all propellants. This universal plot of the thrust efficiency η_T as a function of the reduced specific impulse is presented in Fig. 8-3.

It is important to know the effect upon the efficiency of working at power levels of practical interest. This is shown in Fig. 8-4 where the efficiency as a function of the reduced power is plotted. Values of the reduced power are obtained by use of a parameter P_o defined by

$$P_o = \frac{|e| V_I n_o^2 \dot{m}_o}{m_a} \quad .$$

These curves are valid for all propellants provided they are only singly ionized and comprise only one element.

On the basis of the above analysis, plots can also be made of the potential drop across the discharge as a function of the specific impulse. Such a plot is shown in Fig. 8-5 for an assumed value of the electron energy of $1.4V_I$ electron volts.

Conclusions

1. When operating at high mass flow rates ($|e|\dot{m} > m_a I$), the effective mass flow tends to be less than that supplied. This applies to open devices which do not force the mass through the discharge. In this region voltage is substantially independent of the arc current.
2. When operating at low mass flow rates ($|e|\dot{m} < m_a I$), the voltage increases with increasing current or there is entrainment to make the effective mass flow greater than that supplied.
3. It is impossible to obtain a thrust efficiency greater than 50 percent if the specific impulse is less than I_{sp}^{o} (I_{sp}^{o} depends only upon properties of the propellant).

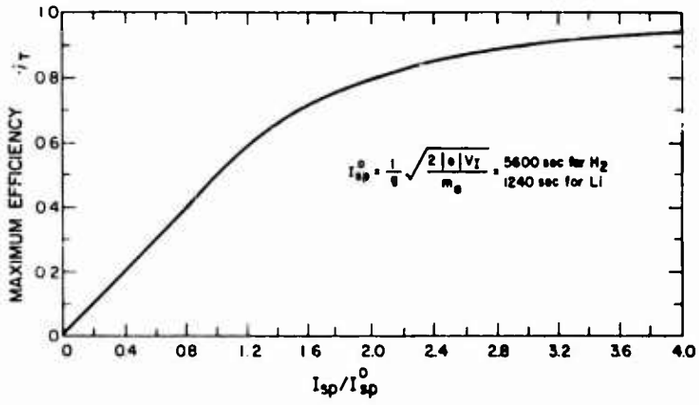

FIG. 8-3

MAXIMUM ATTAINABLE EFFICIENCY (infinite power)

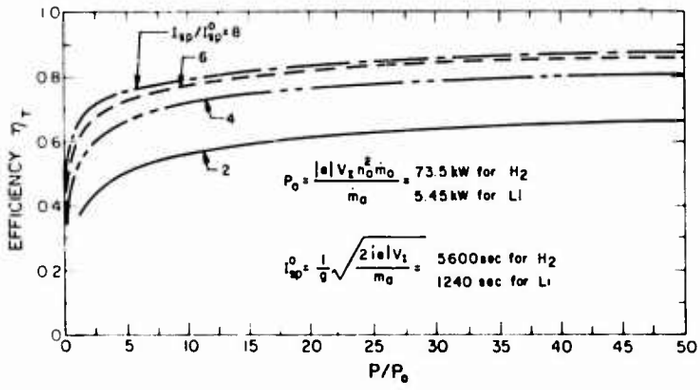

FIG. 8-4

THRUST EFFICIENCY AS A FUNCTION OF POWER

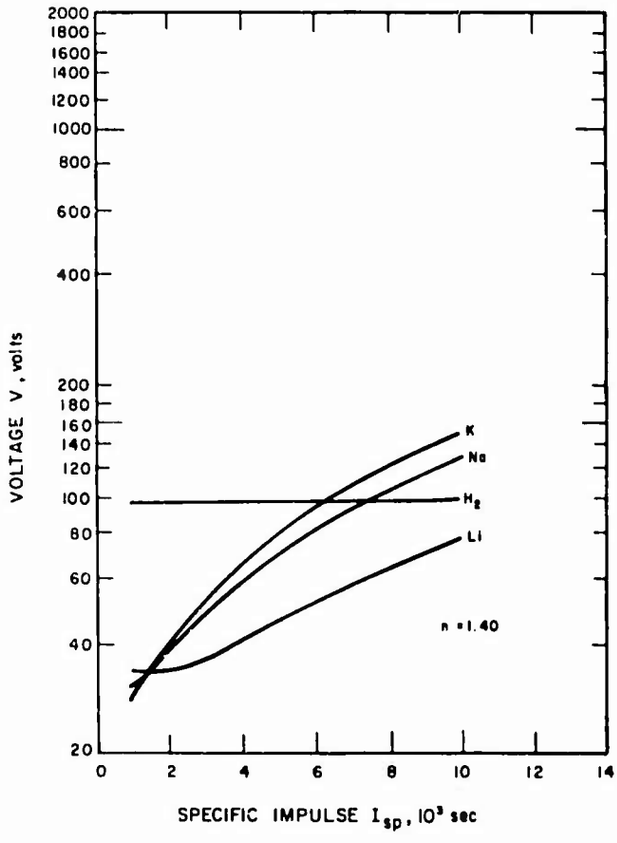

FIG. 8-5

VOLTAGE (calculated using concept of effective mass flow) AS A FUNCTION OF SPECIFIC IMPULSE FOR H_2, Li, Na, AND K

4. To obtain highest efficiency, Hall current accelerators must be operated at reasonably high power (to reduce the percentage power loss to the anode).
5. The analysis predicts that the thrust per unit current should be proportional to $\sqrt{\frac{2\,(1+n)\,m_a\,V_I}{|e|}}$. This relation can be checked experimentally by conducting tests with various propellants. Preliminary information using lithium and sodium as propellants indicates that for high propellant mass flow rate the thrust per unit current is a constant, independent of the type of propellant. If further tests confirm these results it will be necessary to modify the above analysis accordingly.

9. PROPELLANT SELECTION

Lithium was chosen as the most promising propellant for the Hall arc jet because of its low atomic weight, low first ionization potential per atomic mass unit (compared to previous arc jet propellants), high second ionization potential, and high latent heat of vaporization. These factors were all apparently important at the beginning of this work when the high-I_{sp} electromagnetic arc jets had been demonstrated only with hydrogen. The efficiencies measured with hydrogen, for both the electromagnetic arc jets using self-induced magnetic fields and the Hall arc jets using applied magnetic fields, agreed quite well with the theoretically predicted efficiencies based on complete ionization of hydrogen. However, it was necessary to operate the hydrogen arc jets at I_{sp} levels near 10,000 sec in order to obtain efficiencies equal to or greater than 50 percent. The next logical step was to investigate the performance capabilities of a propellant theoretically capable of higher efficiency at a lower range of I_{sp} (2000-5000 sec) since this was indicated to be the optimum for many missions.

9.1 Selection Criteria

The first consideration which may favor lithium over heavier alkali metal propellants is that of its lower atomic weight. For a temperature-limited thrustor such as a purely thermal arc jet, the maximum specific impulse is inversely proportional to the square root of the atomic or molecular weight of the propellant, if the maximum temperature is the same for each propellant. Although an electromagnetic device is not limited by the same mechanisms, as an electrothermal device, it still may have a maximum kinetic energy per particle or a maximum temperature as shown by the analysis in Section 8. If such temperature limits exist with an electromagnetic arc jet, it may be

possible that the required specific impulse levels, i.e., 2000 to 5000 sec, may not be possible with the heavier alkali propellants. This, of course, along with all the other considerations and comparisons of possible propellants, must be determined experimentally.

On the basis of only the first ionization energy losses, the highest theoretical or frozen flow efficiency would be achievable with the propellant having the lowest first ionization potential per atomic mass unit. Alkali metals are, of course, the elements that have the lowest values of this ratio and furthermore, since they all have about the same first ionization potential, the heaviest alkali metal would be chosen. (Frozen flow efficiencies based on complete first ionization for hydrogen, lithium, sodium, and potassium are compared in Fig. 9-1 as a function of specific impulse.) However, as Table 9-I shows, the heavier alkali metals have lower second ionization potential. It is possible that in the Hall arc jet all but lithium would be partially ionized twice and thus the advantage of lower first ionization losses would be offset.

An additional advantage of lithium is its latent heat of vaporization which is higher than the other alkali metals which, as shown in Section 10, is high enough to be effective in cooling the thrustor electrodes. This will allow the thrustor to operate at a lower temperature with lithium than with the other alkali metals and thereby increase its reliability and lifetime.

Other and more secondary considerations which may influence the choice of the best propellant in the future are as follows:

1. Comparison of insulator erosion in the various alkali metals.
2. Power requirements and complexity of the best feed systems for each propellant.
3. Effect of number density of the propellant particles on thrustor performance characteristics.
4. Arc voltage levels and over-all efficiency, including electrode losses and internal energy losses.

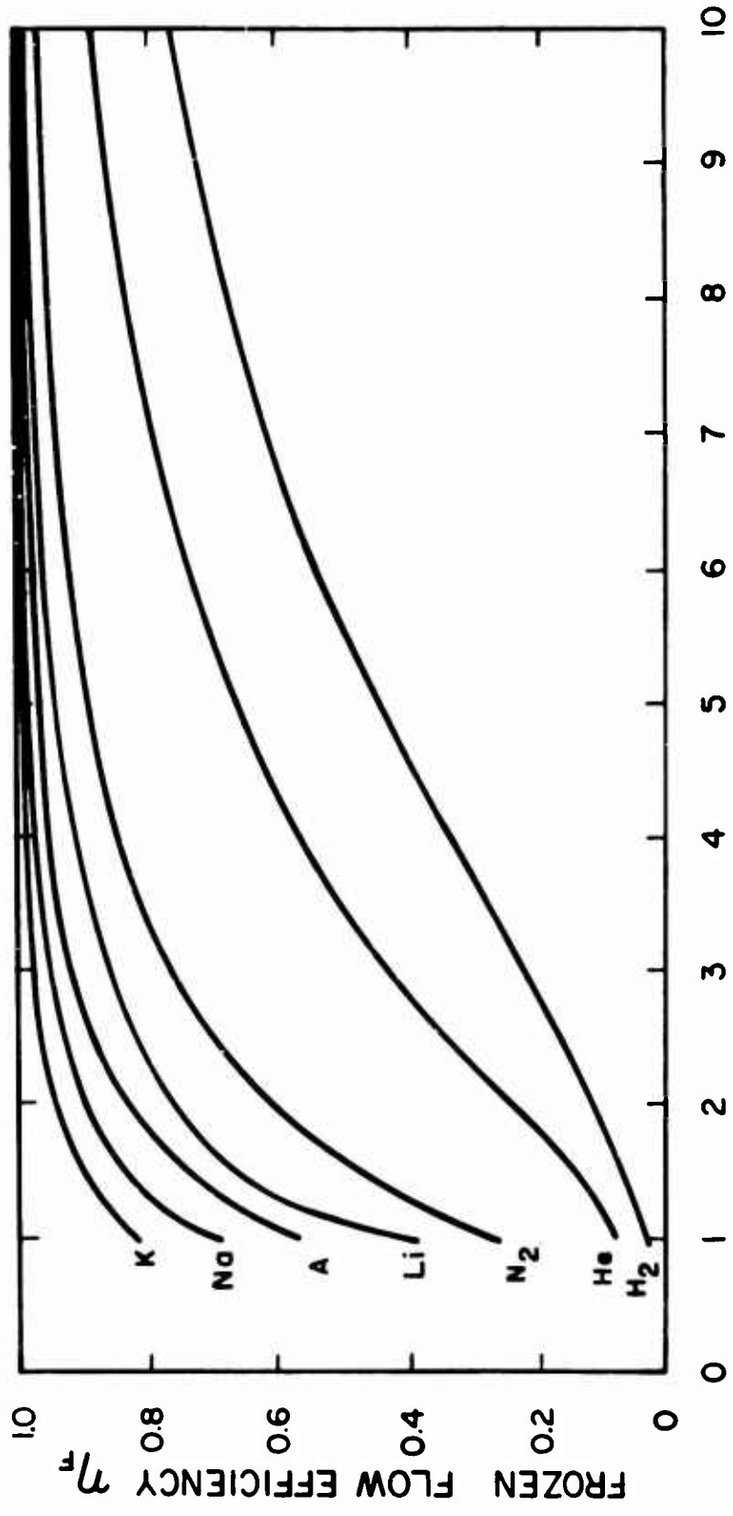

FIG. 9-1 FROZEN FLOW EFFICIENCY AS A FUNCTION OF SPECIFIC IMPULSE FOR H_2, Li, Na, AND K

TABLE 9-I

IONIZATION POTENTIALS FOR ALKALI METALS

	m_a	First Ionization		Second Ionization	
		V_I	V_I/m_a	V_I	V_I/m_a
Lithium	6.94	5.390	0.777	75.619	10.9
Sodium	22.99	5.138	0.224	47.29	2.06
Potassium	39.10	4.339	0.111	31.81	0.813
Rubidium	85.48	4.176	0.0488	27.5	0.322
Cesium	132.91	3.893	0.0293	25.1	0.189

9.2 Estimate of Over-all Efficiencies and Arc Voltage for Hydrogen, Lithium, Sodium, and Potassium

One of the criteria for propellant selection listed above is the relative arc voltage level and the over-all efficiency with various propellants. The upper limit of efficiency for a propellant that is completely ionized is the frozen flow efficiency, shown in Fig. 9-2 for lithium, hydrogen, sodium and potassium. A more realistic lower value of efficiency and an estimate of arc voltage were calculated on the basis of the following assumptions:

1. The cathode power loss is proportional to the current.

   $$P_c = 1.2\ I$$

2. The anode power loss is proportional to the current and to the ionization potential of the propellant.

   $$P_A = V_I\ I$$

3. The internal energy loss is the power required to heat the propellant to 10,000°K.

   $$P_{IE} = 5 \left(\frac{k}{|e|} \right) 10^4\ I$$

4. The current is proportional to the mass flow rate.

   $$I = \left(\frac{|e|}{m_a} \right) \dot{m}\ ,$$

where I is the arc current, V_I is the ionization potential, $\dot{m}$ is the propellant mass flow rate, m_a is molecular weight, $|e|$ is electronic charge, and P is the power loss.

Figure 9-2 shows this efficiency evaluated again for hydrogen, sodium and potassium, in addition to lithium. Hydrogen experimental results (Ref. 4) and the performance of model LAJ-AF-2 lithium thrustor are shown for comparison.

With the assumptions listed above, the arc voltage was computed as a function of the specific impulse (Fig. 9-3) for the same propellants as shown in Fig. 9-2. The theory predicts a strong

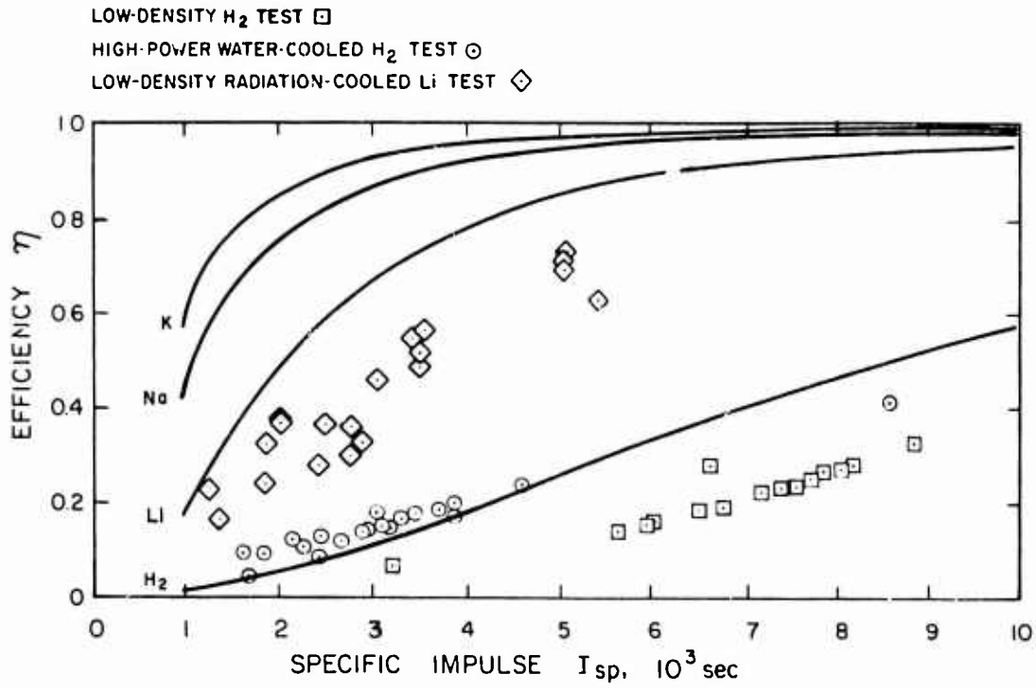

FIG. 9-2 THEORETICAL EFFICIENCY AS A FUNCTION OF SPECIFIC IMPULSE FOR H_2, Li, Na, AND K, TOGETHER WITH EXPERIMENTAL PERFORMANCE OF HYDROGEN AND LITHIUM THRUSTORS

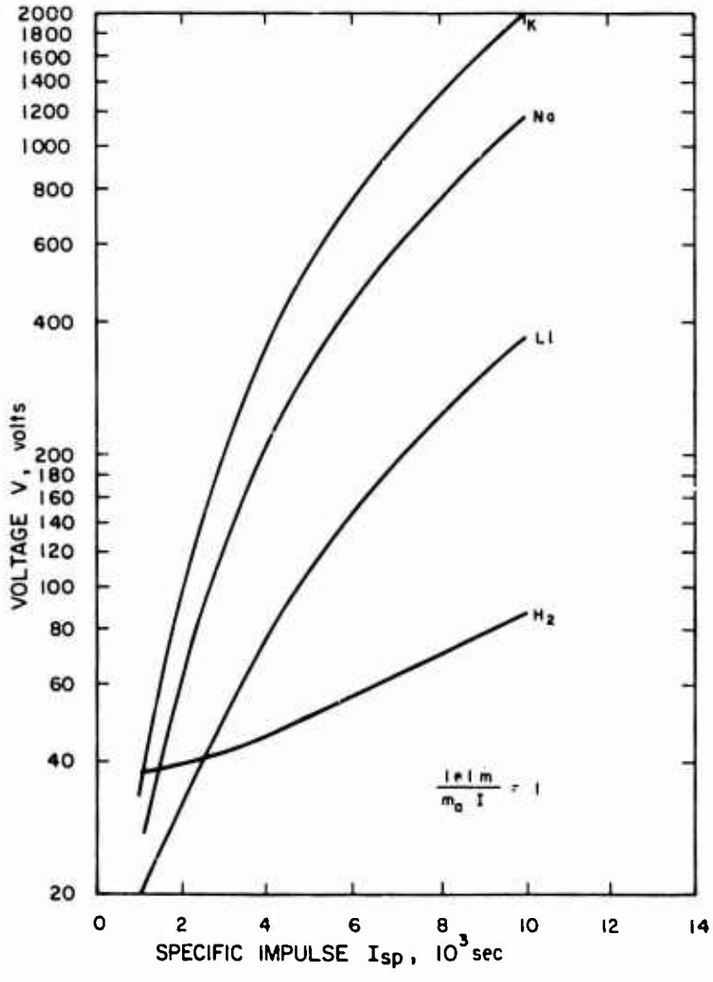

FIG. 9-3

THEORETICAL VOLTAGE AS A FUNCTION OF SPECIFIC IMPULSE FOR H_2, Li, Na, AND K

variation of voltage with specific impulse, which has not been observed with lithium or hydrogen. This discrepancy may be due to the fact that the current in the discharge is not limited to the assumed value of $I = (e/m_a)\dot{m}$. Without this limitation, the power input can be such that the energy per particle which is transferred to the gas is much larger than the equivalent number of electron volts. Provided that all of this energy can be transferred into directed kinetic energy, the exhaust velocity can be higher than could be obtained by accelerating the particle through the potential drop of the discharge. There are some measurements which indicate that Hall current accelerators can have exhaust velocities greater than the equivalent voltage drop (Refs. 16 and 17.)

9.3 Lithium Hydride

Before beginning the present program, lithium hydride was considered as a possible propellant in view of the possibility that a kinetic-energy-per-particle limit existed. The average atomic weight of the dissociated LiH is less than that of pure lithium. Lithium hydride, however, has a lower frozen flow efficiency than lithium because its average ionization potential per molecular weight unit is higher than lithium and it also has a dissociation loss. Because the early lithium results appeared to be close to the theoretically predicted efficiency, no further consideration was given to lithium hydride as a possible propellant.

9.4 Bipropellants

A bipropellant engine concept was studied both experimentally and analytically. This concept, as described in more detail in Section 7, uses a gaseous propellant in addition to the lithium. The gas was injected around the cathode and through a buffer or arc constrictor just downstream of the cathode to cause a small attachment area of the arc at the cathode. Although a thrustor of this type has been tested with hydrogen injection at the cathode, the eventual design would

probably use a storable propellant such as ammonia or methane for the cathode stabilization. Because of the high energy required to dissociate and ionize any gaseous or storable propellant, the ratio of the secondary propellant flow rate to the lithium flow rate must be small for high over-all efficiency. Figures 9-4 and 9-5 show the theoretical efficiencies for various ratios of hydrogen to lithium flow rate and ammonia to lithium flow rate. As these figures show, the mass flow ratios must be less than about 5 percent if the secondary propellant is not to lower the efficiency potential of pure lithium significantly.

Other bipropellants such as mixtures and eutectics of the alkali metals might have some advantages over any pure metal. It may be desirable to investigate these in later phases of the program.

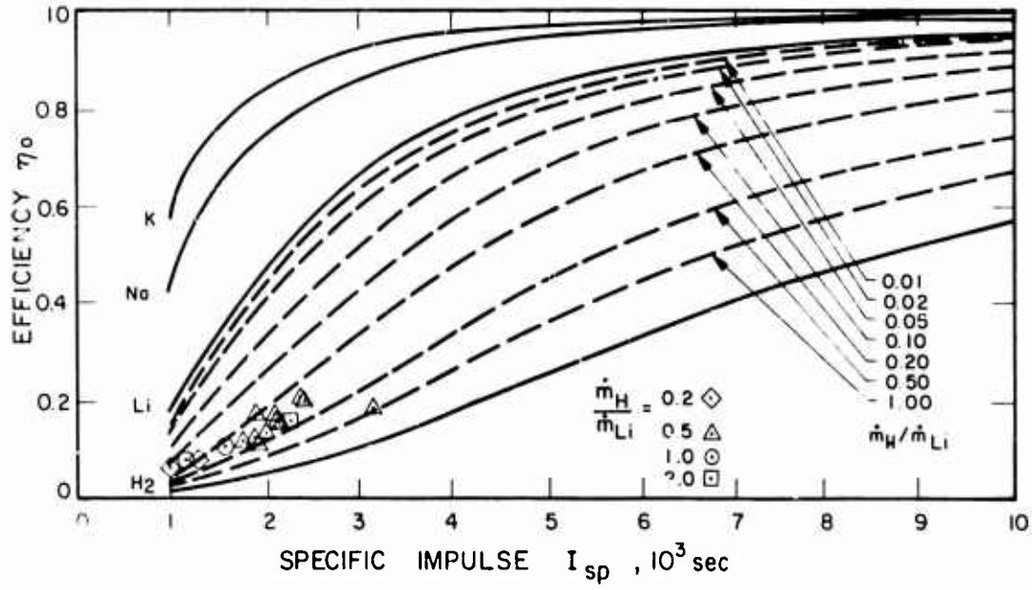

FIG. 9-4 THEORETICAL EFFICIENCY AS A FUNCTION OF SPECIFIC IMPULSE FOR VARIOUS RATIOS OF HYDROGEN TO LITHIUM FLOW RATE

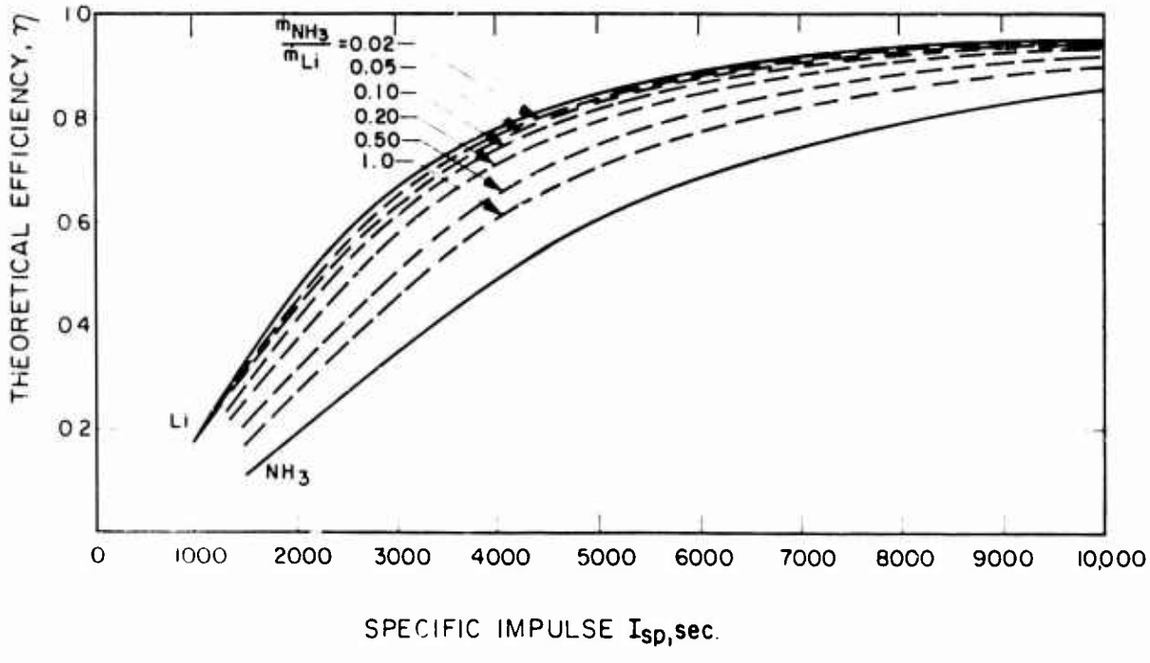

FIG. 9-5 THEORETICAL EFFICIENCY AS A FUNCTION OF SPECIFIC IMPULSE FOR VARIOUS RATIOS OF AMMONIA TO LITHIUM FLOW RATE

10. PREDICTION OF COOLING HEAT FLUX LIMITATIONS

The ultimate performance capabilities of a lithium arc jet will probably be determined by the cooling heat flux limitations at the electrode surfaces. The anode is more critical than the cathode because of larger power losses.

The electrodes may be cooled by radiation, regeneration and, if necessary, by a liquid coolant. A coolant may be required at high power levels, perhaps above 100-200 kW.

One method of liquid cooling is circulation of the lithium propellant from the storage tank through the engine, a radiator, and back to the tank. From preliminary calculations (Ref. 18), lithium appears to be a very effective coolant with high nucleate-boiling, burnout heat flux. At least, with this method, the required coolant weight may be minimized. However, with any method, liquid cooling adds complexity and weight to the propulsion system and will be avoided if possible.

10.1 Regenerative Cooling Capability

Lithium propellant is an effective regenerative coolant since it has a high latent heat of vaporization. The fraction of total power input which can be absorbed in vaporizing and heating the lithium to the operating temperature of the electrode surfaces is about 10 percent at I_{sp} of 1500 sec. This fraction decreases with I_{sp}; at I_{sp} of 4500 sec, it drops to about 1.7 percent.

These power input fractions were calculated after assuming that the overall engine efficiency, η_o, is 75 percent of the frozen-flow efficiency for complete ionization. The power input is thus

$$P_I = \frac{T^2}{2\dot{m}\,\eta_T} = \frac{T^2}{1.5\,\dot{m}\,\eta_F} \qquad (10\text{-}1)$$

The power absorbed by the lithium is

$$P_R = \dot{m} \Delta H , \tag{10-2}$$

where

$$\Delta H = \Delta h_v + (h_2 - h_1) + (h_4 - h_3) \tag{10-3}$$

and Δh_v is latent heat or vaporization, h_1 is enthalpy of liquid in the feed system, h_2 is enthalpy at saturated liquid state, h_3 is enthalpy at saturated vapor state, and h_4 is enthalpy of vapor at T = 3000°C, and maximum operating temperature of the electrodes. Combining Eqs. 10-1 and 10-2 yields

$$\frac{P_R}{P_I} = \frac{1.5\ \eta_F\ \Delta H}{I_{sp}^2} \tag{10-4}$$

Figure 10-1 is a graph of $\frac{P_R}{P_I}$ (the ratio of power absorbed rengeratively by the lithium to the total power input) as a function specific impulse. The thermodynamic properties of lithium required for this calculation were taken from Ref. 19.

Approximately 80 percent of the total power absorbed, P_r, is required to vaporize the lithium. The rest is the "sensible heat" required to increase the liquid temperature from 200°C (at the feed system) to that of the saturated liquid state and then to increase the temperature of the vapor to that of the electrode surfaces.

10.2 Anode Radiation Heat Transfer

To calculate the radiation heat flux for the arc jet configurations of current interest, the cylindrical disk geometry illustrated in Fig. 10-2 was assumed. In this model, the temperature of the inside surface of the disk is constant at near the melting point of tungsten. Heat conducts radially outward through the disk and radiates from the flat surfaces. The temperature distribution must

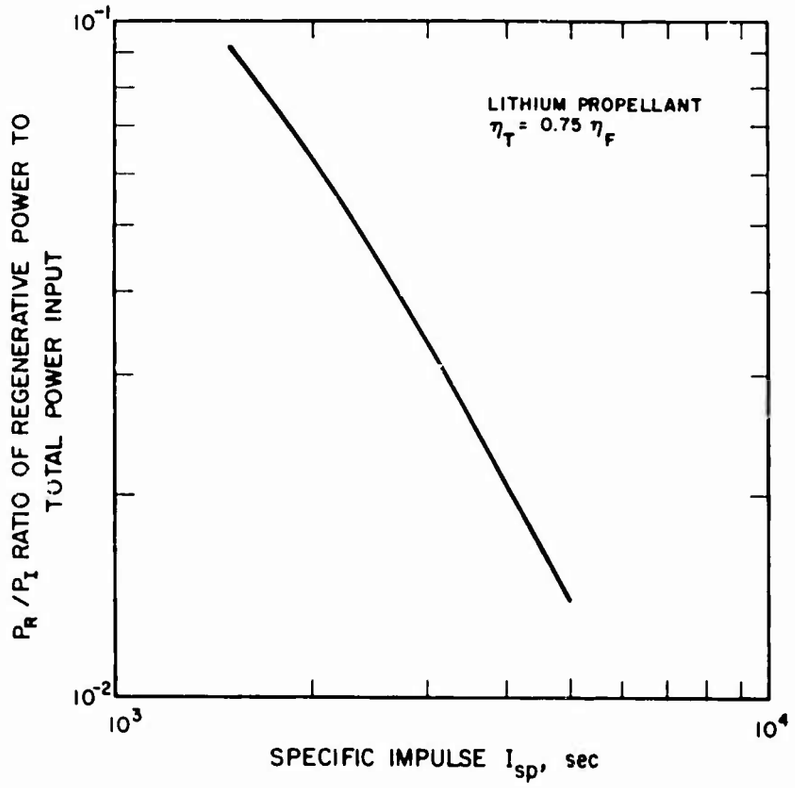

FIG. 10-1

RATIO OF REGENERATIVE POWER TO TOTAL POWER INPUT AS A FUNCTION OF SPECIFIC IMPULSE

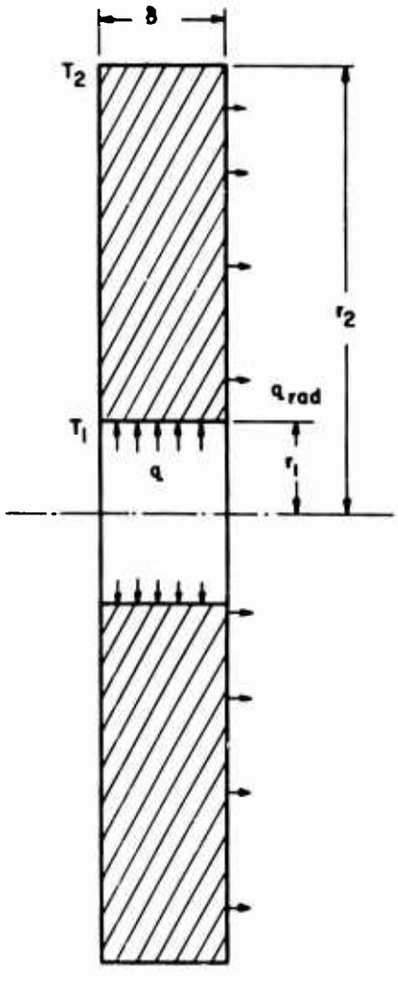

FIG. 10-2

ANODE GEOMETRY ASSUMED FOR HEAT TRANSFER CALCULATION

satisfy the following energy-balance differential equation:

$$\frac{d}{dr}\left(kr\,\frac{dT}{dr}\right) - \frac{\sigma\epsilon r T^4}{\delta} = 0 \qquad (10\text{-}5)$$

The boundary conditions are

$$T(r_1) = T_1, \text{ melting point of tungsten}$$

$$\frac{dT(r_2)}{dr} = 0$$

The second boundary condition obtains only when $r_2 \gg r_1$ or, more precisely, when

$$k_1 r_1 \frac{dT(r_1)}{dr} \gg k_2 r_2 \frac{dT(r_2)}{dr} .$$

Equation 10-5 was solvered numerically by Chambers and Somers (Ref. 20) for constant thermal conductivity and emissivity. They found that the fin efficiency, given by

$$\eta_f = \frac{Q}{Q_{max}} = \frac{Q}{\pi\epsilon T_1^4 (r_2^2 - r_1^2)} \qquad (10\text{-}6)$$

depended only on the parameter $\frac{r_2}{r_1}$ and on

$$\sqrt{\gamma} = \sqrt{\frac{\epsilon\sigma T_1^3}{k\delta}}\ (r_2 - r_1). \qquad (10\text{-}7)$$

Figure 10-3 taken from Ref. 20 illustrates their results.

For the present case, the assumption of constant thermal conductivity is not a good one, since thermal conductivity varies greatly with temperature and the temperature of the disk depends strongly on radial position. The solution of Eq. 10-5 given in Ref. 20

may be used for variable conductivity if temperature in the differential equation is transformed* to the thermal conductivity integral as follows:

$$\phi = \int_0^T k \, dT \tag{10-8}$$

As Fig. 10-4 shows, the thermal conductivity integral, ϕ, is a linear function of temperature for tungsten, i.e.,

$$\phi = A T \tag{10-9}$$

The differential equation (Eq. 10-5), in terms of ϕ, is

$$\frac{d}{dr}\left(r \frac{d\phi}{dr}\right) - \frac{\sigma \epsilon r \phi^4}{A^4 \delta} = 0 . \tag{10-10}$$

The parameter $\sqrt{\gamma}$ appearing in the solution of Chambers and Somers transforms to

$$\sqrt{\gamma'} = \sqrt{\frac{\sigma \epsilon \phi_1^3}{A^4 \delta}} \, (r_2 - r_1) \tag{10-11}$$

Their solution was used by taking η_f from Fig. 10-3 as a function of the modified parameter $\sqrt{\gamma'}$. Total heat transfer Q and heat flux q, given by

$$q = \frac{Q}{\pi r_2^2} , \tag{10-12}$$

were then calculated from Eqs. 10-6 and 10-12. Figures 10-5 through 10-8 show the results for various values of thickness δ, emissivity ϵ, and inside radius r_1.

---

*Kirchhoff's transformation

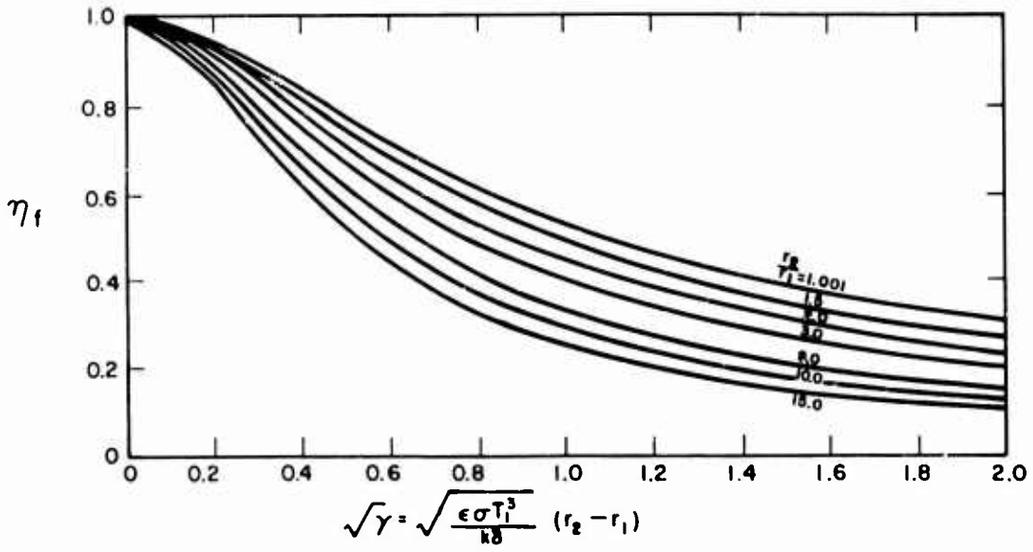

FIG. 10-3 FIN EFFICIENCY AS A FUNCTION OF CONDUCTION PARAMETER

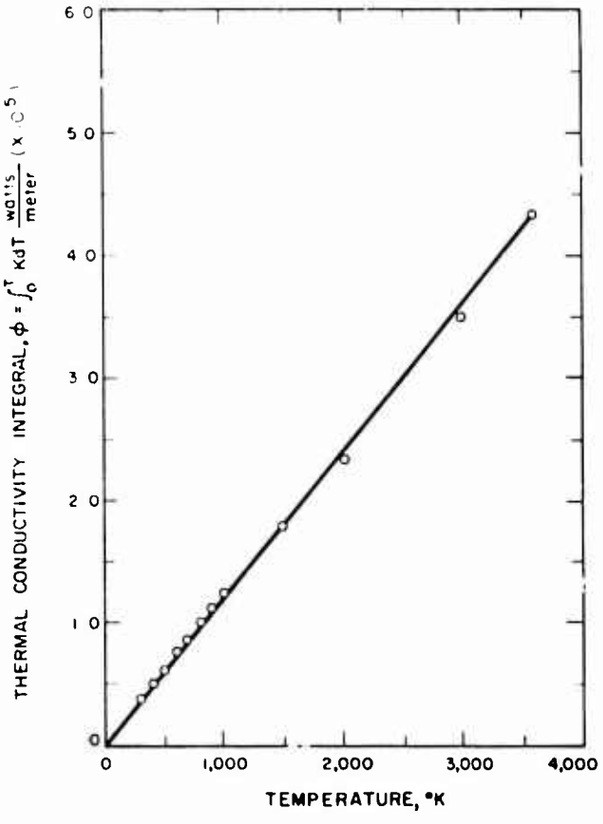

FIG. 10-4 THERMAL CONDUCTIVITY INTEGRAL AS A FUNCTION OF TEMPERATURE FOR TUNGSTEN

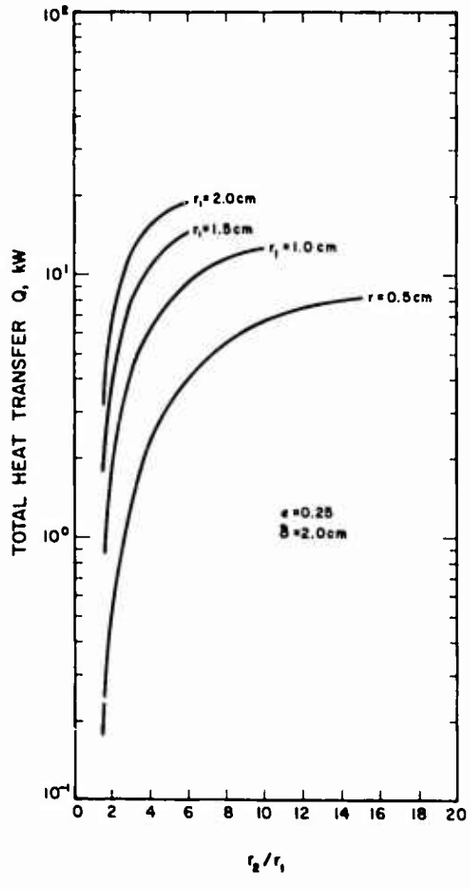

FIG. 10-5 THEORETICAL HEAT TRANSFER RADIATED FROM ANODE FACE

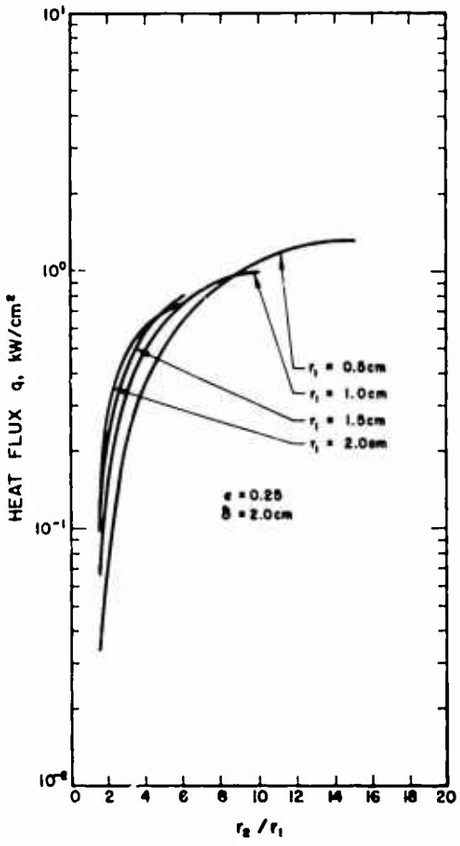

FIG. 10-6 THEORETICAL HEAT FLUX (based on internal surface area) RADIATED FROM ANODE FACE

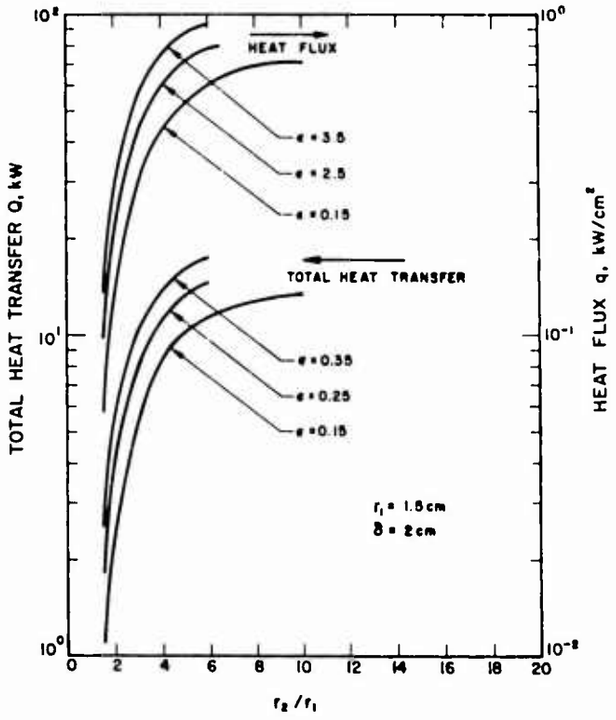

FIG. 10-7 THEORETICAL EFFECT OF EMISSIVITY ON HEAT TRANSFER RADIATED FROM ANODE FACE

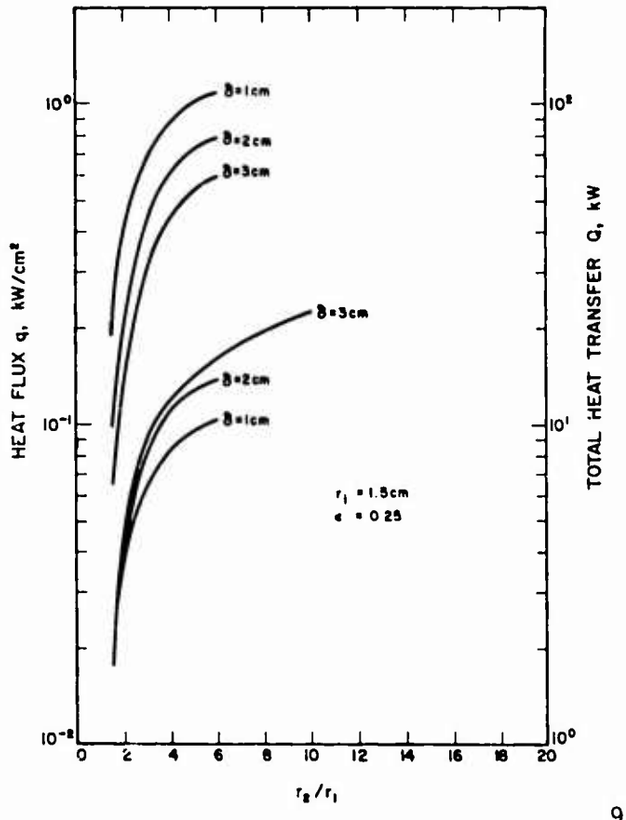

FIG. 10-8

THEORETICAL EFFECT OF THICKNESS ON HEAT RADIATED FROM ANODE SURFACE

Actually, the emissivity is a function of temperature and, if it is treated as such, the differential equation (Eq. 10-5) would require a different numerical solution. This is not justified at the present time since the analytic model (Fig. 10-2) may not accurately represent the thrustor either presently or in the future.

The maximum radiation from tungsten anodes of this type is estimated from the present calculations to be about 20 kW. The minimum heat transfer from the arc to the anode is of the order of $\chi_A I$, where χ_A is the rework function of the anode material and I is the arc current. For tungsten, χ_A is about 5 volts. If the arc voltage is 100 volts, the minimum heat loss to the anode is 5 percent of the power input. This minimum is never actually realized since there must always be some heat transfer by conduction, convection and radiation from the propellant to the anode. For water-cooled thrustors of this type operating with hydrogen, the measured total power loss to the anode varies from 15 to 30 percent of the total power input (Refs. 3 and 16).

If we arbitrarily assume that the minimum anode power loss to the lithium arc jet will be 10 to 15 percent, the loss is equal to the maximum surface radiation at input power levels between 133 and 200 kW. If lithium is injected at the anode, the anode cooling limit is increased by the regenerative cooling capability, which depends on specific impulse as shown in Fig. 10-1. Figure 10-9 shows the power region as a function of I_{sp}, where the minimum anode loss (10-15 percent) is equal to the estimated maximum which can be radiated plus that which is absorbed regeneratively. Above 150 to 250 kW at I_{sp} of 4000 sec, the minimum loss exceeds the cooling capability and some method of increasing the radiation limit must be found or else an external coolant will be required.

There are a number of ways to increase the radiation limit:

1. Increase of surface emissivity with a coating of another material or through the use of fins or grooves.

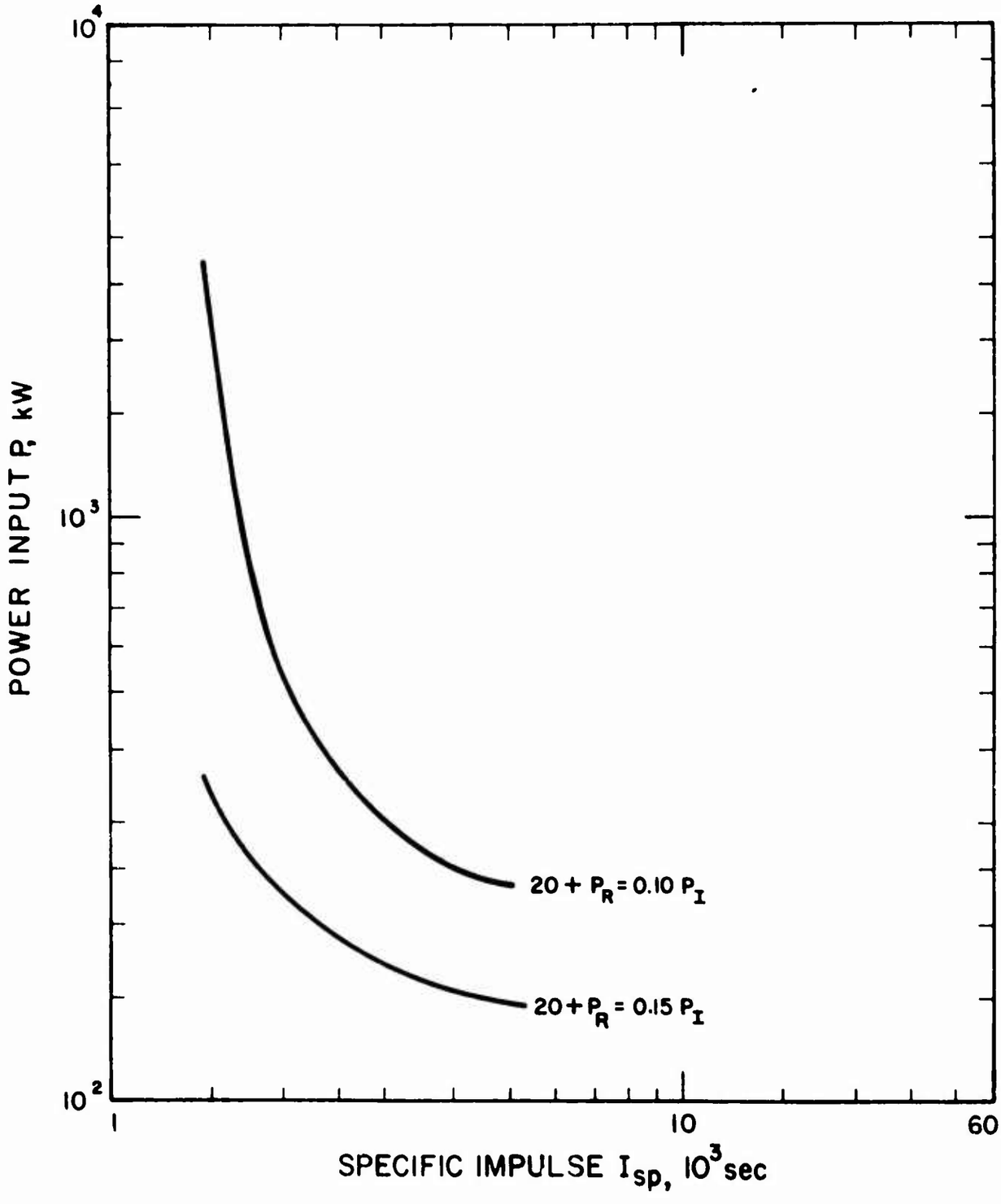

FIG. 10-9 POWER LIMIT WHERE HEAT TRANSFER TO ANODE IS EQUAL TO MAXIMUM COOLING CAPABILITY

2. Use of a composite anode structure with an inner part of tungsten and an outer part of material with higher thermal conductivity or emissivity or both.
3. Modification of the anode configuration to provide for higher heat conductance between the inner surface and the outer radiating surface.

These techniques will be investigated analytically and possibly experimentally in the remaining tasks of the program.

11. PRELIMINARY EVALUATION OF MAGNET POWER AND WEIGHT REQUIREMENTS

The minimum weights of magnet systems for use with a lithium arc jet propulsion system were determined for air core electromagnets and were compared with other magnetic field sources. For fields up to 0.5 Wb/m^2 (5000 gauss), a copper solenoidal magnet cooled by an external thermal radiator has the lowest weight of the magnet systems considered. The minimum weights for fields of 0.2 and 0.5 Wb/m^2 (2000 and 5000 gauss) are 19 and 82 kilograms, respectively, using a solenoid with 0.03 meters inside radius, a power supply "power density" of 0.01 kg/W (22.4 lb/kW), and a radiator density of 5 kg/m^2.

11.1 Introduction

Lithium arc jets show promise for advanced space propulsion system use, provided the power requirements, engine performance, and system weight are competitive with other propulsion systems. Consequently, the weight of the arc jet and its associated equipment must be minimized to provide the values of thrust, thrust energy, and specific impulse required for the particular mission.

A significant portion of the total arc jet system weight may be incorporated in the magnet required for an efficient lithium arc. This study considers the major factors which determine the magnet system weight, and determines the minimum weight for representative magnet designs.

Only the major components of the magnet system - the magnet, its power source, and the thermal radiator - have been considered in detail in this study. The weights of other associated components (controls and instrumentation, coolant pumping, etc.) have been assumed to be of secondary importance, and have not been included in the calculations (except in special cases).

The most important factors which determine magnet system weight are as follows:

1. Magnetic field strength.
2. Sources of magnetic field (e.g., electromagnets and permanent magnets).
3. Magnet geometry and field shape.
4. Magnet temperature and cooling technique.
5. Magnet materials.
6. Weight of power supply, thermal radiators, and refrigerators.

The conclusions regarding these factors are summarized in the following paragraphs.

11.2 Magnetic Field Requirements

Some aspects of magnetic field requirements for lithium arc jets are understood. However, the detailed relationship between magnetic field strength, thrust efficiency and engine lifetime is not yet clearly known, since a wide variation of magnetic field strength and field shape conditions are possible for each specific electrode design and for different mass flow and power input conditions.

Present experimental magnets provide a strong, nearly uniform axial magnetic field in the cathode region; the field diverges rapidly near the anode and downstream of the anode. The applied magnetic field in the cathode region is normally greater than 0.1 Wb/m^2 (1000 gauss) for present lithium engines. For lower values of the magnetic field, the arc current interaction with the magnetic field does not provide sufficient Hall currents for efficient operation. An increase in magnetic field strength above 0.1 Wb/m^2 will increase the engine thrust and efficiency. The field strength in present engines has varied from 0.1 to 0.5 Wb/m^2 (1000 to 5000 gauss), but is normally 0.3 to 0.5 Wb/m^2.

11.3 Magnet System Weight Minimization

The objective of the preliminary study has been to calculate the relationship between minimum magnet system weight and the maximum

axial magnetic field strength $B_z(r,z)$. This is a simplification of the more general problem of determining the minimum <u>total</u> arc jet system weight required to meet specific mission objectives, but only the magnet study is justified at the present time.

For the cases considered, the minimum magnet system weight is provided by a copper solenoidal magnet coil, using a non-uniform current density, and cooled by an external thermal radiator. A summary of the results is given in Table II-I and the details are included in Appendix I. At 0.5 Wb/m^2 (5000 gauss), the minimum magnet weight is about 85 kg, using a solenoid of 0.03 meters inside radius, a power supply "power density" of 0.01 kg/W (22 lb/kW), and a thermal radiator density of 5 kg/m^2.

The total weight of a system using a copper magnet, cooled by thermal radiation from its external surface, is about 50 percent greater, but may be justified for small systems, where a coolant pumping system would add much more weight. The weight for aluminum magnet coil systems would be about 50 percent greater than for copper coils producing the same field strength, despite the material's lower density.

Low temperature magnets and superconducting cryogenic magnets were considered for production of magnetic fields for lithium arc engine systems. Because of the low temperature, a large thermal radiator (and perhaps a refrigerator) will be needed to reject the required heat. For a superconducting magnet, the weight of the refrigerator and its power supply is greater than the weight savings realized by using the cryogenic system. A refrigerator system and magnet operating at intermediate temperatures may prove feasible for this application, provided waste heat from a nuclear reactor can be used to drive the refrigeration system.

The need for a magnet power supply would be eliminated entirely with the use of permanent magnets. Unfortunately, permanent magnets with large air gaps are limited to low magnetic fields (about 0.1 Wb/m^2) and are heavier than a comparable electromagnet system.

TABLE 11-I

SUMMARY OF MINIMUM MAGNET SYSTEM WEIGHT CALCULATIONS FOR AIR CORE ELECTROMAGNETS

Configuration	Material		Cooling		Power Supply "Power Density" w_{PS}		Min. Magnet System Weight W_T (Kg)	
	Copper	Aluminum	Self-Cooled	External-Radiator-Cooled	0.01 kg/W (22.4 lb/kW)	0.02 kg/W (44.8 lb/kW)	.2 Wb/m^2 (2000 gauss)	.5 Wb/m^2 (5000 gauss)
Uniform Current Density Solenoid								
	x		x		x		30	295
	x		x			x	60	>400
	x			x	x		21	98
	x			x		x	29	220
		x	x		x		45	>400
		x	x			x	80	High
		x		x	x		29	160
		x		x		x	43	High
Bitter Solenoid	x		x		x		30	180
	x		x			x	47	296
	x			x	x		19	82
	x			x		x	27	118

Solenoid Inside Radius: 0.03 meters

$\epsilon = 1.0$

$\lambda = 1.0$

Max. Magnet Temperature: Copper $1000^{o}K$
Aluminum $700^{o}K$

The magnetic field of electromagnets and permanent magnets may be shaped and concentrated by the use of iron or other ferromagnetic materials. The weight savings to be gained will depend primarily upon the desired magnetic field distribution and is unique for each magnet geometry.

REFERENCES

1. High Specific Impulse Thermo-Ionic Acceleration, Giannini Scientific Corp., Report No. RRE-114-a, Santa Ana, California, Dec 1963

2. G. L. Cann, Thermal Arc Jet Research, EOS Report 3810-ML-11, Contract No. AF33(657)-10789, 15 Feb 1964

3. R. A. Moore, G. L. Cann, et al, Thermal Arc Jet Research, TDR No. APL-TDR-64-55, Air Force Aero Propulsion Laboratory, May 1964

4. G. L. Cann, P. D. Lenn, and R. L. Harder, Hall Current Accelerator, EOS Report 5470-QL-1, Contract No. NAS3-5989, 5 Oct 1964

5. G. L. Cann, P. D. Lenn, R. L. Harder, Hall Current Accelerator, Second Quarterly Progress Report on Contract NAS3-5909, NASA/Lewis Research Center, 20 Dec 1964

6. G. L. Cann, P. D. Lenn, R. L. Harder, Hall Current Accelerator, Third Quarterly Progress Report on Contract NAS3-5909, NASA/Lewis Research Center, 20 Mar 1965

7. Arc Jet Technology Research and Development, First Quarterly Progress Report, Avco RAD SR-64-239, Contract NAS3-5900, Oct 1964

8. Arc Jet Technology Research and Development, Second Quarterly Progress Report, Avco RAD SR-65-5, Contract NAS3-5900, Dec 1964

9. A. C. Ducati, E. Muehlberger, and J. P. Todd, Design and Development of a Thermo-Ionic Electric Thrustor, Giannini Scientific Corp. Interim Report on Contract No. NASw-968, Sep 1964

10. A. C. Ducati, E. Muehlberger, and J. P. Todd, Design and Development of a Thermo-Ionic Electric Thrustor, Giannini Scientific Corp. Interim Report on Contract No. NASw-968, Feb 1965

11. R. M. Patrick, Study of Magnetic Annular Plasma Accelerator, Second Quarterly Progress Report on Contract No. NAS3-5748, Sep 1964

12. Avco Research Laboratory, Study of Magnetic Annular Plasma Accelerator, Third Quarterly Progress Report, Contract NAS3-5748, 1 Oct-31 Dec 1964

REFERENCES (contd)

13. Arc Jet Technology Research and Development, Third Quarterly Progress Report, Avco RAD-SR-65-92, Contract NAS3-5900, Mar 1965

14. R. A. Moore, G. L. Cann, et al, High Specific Impulse Thermal Arc Jet Thrustor Technology, Interim Technical Report on Contract AF 33(615)-1579, Air Force Aero Propulsion Laboratory, 30 Nov 1964

15. G. L. Cann and R. A. Moore, High Specific Impulse Thermal Arc Jet Thrustor Technology, Monthly Progress Reports on Contract AF 33(615)-1579, Air Force Aero Propulsion Laboratory, EOS Reports 5090-ML-3 through 5090-ML-12, 10 Jul 1964 through 10 Apr 1965

16. G. L. Cann and R. L. Harder, Follow-On Investigation of a Steady State Hall Current Accelerator, NASA/Lewis Research Center Report NAS CR-54062, 30 Oct 1964

17. W. Grossman, R. V. Hess, and H. A. Hassan, Experiments with a Coaxial Hall Current Plasma Accelerator, AIAA Reprint No. 64-700

APPENDIX I

ANALYSIS OF MAGNET POWER AND WEIGHT REQUIREMENTS

Solenoidal air-core electromagnet systems were considered in greatest detail because of the low system weights possible. Solenoidal magnets with two different current distributions were optimized in detail for a magnet with an inside radius of 0.03 meter. A third current distribution is discussed for reference purposes.

The electromagnets were analyzed for two cooling techniques: thermal radiation from the outer surfaces of the electromagnet; and thermal radiation from an external radiator. These two cases are designated as the self-cooled solenoid and the external-radiator-cooled solenoid, respectively.

For analytical purposes, the electromagnet is assumed to be isothermal, i.e., the temperature gradients due to the thermal conductivity of the metal and the electrical insulation are assumed to be negligible relative to the temperature of the thermal radiators.

The "power density" of the magnet power supply has been taken to be 0.01 to 0.02 kg/W (22.4 to 44.8 lb/kW). These values result from electric propulsion studies, which show that electric rockets will become attractive only when "power densities" below approximately 0.02 kg/W are achieved.

I.1 Solenoidal Air Core Magnet Designs

The locus of the maximum value of the axial magnetic field $B_z(r,z)$ for a solenoidal magnet is halfway between the ends of the solenoid. The axial magnetic field at this point is given by the Fabry formula (Refs. I-1 through I-4).

$$B_z(0,0) = B_o = G' \left(\frac{P\lambda}{\rho r_i}\right)^{1/2} , \qquad (I\text{-}1)$$

where B_o is the axial magnetic field strength on axis at the center of the solenoid, in Wb/m^2*; P is power dissipated in the solenoid, in watts; λ is the fraction of volume occupied by the conductor; ρ is resistivity of coil conductor, in ohm-meters; r_i is the inside radius of the solenoid, in meters; and G' is a geometrical factor which depends on the coil geometry and the current density distribution in the coil**, in henrys/meter. The solenoid coil shape was assumed to be a hollow right circular cylinder with inner radius r_i, an outer radius $r_o = \alpha r_i$, and length $L = 2\beta r_i$.

Three current distributions of practical interest are

1. Solenoid with uniform current density
2. Bitter solenoid
3. Gaumé solenoid

The Bitter and Gaumé solenoids require less power (and less weight) for a given value of B_o than the uniform current density solenoid. The current density distributions and G' factors for these three geometries are given in Figs. I-1 through I-4.

I.1.1 Solenoid with Uniform Current Density

I.1.1.1 Self-Cooled Solenoid

The four curves in Fig. I-5 give the minimum magnet system weights for power supply "power densities" w_{PS} of 0.01 and 0.02 kg/W (22.4 and 44.8 lb/kW) and for copper and aluminum solenoids.

Solenoids with the highest radiating temperature have the lowest magnet system weight for fields greater than 0.2 Wb/m^2 (2000 gauss). The maximum temperature values used in this

* 1 $Wb/m^2 = 10^4$ gauss

** $G' = 10^{-6}$ G, where G is the geometrical factor used in Refs. I-1 through I-4

NOTE $G' = 10^{-6} G$, WHERE G IS THE G-FACTOR COMMONLY USED BY MAGNET DESIGNERS (Refs I-1 THROUGH I-3)

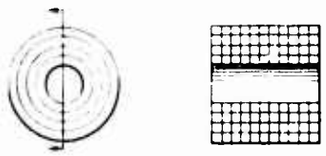

UNIFORM CURRENT DENSITY SOLENOID

$J = \text{CONSTANT}$

$$G' = \mu_0 \left[\frac{\beta}{2\pi(\alpha^2 - 1)} \right]^{1/2} \ln \frac{\alpha + \sqrt{\alpha^2 + \beta^2}}{1 + \sqrt{1 + \beta^2}}$$

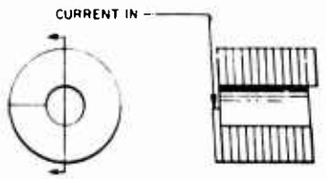

BITTER SOLENOID

$$J \propto \frac{1}{r}$$

$$G' = \mu_0 \left[\frac{1}{4\pi\beta \ln \alpha} \right]^{1/2} \ln \left[\alpha_0 \frac{\beta + \sqrt{1 + \beta^2}}{\beta + \sqrt{\alpha^2 + \beta^2}} \right]$$

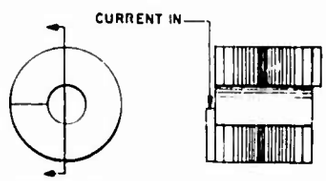

GAUME' SOLENOID

$$J \propto \frac{1}{r} \left(\frac{a}{a-1} \right) \left[\frac{r_1}{\sqrt{Z^2 + r_1^2}} - \frac{r_1}{\sqrt{Z^2 + a^2 r_1^2}} \right]$$

$$G' = \mu_0 \left[\frac{1}{4\pi \ln \alpha} \right]^{1/2} \left[\tan^{-1}\beta + \frac{1}{\alpha} \tan^{-1} \frac{\beta}{\alpha} - \frac{2}{\alpha} F\left(\tan^{-1}\beta, \frac{\sqrt{\alpha^2 - 1}}{\alpha} \right) \right]$$

WHERE $F\left(\tan^{-1}\beta, \frac{\sqrt{\alpha^2-1}}{\alpha}\right)$ IS AN ELLIPTICAL INTEGRAL OF THE FIRST KIND

FIG. I-1

CURRENT DISTRIBUTION AND G'-FACTORS FOR THREE AIR-CORE SOLENOID DESIGNS

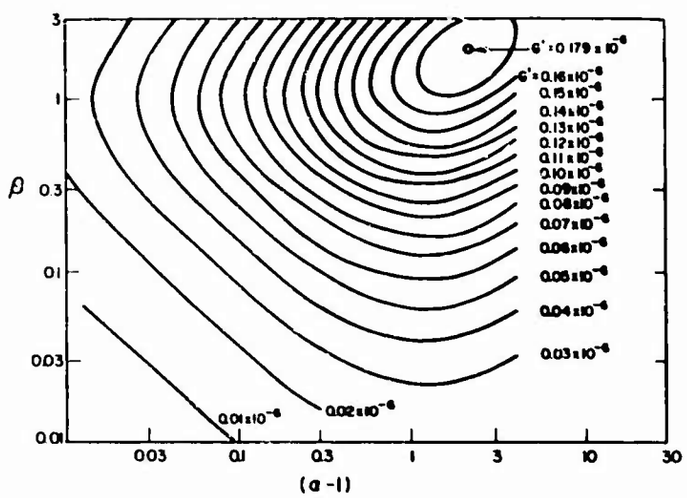

FIG. I-2

G'-FACTORS FOR UNIFORM CURRENT DENSITY SOLENOID

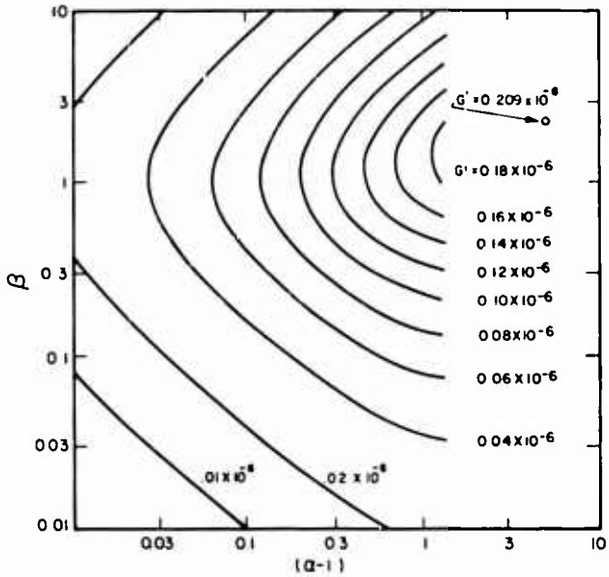

FIG. I-3

G'-FACTORS FOR
BITTER SOLENOID

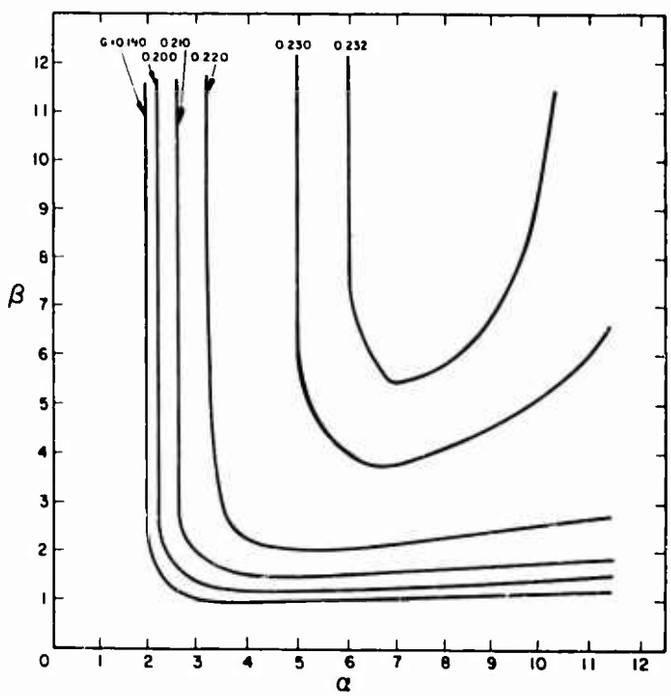

FIG. I-4

G'-FACTORS FOR
GAUME' SOLENOID

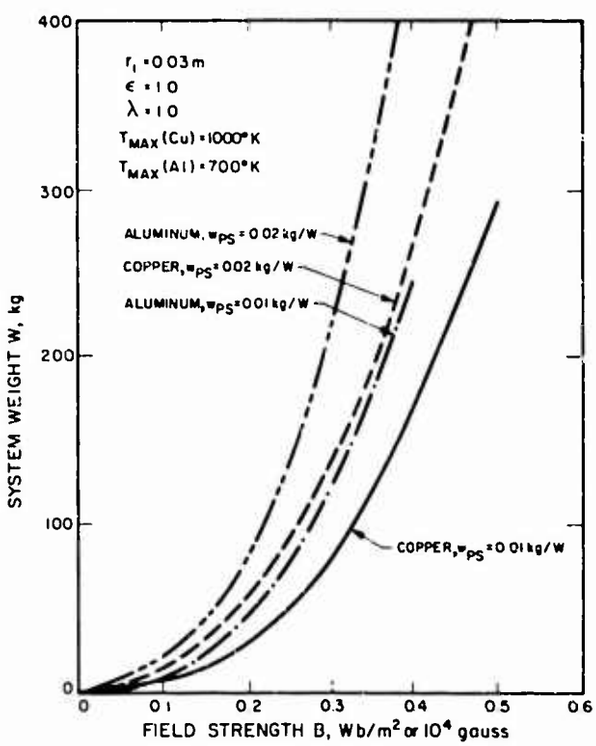

FIG. I-5

SYSTEM WEIGHTS FOR
UNIFORM CURRENT DENSITY
SOLENOID, SELF-COOLED

computation were 1000°K for copper and 700°K for aluminum. If higher operating temperatures can be used with these materials, then lower magnet system weights can be attained.

The maximum magnetic field in a solenoid which has a constant current density j_θ throughout is given by

$$B_o = \mu_o \left[\frac{\beta}{2\pi(\alpha^2 - 1)}\right]^{1/2} \ln \frac{\alpha + \sqrt{\alpha^2 + \beta^2}}{1 + \sqrt{1 + \beta^2}} \left(\frac{P\lambda}{r_i \rho}\right)^{1/2}, \quad \text{(I-2)}$$

where α is the ratio of the external radius to the internal radius of the solenoid, and β is the ratio of solenoid length to the inside diameter.

The power dissipated in the solenoid must be radiated from the two end surfaces and the outside surface. Thus,

$$P = \epsilon\sigma T^4 \cdot 4\pi r_i^2 \left(\alpha\beta + \frac{\alpha^2 - 1}{2}\right) \quad \text{(I-3)}$$

and

$$B_o = \mu_o \left[\frac{\epsilon\sigma T^4 \lambda\, r_i}{\rho(T)}\right]^{1/2} \left[\frac{2\beta\left(\alpha\beta + \frac{\alpha^2 - 1}{2}\right)}{\alpha^2 - 1}\right]^{1/2} \ln \frac{\alpha + \sqrt{\alpha^2 + \beta^2}}{1 + \sqrt{1 + \beta^2}}, \quad \text{(I-4)}$$

where ϵ is emissivity of the solenoid surface; σ is the Stefan-Boltzmann constant, 5.6×10^{-16} W/m^2-(°K)^4; and T is the absolute temperature of the solenoid in °K. The magnetic field is, therefore, a function of the geometrical factors α and β and of the coil temperature T. It is to be noted that the resistivity ρ of the coil material is also a function of temperature.

The major weight of the magnet system includes the weights of the magnet and of the magnet power supply. Since the power dissipated and radiated from the magnet must equal the input power,

$$W_T = w_{PS} P + w_M V_M$$

$$= w_{PS} \epsilon\sigma T^4 \cdot 4\pi r_i^2 \left(\alpha\beta + \frac{\alpha^2 - 1}{2}\right) + w_M \cdot 2\pi r_i^3 \beta (\alpha^2 - 1) , \quad (I\text{-}5)$$

where W_T is the magnet system weight, in kg; w_{PS} is the power supply "power density," in kg/W; w_M is the density of the magnet material, in kg/m^3; and V_M is magnet volume. Thus, the system weight is also a function of the three parameters α, β, and T.

An analytical solution for W_T in terms of B_o could, in principal, be obtained by solving for one of the independent variables α, β, or T and eliminating it from the equations, but the resulting equation would be very complex and unwieldy. Then the magnet system weight W_T could be numerically evaluated as a function of B_o, using various combinations of discrete values for the other independent variables. The minimum weight determined for a given magnetic field B_o would be the required minimum magnet system weight.

A simpler approach was to calculate B_o and W_T for combinations of discrete values of α, β, and T, using the appropriate values of the constants ϵ (1.0), σ, r, λ (1) and using 0.01 and 0.02 kg/W or 22.4 and 44.8 lb/kW for w_{PS} and the values of w_M for copper and aluminum magnet conductors.

The numerical solutions for B_o and W_T were tabulated with a digital computer. The tabulated values of W_T were plotted against B_o, using α, β, and T as parameters. The envelope of these points, as shown in Fig. I-5, gives the minimum weight of the magnet system as a function of the magnet field B_o. All values of W_T and B_o above and to the left of the envelope are possible (for constant values of w_{PS} and w_M), using various combinations of α, β, and T. The desired magnet system configurations and operating conditions are determined by the values of α, β and T which correspond to points on the envelope.

I.1.1.2 External-Radiator-Cooled Solenoid

The magnet system weight may be significantly reduced by the addition of a lightweight thermal radiator surface that is external to the solenoid. The external radiator may be either (1) a large finned structure which is in good thermal contact with the solenoid, thereby increasing the radiating area of the solenoid, or (2) a remote radiator through which the magnet coolant is circulated.*

A copper solenoid system with an external radiator weighs less than half that of a self-cooled system, as may be seen by comparison of Figs. I-5 and I-6. Also, the aluminum solenoid is about 60 percent heavier than the copper system (Fig. I-6), despite the lower density of aluminum.

For field strengths of 5 Wb/m^2 (5000 gauss) and less, radiator temperatures between 300 and 600°K appear to give the lowest system weights. Lower temperatures would, of course, require larger radiators, while the radiator weight would be negligible at higher temperatures. This minimum temperature is significant since magnets, radiators, and other components would deteriorate more rapidly in space at the higher operating temperatures. The radiator areas (which are strongly dependent on radiator density and temperature) generally range from 1 to 30 m^2 for minimum system weight.

The average "area density" w_R of the external thermal radiator over the temperature range 400 to 900°K is about 5 kg/m^2, according to the following tabulation in which the data has been taken from Ref. I-5. This "area density" value has been used for all weight calculations in this report, but differs from the value of 2 kg/m^2 used in the Semiannual Report (Ref. I-6).

*The weight of the circulating fluid and pumps may be of secondary importance. It was not included since the synthesis of the cooling system is beyond the scope of this study.

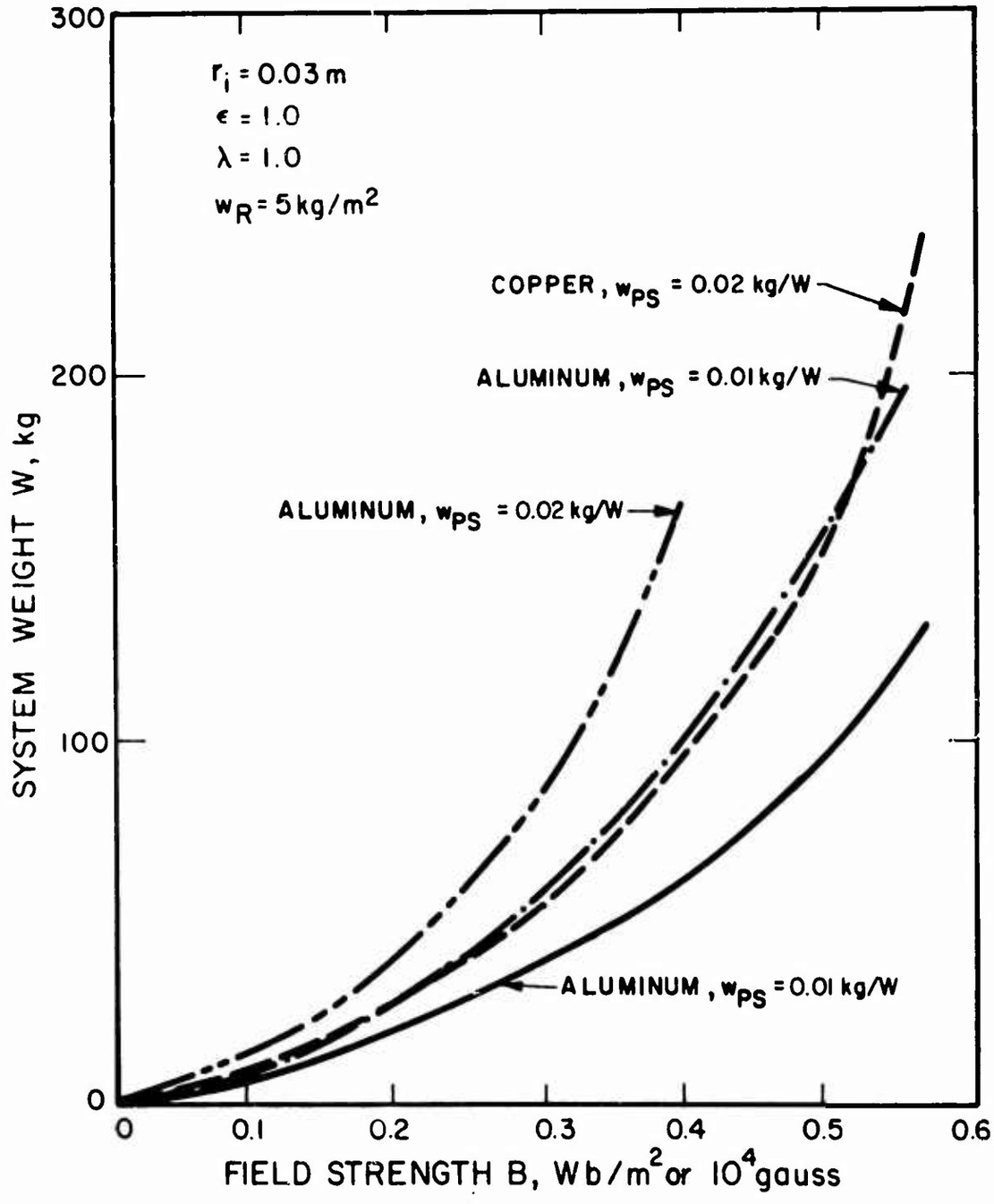

FIG. I-6 SYSTEM WEIGHTS FOR UNIFORM CURRENT DENSITY SOLENOID, EXTERNAL-RADIATOR-COOLED

Radiator Temperature (^oK)	"Power Density" (lb/kW)	kg/kW	Area Density (kg/m^2)
373	12	5.7	6.3
473	3.5	1.6	4.6
573	1.7	0.78	4.8
673	1.1	0.5	5.9
773	0.7	0.3	6.5
873	0.4	0.2	6.0

The maximum value of the magnetic field for the external-radiator-cooled solenoid is the same as that given by Eq. I-2; however, the power dissipated in the magnet must be radiated by the external radiator of area A_R. Thus,

$$P = \epsilon\sigma T^4 A_R \qquad \text{(I-6)}$$

and

$$B_o = \left[\frac{\epsilon\sigma T^4 A_R \lambda}{r\,\rho(T)}\right]^{1/2} \mu_o \left[\frac{\beta}{2\pi(\alpha^2-1)}\right]^{1/2} \ln \frac{\alpha + \sqrt{\alpha^2+\beta^2}}{1+\sqrt{1+\beta^2}} \qquad \text{(I-7)}$$

The major components of the magnet system include the power supply, the magnet, and the external radiator. If W_T is the total system weight,

$$W_T = w_{PS}P + w_M V_M + w_R A_R$$

$$= w_{PS}\epsilon\sigma T^4 A_R + w_M \cdot 2\pi r_i^3 \beta(\alpha^2-1) + w_R A_R. \qquad \text{(I-8)}$$

A numerical solution similar to that for the self-cooled case was performed, using discrete values of α, β, T, and A_R. The resulting minimum weight envelopes are shown in Fig. I-6.

I.1.2 Bitter Solenoid

A magnet design by F. Bitter (Ref. 2) uses the magnet current to produce high central magnet field strength. The current density $j_\theta(r)$ in this design varies inversely as the conductor radius, using the configuration shown in Fig. I-1. Consequently, the Bitter solenoid can produce the same magnetic field B_o as the uniform current density solenoid, while consuming only 73 percent of the power. For space applications, this can be an important weight factor, since a smaller power supply, magnet, and thermal radiator will be required.

The magnet system weights which can be achieved with a Bitter solenoid are lower than those with a uniform current density solenoid, especially at higher magnetic fields. The minimum weights for Bitter solenoids are shown in Fig. I-7 and are summarized in Table 11.1.

The Bitter solenoid has several advantages which make its use even more attractive. Thermal conduction in the radial direction is directly through the electrical conductors to the outside surface, where the thermal energy is either radiated, conducted away or removed by a circulating coolant. In the uniform current density solenoid, thermal conduction is impeded by layers of insulation between the conductors.

The Bitter solenoid design may also have a larger packing fraction than other solenoids. Packing fractions of 0.9 to 0.95 are common for Bitter solenoids with coolant passages. Uniform current density solenoids typically have packing fractions of only 0.6 to 0.8, including coolant passages.

If nuclear thermionic diodes become attractive power sources, Bitter magnets could be designed to match the output of the thermionic diodes with little or no power conditioning required. The total resistance in a Bitter solenoid is usually lower than in a uniform current density solenoid, since the conductor is generally shorter and each turn has a large cross section.

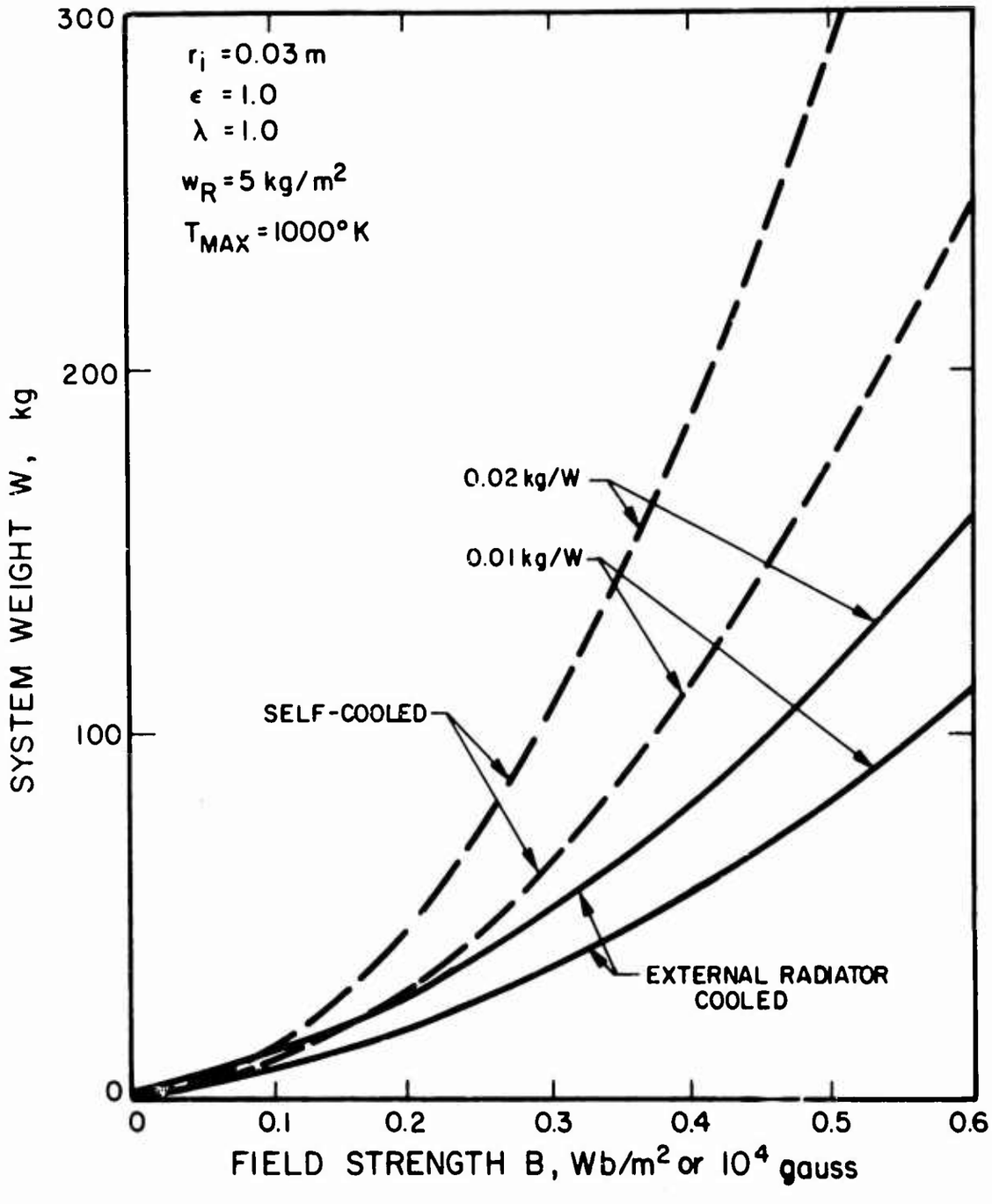

FIG. I-7 SYSTEM WEIGHTS FOR COPPER BITTER SOLENOID, SELF-COOLED AND EXTERNAL-RADIATOR-COOLED

The minimum magnet system weights for a Bitter solenoid were computed for both the self-cooled and the external-radiator-cooled cases. The equations for the magnet field B_o and the system weight W_T are as follows:

Self cooled:

$$B_o = \mu_o \left(\frac{1}{4\pi\beta \ln\alpha}\right)^{1/2} \ln\left[\alpha \cdot \frac{\beta + \sqrt{1+\beta^2}}{\beta + \sqrt{\alpha^2+\beta^2}}\right] \left(\frac{P\lambda}{\rho r_i}\right)^{1/2}$$

$$= \left[\frac{\epsilon\sigma T^4 \lambda r_i}{\rho(T)}\right]^{1/2} \mu_o \left[\frac{\alpha\beta + \frac{\alpha^2 - 1}{2}}{\beta \ln \alpha}\right]^{1/2} \ln\left[\alpha \cdot \frac{\beta + \sqrt{\beta^2 + 1}}{\beta + \sqrt{1 + \alpha^2}}\right] \quad \text{(I-9)}$$

$$W_T = w_{PS}\epsilon\sigma T^4 \cdot 4\pi r_i^2 \left(\alpha\beta + \frac{\alpha^2 - 1}{2}\right) + w_M \cdot 2\pi r_1^3 \beta(\alpha^2 - 1) \quad \text{(I-10)}$$

External-Cooled-Radiator:

$$B_o = \left[\frac{\epsilon\sigma T^4 A_R \lambda}{\rho(T) r_i}\right]^{1/2} \mu_o \left[\frac{1}{4\pi\ \beta\ \ln\ \alpha}\right]^{1/2} \ln\left[\alpha \cdot \frac{\beta + \sqrt{\beta^2 + 1}}{\beta + \sqrt{\beta^2 + \alpha^2}}\right] \quad \text{(I-11)}$$

$$W_T = w_{PS}\epsilon\sigma T^4 A_R + w_M \cdot 2\pi r_i^3 \beta(\alpha^2 - 1) + w_R A_R \quad \text{(I-12)}$$

I.1.3 Gaumé Solenoid

The Gaumé solenoid is similar to the Bitter configuration, except that the current density varies both radially and axially along the length of the solenoid. As shown in Fig. I-1, the turns of the helical conductor are thinner near the center of the solenoid. The current density in the Gaumé design is given by

$$j\theta(r,z) \propto \frac{r_i}{r}\left(\frac{\alpha}{\alpha - 1}\right)\left(\frac{1}{\sqrt{z^2 + r_i^2}} - \frac{1}{\sqrt{z^2 + \alpha^2 r_i^2}}\right)$$

The Gaumé design achieves the same magnetic field B_o as the uniform current density solenoid with only 60 percent of the input power.

Calculations of minimum magnet system weight have not yet been performed; however, the weights can be expected to be lower than for the Bitter design. This design should be carefully considered for use when the required magnetic field configuration is known.

I.2 Cryogenically Cooled Magnets

The power required to produce an electromagnetic field can be considerably reduced by lowering the resistivity of the magnet conductor material. Cryogenic cooling has been used in many applications to lower the electrical resistivity of metals to a fraction of their room temperature resistance, or even to zero (for special metals).

A copper magnet operating at a temperature corresponding to the boiling point of nitrogen ($78^{\circ}K$) will require about one-fourth the power to produce a given magnetic field as would be required at room temperature since

$$\rho_{Cu}\ (78^{\circ}K) \approx \frac{1}{4}\ \rho_{Cu}\ (300^{\circ}K)$$

and since power is proportional to density (the Fabry formula, Eq. I-1).

Because of the high weight penalty paid for electrical power in space, consideration was given to a refrigeration system which would provide a cold magnet temperature, while rejecting the heat at a much higher temperature. The two cryogenic cooling situations requiring refrigerators which should be considered are a superconducting magnet operating at $4.2^{\circ}K$ and a nonsuperconducting cryogenic magnet.

Although a nonsuperconducting magnet has not been studied carefully, it is expected that the required refrigeration system would consume more electrical power than would be saved.

For a 4.2°K superconducting magnet, the refrigeration system would weigh about 500 kg and would be practical only for large magnetic fields or large magnets. The feasibility, in turn, of large magnets depends on the thermal heat load since the magnet is near the arc jet and the hot plasma. Based on existing superconducting magnets, magnets of the sizes required would have a heat load (through the cryogenic insulation) of at least 5 or 10 watts. A refrigerator with a 10-watt capacity at 4.2°K and rejecting heat at 300°K would require approximately 10 kW of electrical power. The power supply would weigh 100 kg (using a "power density" of 0.01 kg/m^2) and it is estimated the refrigerator would weigh 200 to 300 kg. The required radiator surface of 22^2 would weigh an additional 110 kg.

I.3 Ferromagnetic Air-Core Electromagnets

The magnetic field configurations required for arc engines will require a large air gap in the magnetic circuit. Thus, ferromagnetic materials will be of primary use in shaping and concentrating the magnetic field of an electromagnet and in reducing the reluctance of the magnetic circuit. With careful design, ferromagnetic materials may be used to reduce the effective air gap of an air-core electromagnet by as much as a factor of two. Since the power required to create this field varies roughly as B^2, a 75 percent reduction of the required power is possible for a given magnetic field. However, large power reduction would be unusual; power reductions for typical arc engine magnet configurations might be only 10 to 40 percent.

The use of ferromagnetic materials will have to be studied not independently but in conjunction with the thrustor configuration. The reduction in required power and weight will have to be balanced against the added weight of these materials.

I.4 Permanent Magnets

Permanent magnets should be considered for use with arc engines with magnetic field requirements of 0.2 Wb/m^2 (2000 gauss) or less and for applications where power supply "power densities" are large (greater than about 0.02 kg/kW or 44.8 lb/kW.

Permanent magnets have many severe limitations for space applications. They are bulky and quite heavy (but require no power supply). They lose their strength when operated at temperatures above 100 to 200^{o}C and are very sensitive to thermal and magnetic cycling.

REFERENCES
APPENDIX I

I-1 Fabry, Eclairage Electrique 17, 133 (1898)

I-2 F. Bitter, Rev. Sci. Instr., 7, 482 (1936)

I-3 F. Gaume', Journal de Recherche de Centre Nationale de Recherche Scientifique No. 43 (June 1954)

I-4 D. Montgomery and J. Terrell, Some Useful Information for the Design of Air-Core Solenoids, Part I, AFOSR-1525, Air Force Contract AF 19(604)-7344, Nov 1961

I-5 Electro-Optical Systems, Inc., Applied Research on Contact Ionization Thrustors, by A. T. Forrester and S. L. Eilenberg, EOS Report 3830-Final, TN APL TDR 64-52, AF Contract AF 33(657)-10980, May 1964

I-6 Electro-Optical Systems, Inc., High Specific Impulse Thermal Arc Jet Thrustor Technology, by R. A. Moore, G. L. Cann, et al, EOS Report 5090-IR-1, ASD-TR-64, AF Contract AF 33 (615)-1579, Dec 1964

APPENDIX II
POWER DISSIPATION WITH IMPROVED COIL DESIGN

As shown in Appendix I, the maximum field strength at the center of a solenoidal coil is expressed by the Fabry formula:

$$B_o = G' \left(\frac{P\lambda}{\rho\, r_i} \right)^{1/2} \qquad \text{(II-1)}$$

Improvements over the existing coil can be made by using a current distribution which gives higher G', by designing for higher packing fraction λ, and by refining the anode and coil housing designs so that the coil will have a smaller inside radius r_i.

The power of an improved coil producing the same field strength as the existing coil would be

$$P_2 = P_1 \left(\frac{G_1'}{G_2'} \right)^2 \left(\frac{r_{i_2}\, \lambda_1}{r_{i_1}\, \lambda_2} \right) \quad , \qquad \text{(II-2)}$$

where the subscript 1 designates the present coil and

$P_1 = 22$ kW

$G_1' \approx 0.15 \times 10^{-6}$

$r_{i_1} \approx 1.75$ in.

$\lambda_1 \approx 0.48$.

For a Gaumé solenoid, as described in Appendix I, G_1' can be as high as 0.232×10^{-6}. Furthermore, the Gaumé solenoid could probably be designed with a packing fraction λ as high as 0.95. If, in addition,

the inside radius could be reduced to 1.25 in. the power of such a solenoid would be

$$P_2 = (22)\left|\frac{0.15}{0.232}\right|^2\left|\frac{1.25}{1.75}\right|\left|\frac{0.48}{0.95}\right| = 3.3 \text{ kW}$$

This calculation also assumes that the temperature of the improved coil (and thus its resistivity ρ) is the same as that of the existing coil. Further decreases in coil power may be possible by finding thrustor configurations which operate efficiently with a lower field strength. This is an extremely important consideration since the power is proportional to the square of the magnetic field strength.

APPENDIX III

TEST DATA

MODEL LAJ-CF-1

Run No.	I_A amperes	V_A volts	P_I kW	I_c amperes	P_c kW	P_t mm Hg
623	100	42.0	4.2	1800	23.4	
	158	42.0	6.6	1800	23.4	
	150	33.0	5.0	1800	23.4	
	150	29.0	4.4	1800	23.4	
	150	25-28	4.0	1800	23.4	
	200	27.5	5.5	1800	23.4	
	200	26.0	5.2	1800	23.4	
	250	27.0	6.8	1800	23.4	2.0

MODEL LAJ-AF-1

Run No.	I_A amperes	V_A volts	P_I kW	I_c amperes	P_c kW	T gf	$\dot{m}_{Li}$ g/sec	P_t mm Hg	I_{sp} sec	η
626	100	33.0	3.3	1800	23.4			9.0×10^{-1}		
	100	48.5	4.9	1800	23.4		0.074	1.0		
	150	30.0	4.5	1800	23.4		0.074	9.0×10^{-1}		
	150	29.0	4.4	1800	23.4		0.043	9.0×10^{-1}		
	200	28.0	5.6	1800	23.4		0.044	9.0×10^{-1}		
	250	29.5	7.4	1800	23.4		0.044	9.0×10^{-1}		
	300	30.5	9.2	1800	23.4		0.044	9.0×10^{-1}		
	250	28.5	7.1	1800	23.4		0.044	3.0×10^{-1}		
	250	28.5	7.1	1800	23.4		0.027	2.8×10^{-1}		
	300	30.0	9.0	1800	23.4		0.027	2.8×10^{-1}		
	300	31.0	9.3	1800	23.4		0.017	2.8×10^{-1}		
	350	32.5	11.4	1800	23.4		0.017	2.8×10^{-1}		
	350	30.0	10.5	1800	23.4		0.027	2.8×10^{-1}		
	350	42.0	14.7	1800	23.4		0.027	4.0×10^{-1}		
	350	26.2	9.2	1200	9.6		0.027	2.8×10^{-1}		
	350	23.5	8.2	800	4.4		0.027	2.8×10^{-1}		
	350	22.0	7.7	600	2.4		0.027	2.8×10^{-1}		
	350	20.5	7.2	400	1.0		0.027	2.8×10^{-1}		
	150	24.0	3.6	1800	23.4		0.027	3.0×10^{-1}		
627	200	41-50	8.2-10.0	1800	23.4		0.059	1.0		
628	100	120	12.0	1800	23.4		0.062	3.0×10^{-1}		
	100	110	11.0	1800	23.4		0.062	2.8×10^{-1}		
	100	100	10.0	1800	23.4		0.062			
	160	45	7.2	1800	23.4		0.054	8.5×10^{-1}		
	120	118	14.2	1800	23.4		0.018	1.10		
	150	42	6.3	1800	23.4		0.018	9.5×10^{-1}		
	100	140	14.0	1800	23.4		0.018	3.0×10^{-1}		
	100	110	11.0	1800	23.4		0.017	2.0×10^{-1}		

MODEL LAJ-CF-3

Run	I_A amp	V_A volts	P_I kW	I_c amperes	P_c kW	T gf	$\dot{m}_{Li}$ g/sec	$\dot{m}_{H_2}$ g/sec	P_t mm Hg	I_{sp} sec	η
629	100	142	14.2	1800	23.4			0.072	1.0		
	100	118	11.8	1800	23.4			0.034	5.0×10^{-1}		
	200	40	8.0	1800	23.4			0.015			
	160	41	6.6	1800	23.4			0.015	5.0×10^{-1}		
	50	135	6.8	1800	23.4			0.054			
630	100	142	14.2	1800	23.4	12.2		0.062	5.0×10^{-1}		
	150	42	6.3	1800	23.4	21.7			1.0		
	170	35	5.95	1800	23.4	29.6					
	100	80-110	8.0-11.0	1800	23.4	11.4					
	200	35	7.0	1800	23.4	30.4					
	250	36	8.9	1800	23.4	36.2					
	300	36	10.8	1800	23.4	40.2					
	350	36	12.6	1800	23.4	44.2					
	400	37	14.8	1800	23.4	48.2					
	450	40	18.0	1800	23.4	54.0					
	500	41	20.5	1800	23.4	58.2					
	550	43	23.7	1800	23.4	62.7					
	600	45	27.0	1800	23.4	65.3					
	200	38	7.6	1800	23.4	30.6					
	250	38	9.63	1800	23.4	36.7					
	300	39	11.7	1800	23.4	39.7					
	350	39	13.8	1800	23.4	43.7					
	400	40	15.9	1800	23.4	48.7					
	450	40	18.0	1800	23.4	55.2					
	500	41	20.3	1800	23.4	61.7					
	550	41	22.6	1800	23.4	65.5					
	600	42	24.9	1800	23.4	69.7					
	650	42	27.3	1800	23.4						
	700	44	30.5	1800	23.4	73.4					

MODEL LAJ-CF-3 (CONT)

Run	I_A amp	V_A volts	P_I kW	I_c amp	P_c kW	T gf	$\dot{m}_{Li}$ g/sec	$\dot{m}_{H_2}$ g/sec	P_t mm Hg	I_{sp} sec	η
630 (Cont)	200	40	7.9	2000	26.6	30.5	.010				
	250	40	10.0	2000	26.6	35.7	.010				
	300	41	12.3	2000	26.6	40.2	.010				
	350	42	15.1	2000	26.6	46.2	.010				
	400	43	14.7	2000	26.6	51.4	.010				
	450	45	17.2	2000	26.6	57.2	.010				
	500	46	23.0	2000	26.6	63.3	.010				
	550	47	25.9	2000	26.6	66.2	.010				
	600	43	25.8	2000	26.6	69.7	.010				
	650	48	31.9	2000	26.6	73.2	.010				
	700	50	35.4	2000	26.6	73.2	.010				
	200	66	13.2	2000	26.6	15.0	.010	.0066			
	300	60	18.0	2000	26.6	28.7	.010	.0066			
	400	59	23.6	2000	26.6	39.8	.010	.0066			
	500	58	29.0	2000	26.6	52.2	.010	.0066			
	600	59	35.4	2000	26.6	61.7	.010	.0066			
	700	60	43.4	2000	26.6	68.7	.010	.0066			
	160	63	10.1	2000	26.6	11.0	.010	.0035			
	200	58	11.6	2000	26.6	23.2	.010	.0035			
	300	57	17.1	2000	26.6	30.5	.010	.0035			
	400	56	22.4	2000	26.6	45.0	.010	.0035			
	500	56	28.0	2000	26.6	37.2	.010	.0035			
	600	57	34.2	2000	26.6	65.4	.010	.0035			
	700	59	41.3	2000	26.6	69.7	.010	.0035			
	165	50	8.30	1800	23.4	16.7	.010				
	200	48	9.6	1800	23.4	26.7	.010				
	300	48	14.3	1800	23.4	36.9	.010				
	400	48	19.0	1800	23.4	47.7	.010				
	500	48	24.0	1800	23.4	57.7	.010				
	600	52	31.2	1800	23.4	65.7	.010				
	700	53	36.8	1800	23.4	70.7	.010				

MODEL LAJ-CF-3

Run No.	I_A amperes	V_A volts	P_I kW	I_c amperes	P_c kW	T gf	$\dot{m}_{Li}$ g/sec	P_t mm Hg	I_{sp} sec	η
630	165	50	8.25	2000	26.0	16.2	.010			
(Cont.)	200	47	9.80			21.2				
	350	47	16.6			40.7				
	450	49	21.8			51.2				
	550	49	26.7			60.2				
	600	51	30.6			62.2				
	650	52	33.8			64.7				
	700	54	38.5			67.7				
631	160	39	6.2		26.0	24.2				
	200	40	8.0			30.5				
	300	40	12.0			46.2				
	350	41	14.2			52.2				
	400	42	16.8			59.2				
	500	43	21.5			66.9				
	550	45	24.8			72.5				
	700	48	3.33			78.2				
	400	45	18.0			51.7				
	400	40	16.0			60.9		2.5		
	400	42	16.6			58.2		2.0		
	400	46	18.4			48.9		1.5		
	400	55	22.0			39.7		1.0		
	400	69	27.6			28.7		7.0×10^{-1}		
632	200	47	9.3	1800	22.5	12.5	.010	4.0×10^{-1}	1250	8.06
	200	67	13.3			19.3		4.5×10^{-1}	1930	13.4
	200	36	7.2			17.3		4.0×10^{-1}	1730	20.0
	400	37	14.8			47.3		3.5×10^{-1}	4730	72.6
	400	37	14.8			45.0		4.0×10^{-1}	4500	65.7
	400	37	14.8			35.3		4.0×10^{-1}	3530	40.4
	400	37	14.8			27.4		4.0×10^{-1}	2740	24.3

MODEL LAJ-CF-4

Run No.	I_A amperes	V_A volts	P_I kW	I_c amperes	P_c kW	T gf	$\dot{m}_{Li}$ g/sec	P_t mm Hg	I_{sp} sec	η
636	120-130	79-80	9.4	2000	24.0		.018	2.0×10^{-2}		
	200	87	17.4	2000	24.0		.015	9.0×10^{-2}		
	70	126	8.1	2000	24.0		.017	8.0×10^{-2}		
	170	79	13.4	2000	24.0		.017	6.0×10^{-2}		
	170	86	14.6	2000	24.0		.017	6.0×10^{-2}		
637	200	65	13.0	1800	19.8		.018	5.2×10^{-2}		
641	100	74	7.4	1800	24.5		.010	5×10^{-2}		
	200	75-78	15.0	1800	24.5		.010	6×10^{-2}		
	205	74	15.3	1800	24.5	31.3	.010	6×10^{-2}	3130	.31
	200	65-75	14.0	1800	24.5	30.0	.010	6×10^{-2}	3000	.31
	200	65	13.0	1800	24.5		.010	1×10^{-1}		
	300	40-60	22.2	1800	24.5	36.1	.010	9×10^{-2}	3610	.28
	300	83	24.9	1800	24.5		.010	1.3×10^{-1}		
	300	80	24.0	1800	24.5		.010			
	300	83	24.9	1800	24.5	36.3	.010	1.5×10^{-1}	3630	.25
	400	96	38.4	1800	24.5		.010	1.1×10^{-1}		
	350	65	22.8	1800	24.5	45.0	.005		4500	.43
	250	93	23.3	1800	24.5	28.0	.005	1.3×10^{-1}	5600	.32

MODEL LAJ-CF-5

Run No.	I_A amperes	V_A volts	P_I kW	I_c amperes	P_c kW	T gf	$\dot{m}_{Li}$ g/sec	P_t mm Hg	I_{sp} sec	η
642	100	94	9.4	1800	22.5	--	.0200	3×10^{-2}		
	250	43	10.8	1800			.0200	2×10^{-2}		
	85	110	9.3	1800			.0200	2×10^{-2}		
	92	70	6.4	1800			.0031	2×10^{-2}		
	90	70	6.3	1800		12.0	.0033	2×10^{-2}	3820	.35
	90	68	6.1	1800		11.75	.0032	2×10^{-2}	3850	.35
	150	82	12.3	1800		18.4	.0062	2×10^{-2}	3100	.22
	150	77	11.5	1800		17.4	.0062	2×10^{-2}	2950	.21
	200	62	12.4	1800		21.6	.0062	2×10^{-2}	3660	.31
	100	80	8.0	1800		17.5	.0062	1.6×10^{-2}	2960	.31
	100	78	7.8	1800		16.9	.0062		2860	.30
	150	100	15.0	1800		27.5	.0062		4650	.41
	200	109	21.8	1800		38.5	.0062		6510	.51
	250	120	30.0	1800		45.0	.0062		7610	.55
	300	115	34.5	1800			.0062			
	300	120	36.0	1800		45.0	.0061		7760	.47
						50.0	.0061		8600	.57
643	150	80	12.0	1800		19.1	.0101		1890	.15
	150	70	10.5	1800		17.0	.0101	2.2×10^{-2}	1675	.13
	150	76	11.4	1800		17.2	.0102	2.2×10^{-2}	1690	.12
	150	75	11.2	1800		16.0	.0101	2.2×10^{-2}	1580	.11
	150	100	15.0	1800		21.2	.0102	2.0×10^{-2}	2080	.14
	210	85	17.8	1800		22.0	.0101	2.8×10^{-2}	2180	.13
	210	83	17.4	1800		19.5	.0100	2.8×10^{-2}	1950	.10
	200	90	18.0	1800		26.6	.0101	3.0×10^{-2}	2620	.19
	230	86	19.8	1800		26.2	.0101	3.0×10^{-2}	2580	.16
	235	84	19.7	1800		25.9	.0100	3.0×10^{-2}	2580	.16
	85	90	7.6	1800		9.5	.0101	3.0×10^{-2}	935	.06
	350	50	17.5	1800		52.0	.0100			.74

MODEL LAJ-AF-2

Run No	I_A amperes	V_A volts	P_I kW	I_c amperes	P_c kW	T gf	$\dot{m}_{Li}$ g/sec	P_t mm Hg	I_{sp} sec	η
644	295	45-55	14.8	1800	22.5	23.4	.01		2340	.178
	300	38	11.4	1800		26.4	.01		2640	.293
	300	38	11.4	1800		27.6	.01		2760	.321
	200	43	8.6	1800		29.4	.01		2940	.482
	300	39	11.7	1800		39.4	.01		3940	.637
	345	54	18.6	1800		44.9	.01		4490	.520
	405	43	17.4	1800		50,0	.01		5000	.690
	450	50	22.5	1800		56.0	.01		5600	.669
	292	58	16.9	1800		34.9	.01		3490	.346
	300	41	12.3	1800		31.6	.01		3160	.390
	297	35	10.4	1800		41.9	.020		2090	.396
	200	34.5	7.0	1800		28.1	.020		1410	.272
	405	39	15.8	1800		53.8	.020		2690	.440
	150	37	5.6	1800			.020			
	300	36	10.8	1800		25.0	.0102		2450	.272
	300	40	12.0	1800		28.1	.0102		2760	.310
	300	39	11.7	1800		28.8	.0102		2820	.332
	300	38	11.4	1800		29.4	.0105		2800	.346
	300	36	10.8	1800		31.3	.0106		2950	.409
	300	36	10.8	1800		31.3	.0106		2950	.409
	200	40	8.0	1800		20.0	.0106		1890	.226
	300	39	11.7	1800		36.3	.0106		3420	.509
	300	38.5	11.3	1800		36.3	.0106		3420	.529
	350	48	16.8	1800		41.3	.0107		3860	.454
	400	47.5	19.0	1800		53.1	.0105		5060	.679
	404	45.0	18.2	1800		53.1	.0105		5060	.709
	400	45.0	18.0	1800		53.1	.0105		5060	.717
	450	51	23.0	1800		55.6	.0103		5400	.627
	300	41	12.3	1800		36.3	.0103		3520	.498
	300	43	12.9	1800		36.3	.0103		3520	.475

MODEL LAJ-AF-2 (CONT.)

Run No.	I_A amperes	V_A volts	P_I kW	I_c amperes	P_c kW	T gf	$\dot{m}_{Li}$ g/sec	P_t mm Hg	I_{sp} sec	η_i
644 (cont.)	300	37	11.1	1800		36.3	.0102		3550	.56
	300	35	10.5	1800		38.8	.0192		2020	.36
	300	36	10.8	1800		36.6	.0192		1910	.31
	487	40	19.5	1800		58.8	.0190		3090	.45
	200	34	6.8	1800		23.8	.0190		1250	.21
	402	39	15.7	1800		47.5	.0191		2490	.36

MODEL LAJ-AF-3

	I_A amperes	V_A volts	P_I kW	I_c amperes	P_c kW	T gf	$\dot{m}_{Li}$ g/sec	P_t mm Hg	I_{sp} sec	η
646	250	35	8.75	1800	22.7	29.4	.0091	1.1×10^{-2}	3230	.52
	300	36.5	11.0	1800	22.7	39.4	.0091		4330	.74
	300	33.5	10.0	1800	22.7	40.6	.0091	6.0×10^{-3}	4460	.86
	300	33	9.9	1800	22.7	25.0	.0091	6.0×10^{-2}	2750	.33
	300	50	15.0	1800	22.7	30.0	.0091		3300	.31
	300	55	16.5	1800	22.7	31.2	.0091		3430	.30
	300	56	16.8	1600	17.9	32.5	.0091		3570	.33
	300	56	16.8	1600	17.9	30.0	.0091	2.0×10^{-2}	3300	.28
	300	58	17.4	1600	17.9	31.2	.0091		3430	.29
	300	49.5	14.8	1200	10.1	21.2	.0091		2330	.16
	300	53.5	16.0	1200	10.1	25.0	.0091		2750	.20
	300	40.5	12.2	1200	10.1	35.6	.0091		3910	.55
	300	28.5	8.55	1200	10.1	29.4	.0091		3230	.53
	300	32	9.60	1200	10.1	20.0	.0091		2200	.20
	300	32	9.60	1400	13.7	30.6	.0091	5.0×10^{-3}	3360	.51
	300	35	10.5	1400	13.7	26.2	.0091		2880	.34
	340	65	22.1	1400	13.7	32.2	.0091		3540	.25
	120	66	7.92	1800	22.7	15.4	.0091		1690	.15

MODEL LAJ-AF-4

Run No.	I_A amperes	V_A volts	P_I kW	I_c amperes	P_c kW	T gf	$\dot{m}_{Li}$ g/sec	P_t mm Hg	I_{sp} sec	η
647	400	38	15.2	1800	22.5		.0045	6×10^{-5}		
	310	45-48	13.9-14.8	1800			.0045			
	300	35	10.5	1800		24.1			5300	.58
	350	32	11.2	1800		23.0	.0045		5060	.55
	400	38	15.2	1800		33.2			7300	.77
	400	35	14.0	1800		30.5			6710	.70
	400	35	14.0	1800		30.5			6710	.70
	400	35	14.0	1800		34.2			7520	.88
	400	36	14.4	1800		34.2			7520	.86
	400	35-36	14.0-14.4	1800		33.0			7260	.80
	450	37	16.6	1800		38.5			8470	.95
	450	39.5	17.8	1800		36.8			7870	.78
	450	39	17.5	1800		34.6			7610	.72
	450	38.5	17.3	1800		38.3			8640	.90
	450	40	18.0	1800		33.2			7300	.65
	450	40	18.0	1800		35.8		3×10^{-3}	7870	.74
	450	40	18.0	1800		38.9			8550	.89
	300	40-45	12.-13.5	1800		26.6			5850	.58
	300	45-50	13.5-15	1800		28.4			6240	.59
	300	50	15.0	1800		28.4			6240	.57
	300	56	16.8	1800		29.0			6380	.53
	350	53	18.5	1800		29.8			6550	.51
	300	49	14.7	1800		23.5			5170	.40
	300	50	15.0	1800		28.4			6240	.57

MODEL LAJ-AF-5

Run No.	I_A amperes	V_A volts	P_I kW	I_c amperes	P_c kW	T gf	$\dot{m}_{Li}$ g/sec	P_t mm Hg	$\dot{m}_{H2}$ g/sec	I_{sp} sec	η
655	165	115	18.9	1800	2.5	24.3	.0091	1.7×10^{-1}	.010	1320	.08
	200	118	23.6	1800	7.2	31.0	.0087	1.7×10^{-1}	.010	1730	.22
	200	108	21.6	1800	7.4	29.1	.0089	1.25×10^{-1}	.0057	2060	.13
	200	99	19.8	1800	7.40	36.0	.0089	1.10×10^{-1}	.0056	2570	.22
	200	108	21.6	1800	7.47	28.5	.0089	1.25×10^{-1}	.0056	2020	.13
	200	100	20.0	1800	7.40	33.5	.0090	1.25×10^{-1}	.0059	2340	.19
	200	98	19.6	1800	7.4	34.8	.0089	1.18×10^{-1}	.0050	2588	.22
	200	98	19.6	1700	7.45	31.5	.0089	1.12×10^{-1}	.0050	2320	.18
	200	98	19.6	1600	7.45	29.8	.0090	1.12×10^{-1}	.0050	2200	.16
	200	98	19.6	1500	7.45	26.0	.0090	1.12×10^{-1}	.0050	1910	.12
	150	93	13.9	1500	7.43	28.8	.0090	1.15×10^{-1}	.0059	2000	.20
	150	82	12.3	1500	7.38	12.5	.0090	6.3×10^{-1}	.0020	1150	.06
	150	86	12.9	1800	7.40	16.0	.0089	6×10^{-2}	.0020	1490	.09
	150	97	14.5	1800	5.0	23.1	.0045	1.20×10^{-1}	.0059	2330	.18
	200	104	20.8	1800	5.0	25.4	.0045	9.8×10^{-2}	.0030	3430	.20
	200	118	23.6	1800	5.1	34.1	.0046	1.80×10^{-1}	.010	2480	.17

APPENDIX IV
MATERIALS COMPATIBILITY STUDY

A review of the literature and a fundamental study of the compatibility of solid materials with lithium have provided tentative choices of best materials for the lithium arc jet and feed system.

Tungsten appears to be the best material for electrodes operating in lithium provided that

1. The tungsten is of sufficiently high purity.
2. The lithium is free of oxide and nitride.

The commercial grades of lithium are not pure enough for use with refractory metals. A high-purity grade (less than 31 parts per million of nitrogen) may prove to be satisfactory. If not, it will be necessary to use purification techniques as described in a later paragraph. The 347 grade of stainless steel was chosen for the feed system as recommended in Ref.IV-1. Ferritic stainless steels are suitable for applications at temperatures up to about 800°C. High-density and high-purity forms of beryllia, zirconia and alumina appear to be compatible high temperature insulating materials. However, the operating temperatures of the insulators must be kept below the temperature at which the oxidation-reduction equilibrium is upset. Beryllia may be the best choice because of higher resistivity at high temperatures and better thermal shock resistance. However, beryllia is very expensive to use because of the health hazard in machining it and using it in the laboratory. Thus, the initial devices had alumina or boron nitride insulators. The alumina, a low-density grade, was totally unsatisfactory. Boron nitride erodes; however, it lasts for a few hours and will be used for initial tests on new thrustor configurations.

IV.1 Summary of Corrosion Data

Figure IV-1 shows the maximum temperature range in which various materials may be useful with lithium. These results were obtained from a survey of corrosion test data found in the literature.

Much of the available literature concerning the corrosion of various metals in lithium is of little value since the amount of impurities was not reported for either the container material or lithium. Lithium is highly reactive with most of the major constituents of the surrounding atmosphere - oxygen, nitrogen and water. The compounds formed by lithium with these elements are therefore usually present as impurities. All of these compounds react with most materials of construction at elevated temperatures. Lithium, in absolutely pure form, is considered by many to be noncorrosive with most metals.

Much of the present data is also questionable because the sample specimens and the lithium container were of different metals. Such test conditions may lead to erroneous test results due to a phenomenon known as concentration gradient transfer. Concentration gradient transfer occurs between dissimilar test metals immersed in a liquid metal if both of the following conditions are satisfied:

1. The liquid metal dissolves one of the test materials.
2. The second metal forms an alloy or intermetallic compound with the first.

An example of this type of attack is the transfer of molybdenum to iron in lithium.

IV.2 Effects of Impurities on Corrosion of Metals

Observations of the interactions between liquid and solid metals have led to classifications of the various types of corrosion mechanisms. One such classification (Ref. IV-2) for metal-alkali systems is as follows:

1. Solution Corrosion Mechanisms
   a. Dissolution of solid metal by liquid metal.
   b. Dissimilar metal mass transfer.
   c. Temperature gradient mass transfer.

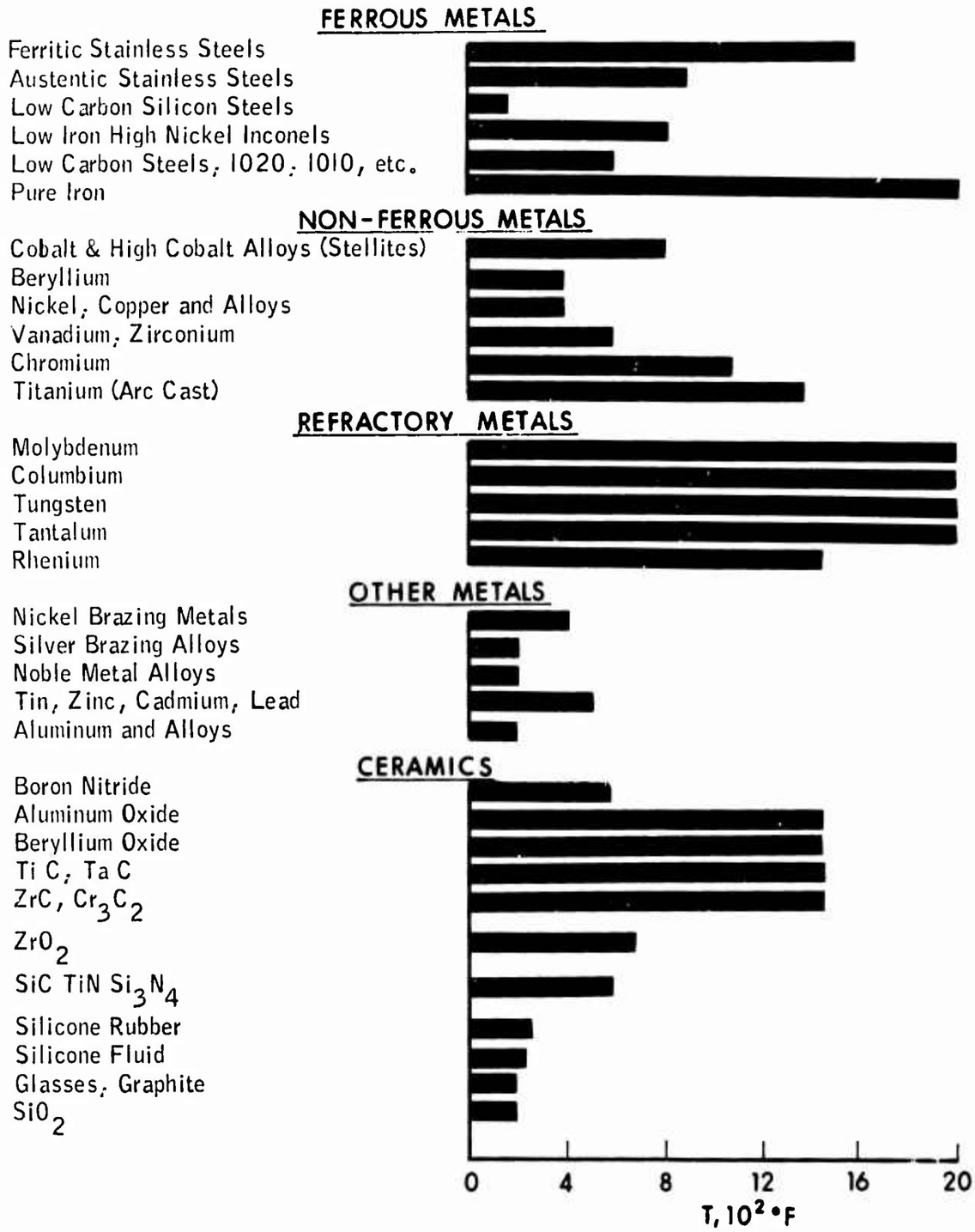

FIG. IV-1 STATIC COMPATIBILITY OF MATERIALS WITH LITHIUM
(Solid bars indicate region of usefulness)

2. Impurity Reaction Mechanisms
   a. Liquid-metal impurities.
   b. Solid-metal impurities.
   c. Partitioning of impurities between solid and liquid metal.

Tests have demonstrated that impurities in the system can increase the corrosion of refractory metals. When an element such as oxygen is in solution in both the solid and liquid metal, it will be redistributed until it has the same chemical potential in each phase. At a particular temperature, the equilibrium ratio of the concentration of oxygen in each phase should be constant. It can be calculated from the following expression:

$$\frac{C_B}{C_A} = \exp\left[\frac{\Delta F_+^o \text{ (A Oxide)} - \Delta F_+^o \text{ (B Oxide)}}{RT}\right] \frac{(C_B)_S}{(C_A)_S} \qquad \text{(IV-1)}$$

where the symbols are defined as follows:

C_A : Concentration of solute in phase A

C_B : Concentration of solute in phase B

ΔF_+^o (A Oxide) : Standard free energy of formation of the oxide of A which can be in equilibrium with a solution of oxygen in A

ΔF_+^o (B Oxide) : Standard free energy of formation of the oxide of B which can be in equilibrium with a solution of oxygen in B

$(C_B)_S$: Solubility of oxygen in B

$(C_A)_S$: Solubility of oxygen in A

At 500°C and 800°C the following ratios were calculated from this equation (Ref. IV-3).

System	Concentration of O_2 in Solid Metal / Concentration of O_2 in Lithium	
	500°C	800°C
Niobium-oxygen-lithium	5×10^{-11}	1×10^{-7}
Tantalum-oxygen-lithium	3×10^{-11}	3×10^{-8}
Vanadium-oxygen-lithium	7×10^{-11}	3×10^{-9}
Titanium-oxygen-lithium	5×10^{-2}	2×10^{-2}
Zirconium-oxygen-lithium	3	4

Although these values may be incorrect by a few orders of magnitude, they indicate that lithium should getter most of the oxygen present in niobium, tantalum or vanadium. Titanium and zirconium, on the other hand, will either gain or lose oxygen in lithium, depending upon the initial concentration in each. Since tungsten is less reactive chemically than niobium it would be expected that lithium would getter nearly all of the oxygen present in tungsten.

The pure metals, niobium, tantalum, vanadium, titanium, and zirconium, exhibit excellent resistance to dissolutive attack by lithium at temperatures in excess of 800°C. However, the presence of small quantities of oxygen in either niobium or tantalum can cause the rapid penetration of these metals by lithium over a wider range of temperatures (Ref. IV-3). Vanadium, titanium, and zirconium, on the other hand, do not show this susceptibility to lithium penetration even at oxygen concentrations in excess of 2000 parts per million. Apparently those metals whose oxides are most acidic are most prone to lithium penetration. Tungstic oxides are very acidic.

Penetration of lithium into the refractory metals results in the formation of a complex corrosion product in grain boundaries or crystallographic planes of the material. This reduces both strength and ductility which are important to thermal shock and stress resistance.

Oxygen impurities within the refractory metals may result from the manufacturing process, improper fabrication procedures or from

redistribution from liquid lithium. Residual oxides within the refractory metals tend to segregate within the crystallographic planes and grain boundaries. The concentration of these oxides will therefore be dependent upon both the initial oxygen concentration and the grain size or internal surface area of the metal. In cold-rolled and other fine grain materials the oxides will be highly dispersed. Recrystallization into larger grain will result in oxide concentration at the grain boundaries.

It has been determined that, under conditions where the oxygen concentration is sufficiently high for lithium attack to occur, the rate of attack is very rapid. In the case of columbium, maximum depth of penetration was reached in less than an hour over a wide range of temperatures (Ref. IV-2).

Pure columbium was not attacked at 816°C by lithium heavily contaminated with Li_2O and Li_3N. On the other hand, specimens of impure columbium were heavily corroded (Ref. IV-2) in the same medium.

Among the ferrous metals, pure iron apparently is one of the most resistant materials to solution in liquid lithium. The data presented in Ref. IV-4 indicate that the solubility of pure iron in lithium is not excessive even at temperatures in excess of 900°C. Those metals most closely approaching pure iron in composition are Armco iron and mild steel of low alloy content.

Austenitic stainless steels are unsuitable for operation in lithium above 500°C as a result of the selective leaching of nickel. Stainless steels of low carbon and nickel content (e.g., 347, 316 ferritic grades) are suitable at temperatures up to 800°C (Ref. IV-4).

IV.3 Insulation Materials

In the presence of lithium metal or vapor at high temperatures, failure in insulator materials may occur by two mechanisms:

1. Infiltration of the liquid metal into the insulator, leading to conduction.
2. Reduction of the insulating oxide, producing conductive oxide mixtures or metals.

The first mechanism can be most easily avoided by the use of insulators of maximum possible density and purity.

Failure of the insulating material by reduction will occur when lithium effects a partial or complete removal of oxygen from the insulator. In closed systems, such as thermionic diodes, the probability of a chemical reduction process occurring can be predicted on the basis of the free energy of formation of the oxides. Metals whose oxides have a high free energy of formation reduce those oxides whose free energy of formation is lower. Figure IV-2 shows the heats of formation for lithium oxide and various other oxides of interest at temperatures up to 2500°K.

In a nonequilibrium system, such as might occur with a moving gas stream, the above laws do not apply. For example, in the following reactions, Al_2O_3 (with heat of formation at 2500°K of -70 kg-cal/gram atom of oxygen) would not be reduced by lithium metal under equilibrium conditions since the heat of formation of Li_2O is -30 kg-cal/gram atom of oxygen.

$$Al_2O_3 + 6Li \rightleftharpoons 3Li_2O + 2Al \qquad \text{(IV-2)}$$

However, in a nonequilibrium system the equilibrium might be shifted to the right, (e.g., if operating conditions were such that either of the products evaporated as a gas), thereby allowing the reaction to proceed. It is important, therefore, that such conditions be avoided in the design.

Impurities within the insulating materials having low negative heats of formation must be avoided in order to prevent gross attack by the lithium. Some early results with aluminum oxide showed poor compatibility with lithium. These experiments used aluminum oxide which contained a CaO, MnO or MgO binder. Since the free energy of formation of Li_2O is higher than that of MnO at temperatures below about 2200°K it is likely that the lithium reacted primarily with the binder. The resulting Li_2O would also tend to dissolve the pure aluminum oxide. It is important, then, that any oxide ceramic to be used should be as pure as possible.

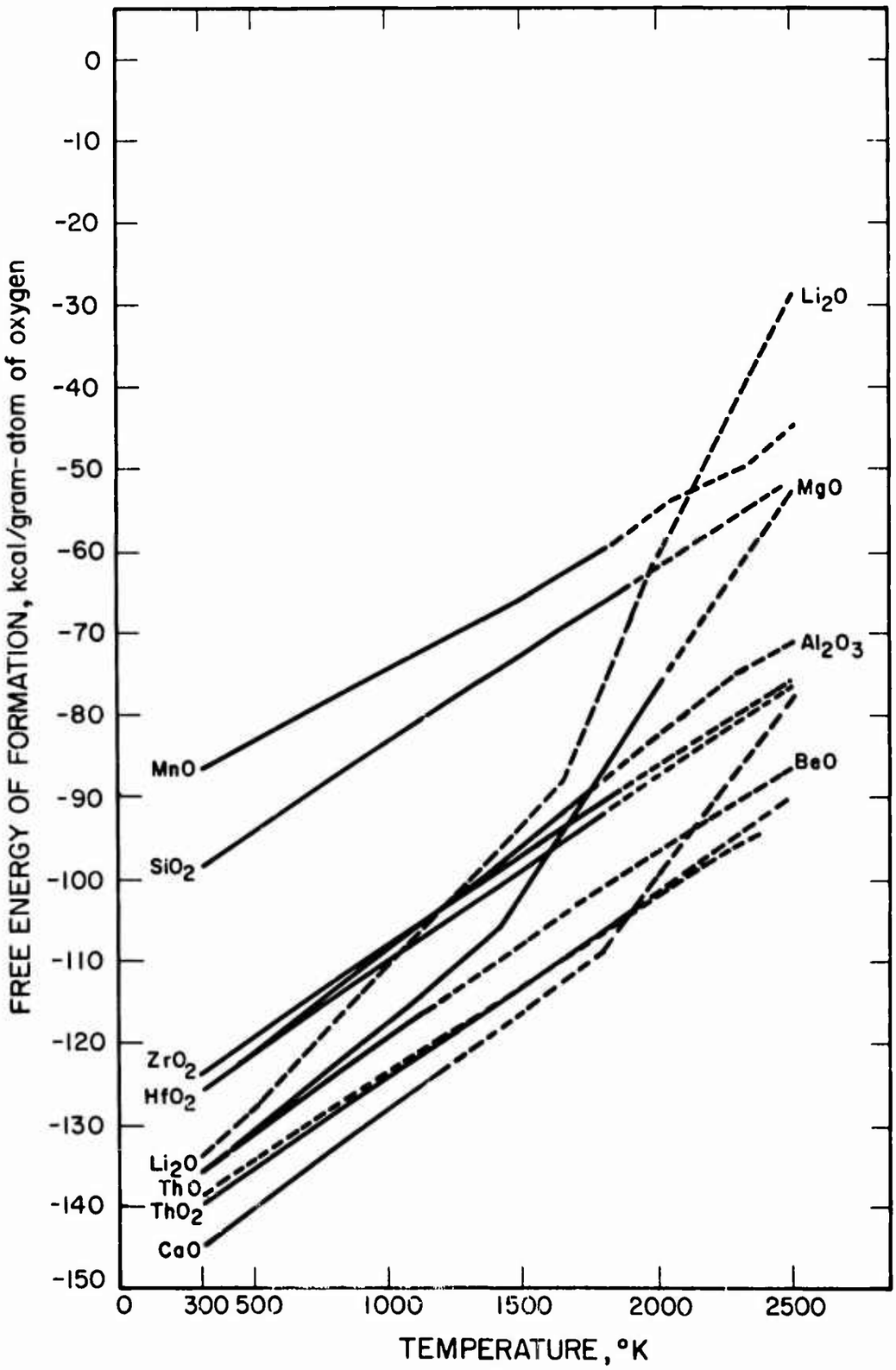

FIG. IV-2 FREE ENERGY OF FORMATION OF LITHIUM OXIDE COMPARED TO VARIOUS OTHER OXIDES

IV.4 Purification of Lithium Metal

To avoid corrosion problems over long periods of time, we have seen that lithium should be thoroughly cleaned of oxygen and nitrogen. This may be done to a certain degree by filtering the metal at 300°C through 10-20μ stainless steel filters. Filtering, however, removes only the insoluble impurities. Since nitrogen is particularly soluble in lithium, gettering is necessary. (Oxygen is soluble to a somewhat lesser degree.)

Zirconium has been found to getter nitrogen in lithium at temperatures of 300°C or above (Ref. IV-5). But, at these temperatures, unless the metal is very clean, zirconium tends to be itself gettered of oxygen by the lithium. To remove the oxygen at temperatures of 300°C or more, yttrium has been found to be a good gettering agent.

A lithium purification procedure is described by Hoffman (Ref. IV-6) which will reduce the oxygen concentration to 100-200 parts per million, and the nitrogen content to less than 20 parts per million. Briefly, this procedure consists of the following steps:

1. Filtration at 250°C through a 10μ-pore stainless steel filter to remove gross amounts of lithium nitride and oxide.

2. Heating the lithium in contact with titanium sponge for 24 hours at 800°C to reduce the nitrogen content to less than 100 parts per million.

3. Cold trapping for 100 hours to reduce the oxygen concentration to 100-200 parts per million. Thus, using filtering and gettering, lithium can be purified to a considerable degree and corrosion over long periods of time should be considerably reduced.

Test results on the refractory metals have indicated little attack with the oxygen concentration below 400 parts per million. Nitrogen and carbon content appear to exert less effect than oxygen on the corrosion characteristics of lithium.

Analytical methods of determining nitrogen concentration in lithium are described by White (Ref. IV-7) and Sax (Ref. IV-8). Oxygen content may be determined by activation analysis (Ref. IV-9).

IV.5 Cleaning and Fabrication Procedures

It is important that metals which contact lithium should be cleaned of all oxide layers. Surface oxides which are normally present on most metals after lengthy exposure to the atmosphere would be reduced by the lithium. Lithium oxide would form and tend to severely corrode the metal. Tungsten may be cleaned by boiling in a 20 percent solution of K(OH). Molybdenum may be cleaned by immersion in a molten salt bath at 500-700°F of 70 percent NaOH and 30 percent $NaNO_2$.

Stainless steels should be cleaned in any good "warm" etch, such as 100 HNO_3, 60 HAc or 30 HF. Titanium may be cleaned by immersion in a solution containing 95 parts H_2O to 10 parts HF (40 percent), then rinsing in distilled water and acetone, and drying in argon. It should always be wrapped in a plastic film and stored in an argon atmosphere.

All apparatus should be fabricated of selected materials of the highest obtainable degree of purity. In the case of refractory metals, arc- or electron-beam-melted materials should be used. All joining operations such as welding should be performed in an inert environment. Before welding, equipment such as tanks and tubing should be purged internally with dry helium or argon.

REFERENCES

APPENDIX IV

IV-1 J. R. Di Stefano and E. E. Hoffman, "Corrosion Mechanisms in Refractory Metal - Alkali Metal Systems", USAEC Report ORNL-3424, August 1963

IV-2 J. R. Di Stefano, "Corrosion of Refractory Metals by Lithium", USAEC Report ORNL-3551, March 1964

IV-3 R. N. Lyon, Liquid Metals Handbook (Supt. of Documents, Washington, D. C., 1952), 2nd ed.

IV-4 S. J. Rodgers, F. Tepper, et al., "Optimum Purification Techniques for the Removal of Contaminants from Liquid Lithium and Rubidium", Technical Documentary Report APL-TDR-64-34, Air Force Aero Propulsion Laboratory, March 1964

IV-5 E. E. Hoffman, "Solubility of Nitrogen and Oxygen in Lithium and Methods of Lithium Purification", Symposium on Newer Metals, Special Technical Publication No. 277, American Society for Testing Materials, Philadelphia, Pennsylvania, pp 195-20, 1959

IV-6 J. C. White, et al., Aircraft Nuclear Propulsion Project, Quarterly Progress Report for Period Ending September 10, 1956, USAEC Report ORNL-2157 (Parts 1-5, ; 128)

IV-7 N. Sax, N. Chu, et al., "Determination of Nitrogen in Lithium" USAEC Report NDA-38, June 1957

IV-8 G. W. Leddicotte, Analytical Chemistry Division, Annual Progress Report for Period Ending December 31, 1957, USAEC Report ORNL-2453, p. 30